GNSS-based Spacecraft Formation Flying Simulation and Ionospheric Remote Sensing Applications

Yuxiang Peng

Thesis submitted to the faculty of the Virginia Polytechnic Institute and State University in partial fulfillment of the requirements for the degree of

Master of Science
In
Electrical Engineering

Wayne A. Scales (Chair)
Jonathan T. Black
Dennis G. Sweeney

May 8, 2017
Blacksburg, VA

Keywords: GNSS, GPS, Spacecraft Formation Flying, HIL Simulation, Remote Sensing, TEC, Ionospheric Irregularity, Scintillation

GNSS-based Spacecraft Formation Flying Simulation and Ionospheric Remote Sensing Applications

Yuxiang Peng

Abstract

The Global Navigation Satellite System (GNSS) is significantly advantageous to absolute and relative navigation for spacecraft formation flying. Ionospheric remote sensing, such as Total Electron Content (TEC) measurements or ionospheric irregularity studies are important potential Low Earth Orbit (LEO) applications. A GNSS-based Hardware-in-the-loop (HIL) simulation testbed for LEO spacecraft formation flying has been developed and evaluated. The testbed infrastructure is composed of GNSS simulators, multi-constellation GNSS receiver(s), the Navigation & Control system and the Systems Tool Kit (STK) visualization system. A reference scenario of two LEO spacecraft is simulated with the initial in-track separation of 1000-m and targeted leader-follower configuration of 100-m along-track offset. Therefore, the feasibility and performance of the testbed have been demonstrated by benchmarking the simulation results with past work.

For ionospheric remote sensing, multi-constellation multi-frequency GNSS receivers are used to develop the GNSS TEC measurement and model evaluation system. GPS, GLONASS, Galileo and Beidou constellations are considered in this work. Multi-constellation GNSS TEC measurements and the GNSS-based HIL simulation testbed were integrated and applied to design a LEO satellite formation flying mission for ionospheric remote sensing. A scenario of observing sporadic E is illustrated and adopted to demonstrate how to apply GNSS-based spacecraft formation flying to study the ionospheric irregularities using the HIL simulation testbed. The entire infrastructure of GNSS-based spacecraft formation flying simulation and ionospheric remote sensing developed at Virginia Tech is capable of supporting future ionospheric remote sensing mission design and validation.

GNSS-based Spacecraft Formation Flying Simulation and Ionospheric Remote Sensing Applications

Yuxiang Peng

General Audience Abstract

Global Navigation Satellite Systems (GNSS), such as the Global Positioning System (GPS), are not only used to navigate vehicles such as automobiles and spacecraft, but they are also used as a tool to remotely study the Earth's ionosphere. A GNSS-based hardware simulation testbed for a group of spacecraft flying in low altitude orbit with the capability to remotely sense the ionosphere has been developed and evaluated. The hardware testbed developed is composed of GNSS signal emulators, GNSS signal receiver(s), the spacecraft navigation & control system and a mission visualization system. A reference scenario of two spacecraft in low altitude orbit with an initial horizontal distance of 1000-m and a final separation of 100-m is successfully simulated. Therefore, the feasibility and performance of the hardware testbed have been demonstrated by comparing the simulation results with past work.

To study the Earth's ionosphere, advanced GNSS receivers along with newly developed software are used to measure the ionospheric electron concentration. This software can be integrated with the hardware testbed and utilized to design spacecraft missions to study the ionosphere from the space. A scenario for observing a unique ionospheric structure is implemented to demonstrate application of the hardware testbed to more general ionospheric studies. Combining the software for ionospheric measurement and the hardware testbed for two spacecraft flying in formation can support future mission design and validation.

Acknowledgement

First of all, I would like to express the most sincere gratitude to my advisor and committee chair Professor Wayne Scales. His understanding, support, mentoring, and guidance have lightened my pathway to pursue my dream.

Second of all, I would like to thank my parents and my uncles for encouraging me to follow my interests and supporting me every step of the way.

I also want to thank Dr. Jonathan Black and Dr. Dennis Sweeney for being my committee members and giving me valuable advice for this work.

I have been fortunate enough to know Dr. Anthea Coster and to have the opportunity to learn from her. Specifically, I would like to thank her for sharing her wisdom on ionospheric remote sensing.

I would like to acknowledge my fellow student, Thomas Edwards, for his help and contribution to my work. It was a pleasure and enjoyable experience to work with him.

Thanks to Dr. Mark Psiaki for sharing his expertise on Kalman Filtering. Thanks to Dr. Andrew Rogers for sharing his experience on spacecraft formation flying and giving me advise for this work. I want to thank Xavier Gomez, Tunc Ertan, Daniel Luciani, Ian Elliot, Dong Lin, Xueling Shi, Fred Harris and Marc Jeans for providing help at various stages throughout my work.

Last but not least, I want to thank Alexandra Pedin for helping and giving me encouragement throughout this process.

Table of Contents

List of Figures

List of Tables

Chapter 1

Introduction

Spacecraft formation flying, a space mission architecture of multiple satellites orbiting together in a specific configuration, is significantly advantageous to space science research and commercial space development. For general space mission applications, such as spacecraft rendezvous or docking, spacecraft formation flying is a critical technique used to realize precise control of collaborative distributed space systems. Two classical examples are the assembly of the Intentional Space Station (ISS) and Cargo Ship Delivery Mission for ISS. Compared with traditional single spacecraft mission, spacecraft formation flying can be more flexible and less costly by deploying several smaller agile satellites. For the purpose of space environment exploration, deploying scientific instruments on different satellites and letting them fly in formation enables a higher flexibility of the field of view by changing the relative orbits. In this way, the spacecraft can precisely and flexibly survey the space environments through in-situ measurement or remote sensing.

Global Navigation Satellite System (GNSS) is a space-based radio navigation system that utilizes a group of satellites to realize geo-spatial positioning globally. Currently, there are four main GNSS constellations in different status of development: GPS (American GNSS system), GLONASS (Russian GNSS system), Galileo (European Union GNSS system) and Beidou (Chinese GNSS system). GNSS plays an important role in spacecraft formation flying as it can provide not only absolute navigation onboard for orbit determination of each spacecraft, but also highly accurate relative navigation based on differential GNSS measurement techniques. The orbital altitude of all GNSS systems are approximately 20,000 km. Therefore, any spacecraft with an orbit below 20,000km (within the coverage of GNSS constellations) would be able to use GNSS for formation flying navigation. Nonetheless, it's not impossible to use GNSS for high-altitude orbit spacecraft navigation. Since the 1990's, several experiments were designed to implement GNSS side-lobe signals for spacecraft positioning and navigation in Medium Earth Orbit (MEO), High Earth Orbit (HEO), or Geostationary Earth Orbit (GEO) [1]. Other than GNSS, there are several other modern navigation techniques can be used for spacecraft orbit determination, such as inertial navigation system, radar navigation/tracking or satellite laser tracking [2][3]. Because of the combination of high accuracy, availability and stability, GNSS is often chosen for LEO satellite navigation.

Currently, CubeSats are under development at Virginia Tech for Low Earth Orbit (LEO) missions to study the upper atmosphere, such as the LAICE CubeSat mission for gravity wave studies [4]. To support future LEO satellite formation flying missions design, it is proposed to develop a Hardware-in-the-Loop (HIL) spacecraft formation flying simulation testbed, which will provide a realistic hardware platform to test and validate the flight control algorithm of satellite mission. Inspired by reference [5] on HIL satellites formation flying simulation, the Virginia Tech Formation Flying Testbed (VTFFTB) for GNSS-based HIL simulation of spacecraft formation flying is developed. The VTFFTB is composed of Spirent GNSS simulators, multi-constellation GNSS receivers, a GNSS measurement system, a flight control system, a remote control system and additionally a STK mission visualization system. The primary goal of this work is to reproduce the

simulation results of reference [5], as well as validate the feasibility and performance of the closed-loop GNSS-based simulation on the VTFFTB, and ultimately attempt to apply the VTFFTB to ionospheric remote sensing.

MathWorks MATLAB and AGI Systems Tool Kit (STK) were used to develop the software system of the VTFFTB. LEO orbit formation-flying scenarios consist of two satellites, one chief satellite and one deputy satellite, were selected in this work for experiments. The GNSS data from the receiver are transferred to the GNSS measurement system via the Universal Serial Bus (USB) communication. A single-difference pseudorange measurement model is adopted for relative navigation between chief and deputy satellite. Absolute navigation of the chief satellite combined with relative navigation, and the relative states predicted by the spacecraft dynamics propagator would be fed into the Extended Kalman Filter (EKF) to drive the GNSS measurement system. The Joint Gravity Model 3 (JGM-3) was compared with the Kepler (two-body) model for dynamics propagation. Required thrusts for the maneuver are calculated by the flight control system based on the State Dependent Riccati Equation (SDRE) technique. The output thrusts will be delivered to the remote control system to generate the motion command of deputy spacecraft, which will be passed back to the simulator system by TCP/IP socket. As an option, the STK mission visualization system can display the satellite formation flying scenario in real time mode or replay mode.

Pure software simulations were conducted on a MATLAB platform to test the flight control system by deactivating the GNSS measurement system and the EFK of the Navigation & Control system. In this way, the predicated states from the dynamics propagator were directly used to estimate the relative states. Once the feasibility of the dynamics propagator and flight control system are validated, the closed-loop HIL simulation would be conducted to test the reference scenario of spacecraft formation flying. The simulation results will be compared to reference [5] in order to evaluate the preformation of the VTFFTB.

GNSS is not only a tool for positioning or navigation, but it also has a variety of applications including upper atmosphere study, cartography, accurate clock development, tectonics and so on. The upper atmosphere (especially the ionosphere) has significant impact on GNSS signals. Inversely, GNSS can be used to study space weather including the ionosphere. Total Electron Content (TEC) is the integration of electron density along the sight of view between two points. By taking advantage of the dual-frequency radio wave transmission, the ionospheric TEC can be measured by calculating the difference in radio frequency (RF) signal delays between different frequency GNSS signals propagating through the ionosphere. The multi-constellation GNSS TEC measurement and model evaluation system including GPS, GLONASS, Galileo and Beidou constellations has been established. When a RF signal propagates through ionospheric irregularities, the rapid fluctuation of signal phase and/or amplitude is called ionospheric scintillation. A subsystem of multi-constellation multi-frequency GNSS scintillation monitoring has been developed to study the mid-latitude GNSS scintillation and ionospheric irregularities. Ground-based mid-latitude scintillation of GPS (L1, L2 & L5 bands), GLONASS (L1 & L2 bands) and Galileo (E1, E5a & E5b bands) constellations can be observed at Virginia Tech. These two systems can be integrated into the spacecraft formation flying testbed to design and develop GNSS-based spacecraft formation flying remote sensing missions to survey the ionosphere and study the ionospheric irregularities. This work will demonstrate how to

apply spacecraft formation flying to ionospheric remote sensing by simulating a scenario to detect a type of ionospheric irregularities called Sporadic E.

The subsequent sections of this thesis will be organized as follows: Chapter 2 gives an overview of the coordinate systems that will be used in this work, highlights the basic GNSS theories, as well as the fundamentals of spacecraft formation flying, and a brief review of the past work on HIL satellite formation flying; Chapter 3 introduces the hardware systems of the VTFFTB, including the GNSS simulators, multi-frequency multi-constellation GNSS Receivers and a Dell laptop with the navigation & control system. The concepts and setup of GNSS-based HIL simulation testbed will be illustrated in detail; Chapter 4 focuses on the software algorithm of the navigation & control system. The design methodology of each subsystem will be introduced and explained, which include the hardware communications in Section 4.2, dynamics propagator in Section 4.3, concepts of Differential GPS Measurement in Section 4.4, set up of the Extended Kalman Filter in section 4.5 and the SDRE Controller in section 4.6; Chapter 5 presents and analyzes the results of both software and hardware simulation, as well as validates the performance of the developed GNSS-based HIL spacecraft formation flying testbed by comparing to the results of reference [5]; Chapter 6 introduces the multi-constellation GNSS TEC measurement and model evaluation system and then demonstrates how to apply the spacecraft formation flying to ionospheric remote sensing by simulating a scenario of Sporadic E detection. The subsystem of multi-constellation multi-frequency GNSS scintillation monitoring will also be briefly introduced in section 6.3; The last chapter summarizes the current accomplishments and issues. Finally, future work is outlined.

Chapter 2

Basics of GNSS and Formation Flying

2.1. Coordinate Systems

Five different coordinate systems (reference frames) involved in this work are overviewed as follows:

1) Earth Centered Inertial (ECI) Frame: a Cartesian, rectangular, inertial coordinate system originates at the center of mass of the Earth. The unit vector $\hat{x}$ is directed from the center of the Earth along the vernal equinox; the unit vector $\hat{z}$ is perpendicular to the equatorial plane of the Earth with the positive direction toward the geographic North Pole; and the unit vector $\hat{y}$ is $\hat{z}\times\hat{x}$ (see Fig. 2.1).

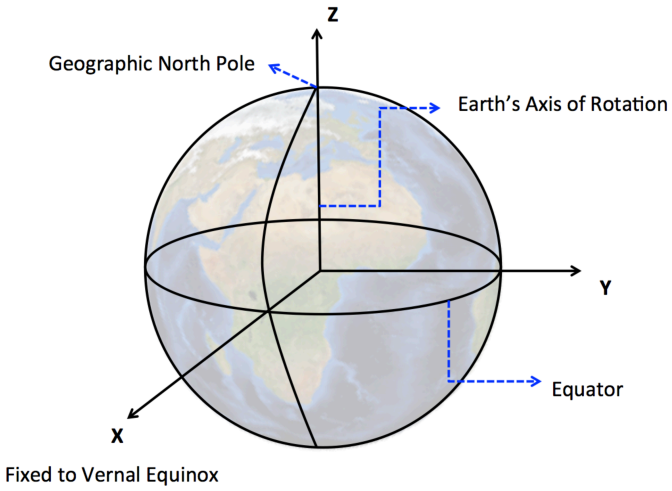

Figure 2.1. ECI Coordinate Frame

2) Earth Centered Earth Fixed (ECEF) Frame: a Cartesian, orthogonal, rotating coordinate system originates at the center of mass of the Earth. The unit vector $\hat{x}$ is directed from the center of the Earth to 0° latitude and 0° longitude (the intersection of the equator and the prime meridian in Greenwich). The unit vector $\hat{z}$ is perpendicular to the equatorial plane of the Earth with the positive direction toward the geographic North Pole. And the unit vector $\hat{y}$ is $\hat{z}\times\hat{x}$ (see Fig. 2.2). Note that, ECEF frame is one of the two standard reference frames for GNSS system users.

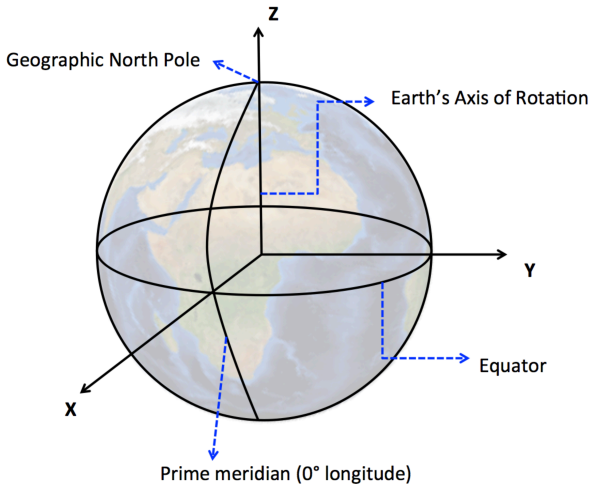

Figure 2.2. ECEF Coordinate Frame

3) World Geodetic Survey 1984 (WGS-84) Frame: an ellipsoidal approximation coordinate system originating at the center of mass of the Earth. It's the projection of ECEF onto the Earth's surface to pinpoint the latitude, longitude and altitude. Also, WGS-84 frame is one of the two standard reference frames for GNSS users. Because the Earth is not a pure sphere, the conversion between ECEF frame and the WGS-84 frame requires some extra attentions.

4) Local-Vertical, Local-Horizontal (LVLH) or Body Frame: a coordinate system originates at the center of mass of the spacecraft, which is often used to describe the relative dynamics of spacecraft formation flying. In the circumstance of two spacecraft formation flying, the (center of mass of) chief spacecraft will usually be assumed as the center of this reference frame. The unit vector $\hat{e}_x$, as known as radial direction, is directed from the center of the Earth to the chief spacecraft position. The unit vector $\hat{e}_y$, as known as in-track/along-track direction, is directed along the velocity vector of the chief satellite. The unit vector $\hat{e}_z$, as known as cross-track direction, is perpendicular to the orbital plane of the chief satellite with the positive direction along with the angular momentum vector. (See Fig. 2.3)

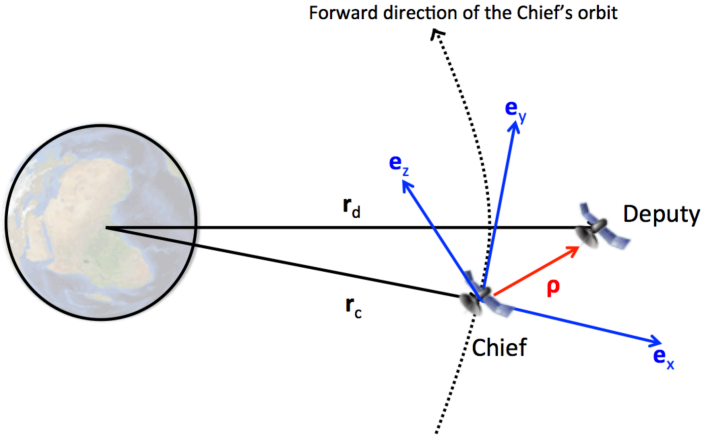

Figure 2.3. Body Frame

5) Classical Orbital Elements (COE) Frame: A set of elements consists of six basic parameters to describe the satellite orbit based on the Kepler's laws of planetary motion. The orbit of spacecraft can be completely determined if the initial position $\vec{r}_0$ and velocity $\vec{v}_0$ are specified at time t_0. Each vector consists of three scalars, hence the orbit can be described by six scalars, including three elements (Semimajor axis, Eccentricity and True anomaly) to determine the satellite motion in the orbital plane and three elements (Inclination, Longitude of the ascending node and Argument of perigee) to determine the orientation of the orbit in the space. (See Fig. 2.4)

1) **Semimajor axis (*a*)**: one half of the sum of the periapsis (perigee) and apoapsis (apogee) distances, which determines the size of the orbit.
2) **Eccentricity (*e*)**: eccentricity of the elliptical orbit, which determines the shape of the elliptical plane.
3) **True anomaly (ν)**: position of the orbiting body along the ellipse at the epoch time.
4) **Inclination (*i*)**: vertical tilt of the orbital plane with respect to the Earth's equatorial plane.
5) **Longitude of the ascending node** (Ω): horizontal angle measured counterclockwise (as seen from the north) from the ascending node of the equatorial orbit (the intersection of upward orbit and the Earth's equatorial plane) to the direction of First Point of Aries (vernal equinox)
6) **Argument of perigee** (ω): the angle between the ascending node and the perigee, which determines the orientation of the ellipse in the orbital plane

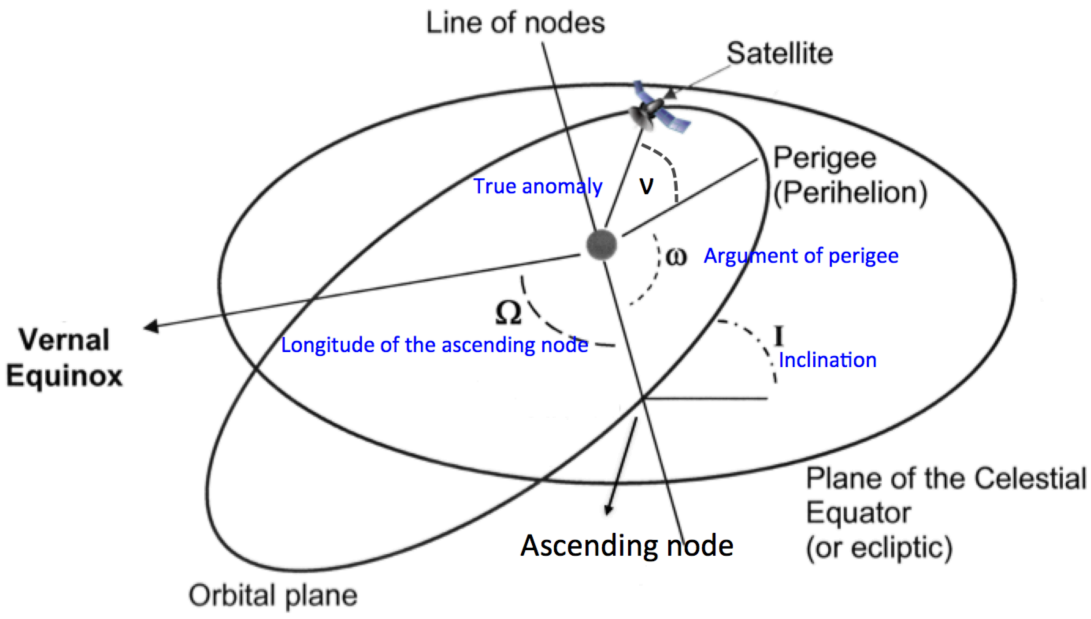

Figure 2.4. Classical Orbit Elements Frame

2.2. Fundamentals of GNSS

2.2.1. GNSS Positioning Principle

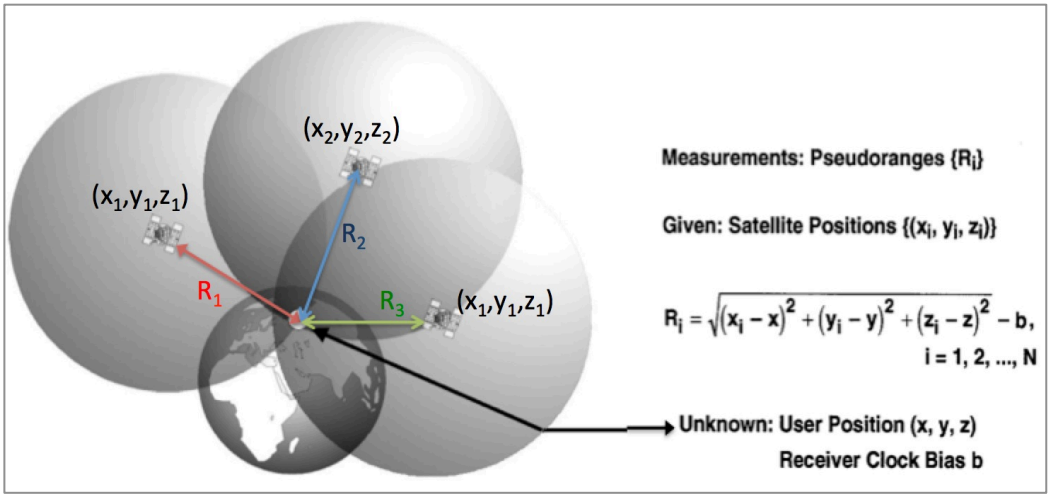

Figure 2.5. Illustration of the principle of trilateration for GNSS positioning

GNSS positioning is based on the principle of trilateration. Assume the velocity of signal propagating equals to the speed of light. And the propagating time can be obtained by reading the clock on the satellite and the receiver (object). Thus the distance *Ri* between the satellite and the object (the subscript *i* stands for the number of GNSS satellite) can be determined. If the satellite positions were known, the distance equations contain the object position and satellites' position can be set up as shown in Fig. 2.5. In the three-dimension world, using at least three equations to locate object by three different satellites at different places, the static position of the object can be calculated theoretically. However, since the time is also an unknown parameter in the equations because of the receiver clock bias, at least four GNSS satellites are needed to give navigation solution. This receiver clock bias is simply due to the fact that GNSS receivers use inexpensive clocks for consumer affordability, while the GNSS satellites use atomic clocks, which allow them to be synchronized to a very accurate time standard.

2.2.2. Basic GNSS Constellation Background

Currently fully operational GNSS constellations include the United States' Global Positioning System (GPS) and the Russian Global Navigation Satellite System (GLONASS). Two other global GNSS systems are expected to be fully operational by 2020 at the earliest: the European Union's satellite navigation system (Galileo) and Chinese global navigation satellite system (BeiDou/Compass).

As of April 2017, the GPS constellation is composed of 31 operational MEO satellites in six different orbital planes with an approximate inclination of 55 degrees and 60 degrees separation of longitude of the ascending node. The GPS satellite orbits are located about 20,200 km above the surface of the Earth with an orbital period about 12 hours. The GPS constellation is designed to have at least six satellites line-of-sight from almost everywhere on Earth's surface. Among those 31 GPS satellites, 19 satellites broadcast dual frequency signals: L1 (1575.42 MHz) and L2 (1227.6 MHz) and 12 satellites

broadcast three frequency signals: L1, L2 and L5 (1176.45 MHz). GPS RF signals are transmitted based on Code Division Multiple Access (CDMA) spread-spectrum technique.

As of April 2017, the GLONASS constellation is composed of 24 operational MEO satellites in three different orbital planes with an approximate inclination of 64.8 degrees and 120 degrees separation of longitude of the ascending node. The GLONASS satellite orbits are located about 19,100 km above the surface of the Earth with an orbital period approximately 11 hours 15 minutes. Unlike GPS, GLONASS satellites transmit the signal in two frequency bands (L1 and L2) with Frequency Division Multiple Access (FDMA) technique. Therefore, each satellite broadcast RF signals on its own carrier frequency. The L1 center frequency is 1602 MHz + n × 0.5625 MHz and L2 center frequency is 1246 MHz + n × 0.4375 MHz (where n is the satellite frequency channel number).

The Galileo constellation is scheduled to be composed of 30 operational MEO satellites in three different orbital planes with an approximate inclination of 56 degrees and 120 degrees separation of longitude of the ascending node. The GLONASS satellite orbits are located about 23,222 km above the surface of the Earth with an orbital period approximately 14 hours 7 minutes. As of April 2017, 12 Galileo satellites are operational in orbit and can be tracked by the users. Galileo satellites transmit signals in four radio frequency bands: E1 (1575.42 MHz), E5a (1176.45 MHz), E5b (1207.14 MHz) and E6 (1278.75 MHz). [6]

As of April 2017, there are 21 Beidou satellites in orbit operationally. The orbits of Beidou constellation are different from the other three GNSS constellations. The Beidou constellation is scheduled to be composed of 35 satellites to provide global coverage, including 5 GEO satellites, 27 MEO satellites and 3 Inclined Geosynchronous Orbit (IGSO) satellites. Beidou constellation can transmit RF signal in three frequency bands: B1 (1561.098 MHz), B2 (1207.14 MHz) and B3 (1268.52 MHz). [7]

	GPS	**GLONASS**	**Galileo**	**Beidou**
Owner	U.S.A 	Russia 	European Union 	China 
Orbit Altitude	MEO (~20,200 km)	MEO (~19,100 km)	MEO (~23,222 km)	GEO+MEO+IGSO
Number of Operational Satellites	31	24	12	21
Scheduled Total Number of Satellites	32	27	30	35
Transmit Frequencies	L1 (1575.42 MHz), L2 (1227.6 MHz), L5 (1176.45 MHz)	L1 (1602 MHz + n × 0.5625 MHz) and L2 (1246 MHz + n × 0.4375 MHz)	E1 (1575.42 MHz), E5a (1176.45 MHz), E5b (1207.14 MHz), E6 (1278.75 MHz)	B1 (1561.10 MHz), B2 (1207.14 MHz), B3 (1268.52 MHz)

Table 1. Comparison of main GNSS constellations

2.2.3. Ranging Errors and Pseudorange

Various ranging errors cause fundamental limitations on GNSS positioning accuracy. These limitations can be defined in the format of error budget as the GNSS observable pseudorange:

$$P = R + c(\Delta T + \Delta t) + \Delta_{ionosphere} + \Delta_{troposphere} + \Delta_{multipath} + \Delta_{DOP} + \Delta_{receiver} + \Delta_{other} \quad \textbf{(1)}$$

Where:
P = measured pseudorange (distance with error) in the unit of meters
R = the geometric range to the satellite (true distance without error)
c = speed of light in a vacuum
ΔT = satellite clock bias
Δt = receiver clock bias
$\Delta_{ionosphere}$ = ionospheric signal delay
$\Delta_{troposphere}$ = troposphere signal delay
$\Delta_{multipath}$ = multipath effect delay
Δ_{DOP} = errors caused by geometric dilution effect
$\Delta_{receiver}$ = receiver noise
Δ_{other} = others noise like relativity effect, selective availability, etc.

Ultimately, the better we estimate, measure or eliminate these error sources, the better the GNSS positioning accuracy would be. Precise navigation for spacecraft formation flying demands robust estimation of each ranging error.

2.2.4. Ionospheric Remote Sensing Using GNSS Beacons

Ionospheric irregularity is the small-scale region in the ionosphere with distinctly different plasma density. The irregularity result from plasma instabilities can be driven by combinations of plasma drifts, density and temperature gradients, electric fields and winds generating fluctuations in electron density [8]. The sizes of ionospheric irregularities range from centimeters to tens of kilometers. Depending on their scale sizes, ionospheric irregularities can be detected by a variety of ground-based (e.g. Radar) or space-based (e.g. satellite beacon) remote sensing techniques. The Earth's ionosphere with plasma irregularities/instabilities will impact GNSS signal propagation and cause ionospheric delays, signals scintillation, Faraday rotation and many other negatively effects.

The dispersion relation equation of electromagnetic waves propagating through the ionosphere, which is relevant to GNSS signals, can be expressed as [9]:

$$\frac{\omega^2}{c^2 k^2} = 1 - \frac{n_e q^2}{\varepsilon_0 m_e \omega^2} = 1 - \frac{\omega_p^2}{\omega^2} \quad \textbf{(2)}$$

Where:
n_e = electron density

k = wave number

ω = radian frequency of the wave

q = elementary charge $\approx 1.6\times10^{-19}$ C

ε_0 = permittivity of free space

μ_0 = permeability of free space

m_e = electron rest mass

$$c^2 = \frac{1}{\mu_0\varepsilon_0}$$

$$\omega_p \equiv q\sqrt{\frac{n_e}{\varepsilon_0 m_e}} \quad \text{(Plasma Frequency)}$$

From the dispersion relation Eq. (2), the phase velocity of radio wave can be derived as:

$$v_\phi = \frac{\omega}{k} = \frac{c}{\sqrt{1-\frac{n_e q^2}{\varepsilon_0 m_e \omega^2}}} = \frac{c}{\sqrt{1-\frac{\omega_p^2}{\omega^2}}} \tag{3}$$

Consider: $\omega = 2\pi f$. Therefore, the higher the signal frequency, the slower the phase velocity is.

Also, the group velocity of radio wave can be derived from Eq. (2):

$$v_g = \frac{\partial\omega}{\partial k} = c\sqrt{1-\frac{n_e q^2}{\varepsilon_0 m_e \omega^2}} = c\sqrt{1-\frac{\omega_p^2}{\omega^2}} \tag{4}$$

So, the higher the signal frequency is, the faster the radio wave group velocity is. And the slower the group velocity is, the larger the ionospheric delay is.

The carrier signals travel in phase speed, while the modulated signal travels in group velocity. So the information content of GNSS signals is propagated in v_g .

$$\text{Consider: } v_p = \frac{\omega}{k} = \frac{c}{n} \tag{5}$$

The index of refraction is given by:

$$n = \sqrt{1-\frac{\omega_p^2}{\omega^2}} \tag{6}$$

When the radio wave frequency is smaller than the plasma frequency, the index of refraction will become an imaginary number. This causes spatial decay of the radio waves. Hence, the radio wave cannot penetrate the plasma. For example, the lower frequency radio wave cannot propagate through

the relative “opaque” ionosphere. When the frequency radio wave is higher than the plasma frequency of the ionosphere, it can penetrate through the ionosphere. (As illustrated in Fig. 2.6)

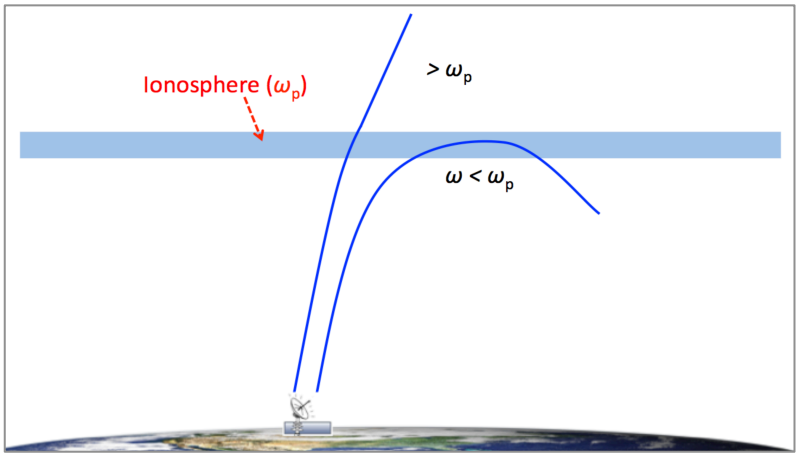

Figure 2.6. Radio wave propagation dependence on frequency

Total Electron Content (TEC) is a commonly used parameter for characterizing the Earth's ionosphere. It is defined as the total number of electrons within a cross-sectional volume along a path between two points and given in units of number of electrons / m^2. Ionospheric range delay is dispersive and thus depends on the frequency of the signal.

By considering two paths (one with ionospheric delay, one without ionospheric delay) of propagation, we can derive the ionospheric delay as a function of frequency:

$$\Delta_{ionosphere} \cong \frac{40.3}{f^2} \cdot \int_0^R n_e dr \quad \text{(where } TEC \equiv \int_0^R n_e dr\text{)} \tag{7}$$

Since TEC depends on altitude, longitude and latitude, ionospheric delay varies from height to height, from place to place. Ionospheric delays are estimated by transmitting GNSS signals in two or more frequencies. Consider ionospheric delay is a function of frequency and TEC from Eq. (7), and GPS satellites transmit in two frequencies (L1 & L2), we can get the difference in arrival time for two different band signals transmitted at identical times but at different frequencies:

$$\Delta(\delta t) = \frac{40.3 \times TEC}{c}\left(\frac{f_{L1}^2 - f_{L2}^2}{f_{L1}^2 f_{L2}^2}\right) \tag{8}$$

Because pseudorange $P = c \cdot \delta t$ (where δt is the time from the signal transmitted by the GNSS satellite to the signal received by the GNSS receiver), then:

$$TEC_{\text{pseudorange}} = \frac{1}{40.3}\left(\frac{f_{L1}^2 f_{L2}^2}{f_{L1}^2 - f_{L2}^2}\right)\left(P_{L1} - P_{L2}\right) \tag{9}$$

Based on Eq. (9), we can generate relatively fluctuated TEC plot (as shown as the blue plot in Fig. 2.7), which is called pseudorange/code TEC.

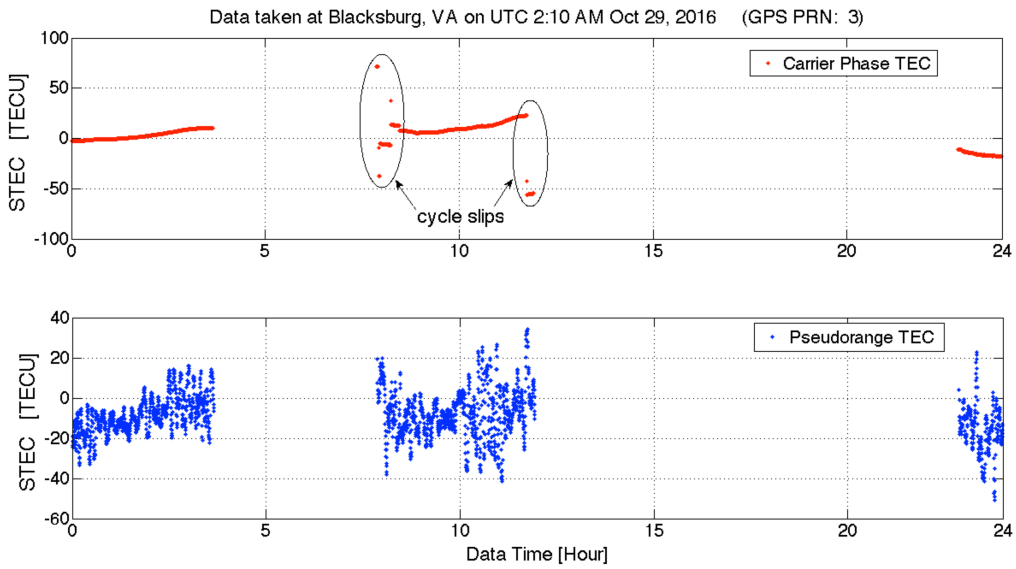

Figure 2.7. Pseudorange TEC (blue) and carrier phase TEC (red) plots with feature of cycle slips

Another GNSS observable carrier phase CP (in the unit of number of cycle) is defined as:

$$CP = R + c(\Delta T + \Delta t) + N - \Delta_{ionosphere} + \Delta_{troposphere} + \Delta_{multipath} + \Delta_{DOP} + \Delta_{receiver} + \Delta_{other} \quad \textbf{(10)}$$

(where N is the ambiguity)

The carrier phase is the time integration of Doppler frequency plus the ambiguity of phase (i.e. initial phase). It is a relative phase measured in the unit of cycles, which is equivalent to the number of wavelengths of the propagating signals starting from the reference of first tracking. Smooth TEC is measured by calculating the difference in carrier phase delays between different frequency signals propagating through the ionosphere, which can be written in this expression.

$$TEC_{\text{carrier phase}} = \frac{c}{40.3}\left(\frac{f_{L1}^2 f_{L2}^2}{f_{L1}^2 - f_{L2}^2}\right)\left(\frac{CP_{L2}}{f_{L2}} - \frac{CP_{L1}}{f_{L1}}\right) \quad \textbf{(11)}$$

As shown as the red plot in Fig. 2.7, the carrier phase TEC is much smoother than pseudorange TEC but there might be cycle slips exist in the carrier phase TEC caused by GNSS scintillation.

For an undisturbed ionosphere, ionospheric delay is the only effect that impacts the GNSS signals passing through the ionosphere. However, the GNSS signals can be perturbed by electron density fluctuations in the ionosphere that might cause phase and/or amplitude fluctuations in the received signal, known as GNSS scintillations. Subsequently, differential scattering of the plane wave produces phase variations along the phase front of the signal. As the signal propagation continues after passing through the ionospheric irregularity regions, phase or amplitude scintillation develops through constructive and destructive interference of multiple scattered signals.

Serious GNSS scintillations present additional stresses to the tracking loop of GNSS receiver, which

can induce cycle slip, a discontinuity or a jump in carrier phase measurements. In such circumstances, a sudden fluctuation of carrier phase TEC in a short amount of time can be noticed as shown in Fig. 2.7. Or even worse case of scintillations would cause receivers to stop tracking the signals from GNSS satellites, which is known as loss of lock.

2.3. Fundamentals of Spacecraft Formation Flying

2.3.1. Definition of Spacecraft Formation Flying

Spacecraft formation flying may have a number of definitions depending on the application. For the type of application in this thesis, the NASA's Goddard Space Flight Center (GSFC) definition is used:

Spacecraft Formation Flying is "tracking or maintenance of a desired relative separation, orientation or position between or among spacecraft" [10]. In other words, spacecraft formation flying refers to maintaining the relative motion of spacecraft with respect to a reference spacecraft in a specific configuration.

2.3.2. Spacecraft Formation Flying Missions

There are a variety of applications for spacecraft formation flying. On one hand, it's a very critical technique for spacecraft missions. For instances, rendezvous or docking, satellite deployment, spacecraft assembly or even spacewalk for extravehicular activity. One the other hand, spacecraft formation flying enables the collaboration of a group of similar, agile satellites for high resolution space environment sounding or measurement. As one of the pioneering spacecraft formation flying missions, European Space Agency (ESA)'s CLUSTER II mission launched a constellation of four identical spacecraft into highly elliptical polar orbits around the Earth in 2000, to observe the Sun-Earth electromagnetic interactions by making three-dimensional in-situ measurements [11].

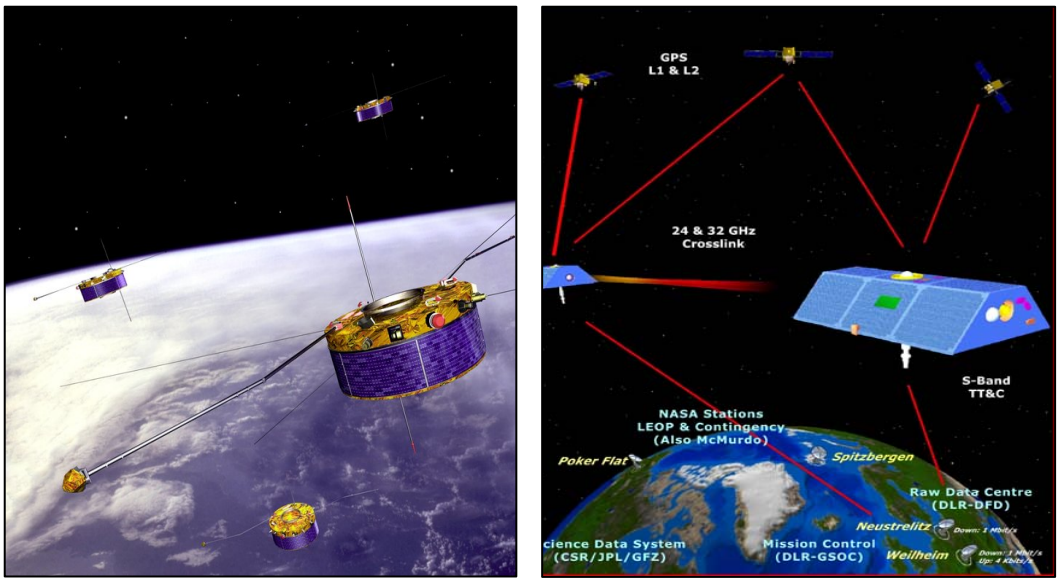

Figure 2.8. Left: CLUSTER II mission [11]; Right: GRACE mission [12]

Another pioneering spacecraft formation flying mission, Gravity Recovery And Climate Experiment (GRACE), a joint mission of NASA and the German Aerospace Center (DLR), launched two identical satellites with an in-track separation of 220 km in March 2002 with the primary mission object to map the Earth's gravity field in high level of accuracy and generate high-fidelity gravitational field model of the Earth [12]. Eleven years later, ESA's SWARM mission launched a constellation of three satellites to survey the Earth's magnetic field with a higher level of precision and resolution [13].

NASA's Magnetospheric Multiscale Mission (MMS) mission is a spacecraft formation flying space mission to study the Earth's magnetosphere. MMS consists of four identical spacecraft that are formed into a variably spaced tetrahedron configuration in an attempt to perform three-dimensional space weather tomography observation. On September 2016, MMS spacecraft achieved as close as only four-and-a-half miles with each other in a pyramid shape formation [14].

Furthermore, the mission architecture of multiple satellites orbiting close together opens a new door for the space scientist and engineers to design next generation novel space missions. Examples of such missions include Stellar Imager (SI), Milli-Arc-Second Structure Imager (MASSIM), and Black Hole Imager. All of these future NASA formation flying astrophysical missions are planned to be launched in the third decade of the 21st century [10][15]. Stellar Imager (SI) mission envisions to build a space-based ultraviolet/optical interferometer; Milli-Arc-Second Structure Imager (MASSIM) mission and Black Hole Imager mission plan to design ultra-high angular resolution X-ray astronomy space-based telescope. Moreover, asteroid miners are seeking to utilize spacecraft formation flying techniques to capture asteroids [16].

2.3.3. Orbital Mechanics Overview

Consider a scenario of two spacecraft formation flying: one chief satellite and another deputy satellite orbiting the Earth in proximity to each other. To establish the relative dynamics model, let's assume:

- Earth is a perfect sphere.
- The Earth and the two spacecraft are treated as point mass.
- No external disturbances (e.g. Sun, Moon, etc.) or internal thrust (i.e. no control)
- Spacecraft follow Kepler's laws of planetary motion.
- Chief satellite obeys circular motion (eccentricity $\approx$ 0)
- The separation between chief and deputy is much less than the orbital radius of chief.

Starting from the relative position in the body frame (See Fig. 2.9):

$$\vec{r}_d = \vec{\rho} + \vec{r}_c \quad \text{(Where } \vec{\rho} = x\hat{e}_x + y\hat{e}_y + z\hat{e}_z \text{, } y\hat{e}_y \simeq r_c\delta\theta\hat{e}_\theta \text{ and } \vec{r}_c = r_c\hat{e}_x \text{)} \tag{12}$$

The position of deputy satellite can be expressed as:

$$\vec{r}_d = \left(r_c + x\right)\hat{e}_x + y\hat{e}_y + z\hat{e}_z \tag{13}$$

Since r_c is a constant (because of the circular motion of chief satellite), the derivations of $\vec{r}_d$ in the body frame are:

$$\frac{^{body}d}{dt}\vec{r}_d = \dot{x}\hat{e}_x + \dot{y}\hat{e}_y + \dot{z}\hat{e}_z \tag{14}$$

$$\frac{^{body}d^2}{dt^2}\vec{r}_d = \ddot{x}\hat{e}_x + \ddot{y}\hat{e}_y + \ddot{z}\hat{e}_z \tag{15}$$

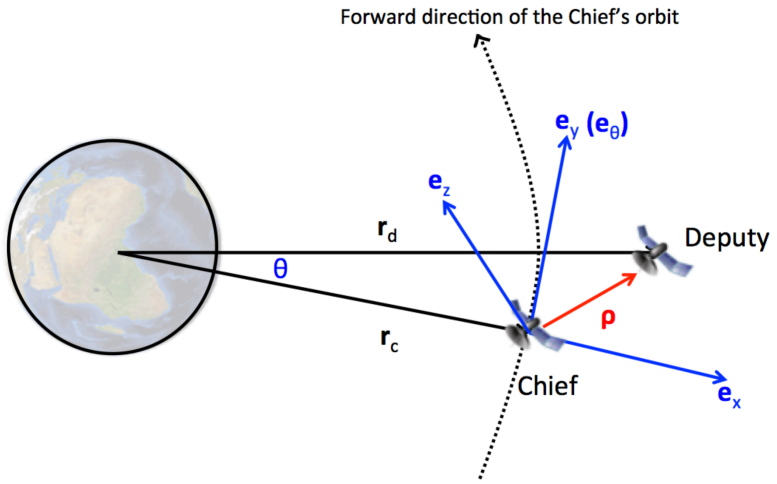

Figure 2.9. Two spacecraft formation flying in the body frame

The chief satellite is the origin (reference point) of the body frame. The body frame rotates the center of ECI frame at an angular velocity equals to the mean motion of chief satellite:

$$\vec{\omega}^{body\_to\_ECI} = n_0\hat{e}_z \tag{16}$$

Therefore the second order inertial derivative is:

$$\ddot{\vec{r}} = \frac{^{body}d^2}{dt^2}\vec{r}_d + 2\vec{\omega}^{body\_to\_ECI} \times \frac{^{body}d}{dt}\vec{r}_d + \left(\dot{\vec{\omega}}^{body\_to\_ECI} \times \vec{r}\right) + \vec{\omega}^{body\_to\_ECI} \times \left(\vec{\omega}^{body\_to\_ECI} \times \vec{r}\right) \tag{17}$$

Substitute the Eq. (13) - Eq. (15) into right hand side of Eq. (17), we can get the deputy acceleration:

$$\begin{aligned}\ddot{\vec{r}}_d &= \left(\ddot{x}\hat{e}_x + \ddot{y}\hat{e}_y + \ddot{z}\hat{e}_z\right) + 2\left(n_0\hat{e}_z\right) \times \left(\dot{x}\hat{e}_x + \dot{y}\hat{e}_y + \dot{z}\hat{e}_z\right) + \left(\dot{n}_0\hat{e}_z \times \left(\left(r_c + x\right)\hat{e}_x + y\hat{e}_y + z\hat{e}_z\right)\right) \\ &+ \left(n_0\hat{e}_z\right) \times \left(n_0\hat{e}_z \times \left(\left(r_c + x\right)\hat{e}_x + y\hat{e}_y + z\hat{e}_z\right)\right) \\ &= \ddot{x}\hat{e}_x + \ddot{y}\hat{e}_y + \ddot{z}\hat{e}_z + 2n_0\dot{x}\hat{e}_y - 2n_0\dot{y}\hat{e}_x - n_0^2\left(r_c + x\right)\hat{e}_x - n_0^2 y\hat{e}_y - \dot{n}_0 y\hat{e}_x + \dot{n}_0 x\hat{e}_y\end{aligned}$$

Express in the body frame format:

$$\ddot{\vec{r}}_d = \left[\ddot{x} - 2n_0\dot{y} - n_0^2\left(r_c + x\right) - \dot{n}_0 y\right]\hat{e}_x + \left(\ddot{y} + 2n_0\dot{x} - n_0^2 y + \dot{n}_0 x\right)\hat{e}_y + \left(\ddot{z}\right)\hat{e}_z \tag{18}$$

Next, the two-body Keplerian motion equation gives the acceleration of deputy satellite as:

$$\ddot{\vec{r}}_i = -\frac{\mu \vec{r}_i}{r_i^3}, \qquad (i = \mathrm{c}, \mathrm{d}) \tag{19}$$

(where μ is the standard gravitational parameter of the Earth)

Substitute the Eq. (17) into the acceleration we get:

$$\ddot{\vec{r}}_d = -\frac{\mu \vec{r}_d}{r_d^3} = -\frac{\mu\left[\left(r_c + x\right)\hat{e}_x + y\hat{e}_y + z\hat{e}_z\right]}{\left[\left(r_c + x\right)^2 + y^2 + z^2\right]^{3/2}} = -\frac{\mu\left[\left(r_c + x\right)\hat{e}_x + y\hat{e}_y + z\hat{e}_z\right]}{\gamma} \tag{20}$$

Component-wise, equal Eq. (18) and Eq. (20), can get the following nonlinear, time-varying differential equations:

$$\ddot{x} - 2n_0\dot{y} - \dot{n}_0 y - n_0^2\left(r_c + x\right) + \frac{\mu\left(r_c + x\right)}{\gamma} = 0 \tag{21}$$

$$\ddot{y} + 2n_0\dot{x} + \dot{n}_0 x - n_0^2 y + \frac{\mu y}{\gamma} = 0 \tag{22}$$

$$\ddot{z} + \frac{\mu z}{\gamma} = 0 \tag{23}$$

When the chief orbit is circle (eccentricity ≈ 0), the mean motion of chief satellite can be approximated as first order derivative of true anomaly:

$$n_0 \simeq \sqrt{\frac{\mu}{r_c^3}} = \dot{\nu} \tag{24}$$

Finally, after substituting Eq. (24) into Eq. (21) and Eq. (22), we can obtain the set of nonlinear equations of relative motions, as known as the Hill's (Clohessy-Wiltshire) equations:

$$\ddot{x} - 2\dot{\nu}\dot{y} - \ddot{\nu} y - \dot{\nu}^2 x - \frac{\mu}{r_c^2} + \frac{\mu\left(r_c + x\right)}{\gamma} = 0 \tag{25}$$

$$\ddot{y} + 2\dot{\nu}\dot{x} + \ddot{\nu} x - \dot{\nu}^2 y + \frac{\mu y}{\gamma} = 0 \tag{26}$$

$$\ddot{z} + \frac{\mu z}{\gamma} = 0 \tag{23}$$

The Hill's equations will be used to calculate the thrust required to control the relative motion later in the flight control system, which will be discussed in the session 4.6.

To determine the value of true anomaly ν, we need to numerally solve for Kepler's Equation to get the eccentric anomaly E:

$$E - e\sin E = \sqrt{\frac{\mu}{a^3}}\left(t - T_0\right) \tag{27}$$

To find the root of E in the equation above, we need to solve the transcendental function above using numerical algorithm. Once getting the solution of E, we can calculate the true anomaly as follow:

$$\nu = 2\tan^{-1}\left[\sqrt{\frac{1+e}{1-e}}\tan\left(\frac{E}{2}\right)\right] \tag{28}$$

2.4. Past HIL Spacecraft Formation Flying Simulations

Research of spacecraft formation flying simulation can be dated back to 1990s. In 1996, Guinn and Boain [17] at NASA's Jet Propulsion Laboratory (JPL) performed GPS-based simulation of spacecraft formation flying to support the New Millenium Earth Orbiter-1 (EO-1) mission. Another pioneering spacecraft formation flying mission, TechSat-21, was a revolutionary space mission architecture proposed by the U.S. Air Force Research Laboratory in late 1990s to form a large sparse aperture imaging system using multiple small satellites flying in formation [10]. TechSat-21 mission also carried an innovative concept of upgrading the system performance of the small satellites clusters over time through post-phased deployment or evolution. However, TechSat-21 project was terminated in 2003 due to research complexity and financial issues.

The robustness of spacecraft formation flying mission highly depends on the performance of the Guidance, Navigation and Control (GNC) algorithm. GNSS-based Hardware-In-the-Loop (HIL) simulation provides a testbed to analyze and validate the functionalities of GNC algorithm, which is advantageous to mission development in the hardware level before the launch. As one of the leading researcher facilities on GNSS-based HIL spacecraft formation flying simulation, NASA's GSFC had built the Formation Flying Test Bed (FFTB) since early 2000s to support their satellite formation flying mission deign, validation and development. In 2001, Leitner [18] firstly established the FFTB, a GPS-based HIL simulation platform for formation flying clusters and constellations of satellites. The FFTB developed by Leitner consists of 10 components: Central Simulation Controller, Intersatellite Communication Subsystem, On-board Processing Subsystem, Ground Control and Telemetry Subsystem, Navigation Subsystem, Guidance and Trajectory System, Environment Subsystem, Vehicle Control Subsystem, Health and Status Subsystem and Formation Flying Executive. Such comprehensive and sophisticated infrastructure allows the testbed to support various different level or type of experiments with respect to each individual subsystem. For instance, the Environment Subsystem is capable of modeling the space environment (ionosphere and atmosphere) and its impact on satellites communications. The implementations of the FFTB were directly applied to some of the GPS-based-navigation space missions such as University NanoSats, TechSat21 and MMS. In 2002, Gill et. al. [19] used the FFTB to demonstrate real-time HIL simulation for

GPS-based autonomous formation flying. Orion GPS receivers were used to perform a 12-hour experiment of two near-polar LEO micro-satellites scenario. Initially the in-track separation of the two satellites was 800m and the goal was to maintain a 100m in-track separation. A formation keeping accuracy of about 3 m (3D root mean square, RMS) has been achieved for the scenario. The feasibility of 50-m minimum separation has been demonstrated by simulations as well.

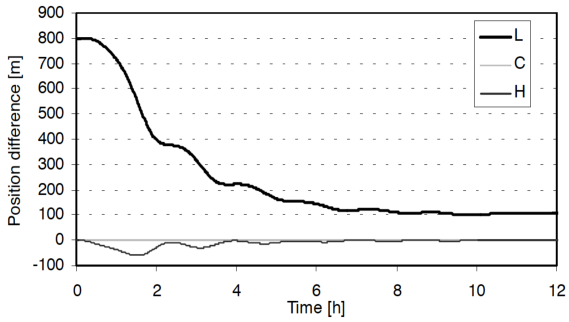

	L [m]	C [m]	H [m]	R [m]
Minimum	100.3	-0.1	-2.7	100.3
Maximum	111.1	0.1	1.5	111.1
Mean	106.2	0.0	-0.3	106.2
RMS	2.8	0.1	1.1	2.8

Figure 2.10. Result of HIL formation flying in reference [19] (Left: Relative Position; Right: characteristics of formation keep in L/in-track, C/cross-track, H/radial and R/relative directions)

In 2004, Burns et. al. [20] upgraded the FFTB and perform further formation control simulations. Spirent STR4760 GPS simulator was used and a visualization subsystem based on Satellite Tool Kit (STK) was added. Both pure software simulation and HIL simulation were performed. Simulation results showed that, the HIL mean range error is about 2.5 times worse than the pure software result. In 2005, Mohiuddin and Psiaki [21] used the FFTB at GSFC to test and evaluate a newly developed satellite relative navigation estimator based on carrier-phase differential GPS (CDGPS) technique. Their new estimation algorithm can achieve (3D RMS) accuracy of less than 3 mm over a 1km baseline LEO scenario. Later on, Mohiuddin and Psiaki tested more relative navigation estimators under few special scenarios like high-altitude orbit [22] or scintillation condition [23] using GSFC's FFTB.

In 2005, Leung and Montenbruck [24] used the closed-loop GPS-based HIL spacecraft formation flying testbed developed at DLR to validate the real-time performance of a GPS relative navigation algorithm. The DLR testbed used a Spirent STR4760 GPS simulator and an Orion-S GPS receiver. The simulation result of a four spacecraft scenario has accomplished relative position accuracy of 1.5 mm over a 4-km baseline. In 2008, Yamamoto and D'Amico [25] at DLR presented a closed-loop testbed for GPS-based HIL autonomous formation flying of LEO satellites. The experiment was to support the test campaign of PRISMA, a Swedish micro-satellite mission aiming for formation flying technologies development. The testbed included a Spirent GPS simulator and two Phoenix GPS receivers. The PRISMA GPS-based GNC flight software was conducted in a MATLAB/Simulink platform and tested and validated in their HIL testbed. After 24-hour simulation, the statistical accuracy of absolute navigation is 2.7m and relative navigation is 5.5cm (3D RMS).

Besides research facilities like NASA or DLR, several other universities have also developed GNSS-based HIL testbed to study relative navigation or design robust control system for spacecraft formation flying. In 2003, Ebinuma et. al. [26] from the University of Texas at Austin constructed a closed-loop HIL system for two satellites rendezvous simulation using single-frequency Orion GPS

receivers and STR4760 GPS simulator. The closed-loop simulation of reference [26] achieved 3.5 cm or less relative position accuracy and 1.0 mm/s relative velocity accuracy without the impact of multipath effect. In 2008, Marji [27] at University of Calgary developed a HIL testbed with a Spirent STR4760 GPS Simulator and two Novatel OEM4-G2L GPS Receivers and applied it for GPS-based CDGPS precise relative navigation for LEO satellite formation flying. The simulations of reference [27] achieved 4 mm relative position accuracy and less than 3 cm/s relative velocity accuracy with 1-km baseline, and 2-3 mm and less than 2.5 cm/s with 100 m baseline. In 2009, Eyer [28] at University of Toronto developed a GPS-based HIL testbed using a Novatel GPS simulator and Novatel OEMV GPS receivers to support CanX-4&5 program, a nanosatellites mission to accomplish autonomous spacecraft formation flying precisely with low cost.

In 2009, Park et. al. [5] at Yonsei University established a GPS-based HIL satellite formation flying simulation testbed and developed the algorithm for real-time relative navigation and formation control. Their closed-loop 1-hour simulations have evaluated the performance of the algorithm and demonstrated the relative position accuracy of 7 cm (3D RMS) for a two LEO satellites scenario with a 100 m baseline. Because of the similarity of infrastructure, reference [5] is used as the paradigm for testbed development. Further benchmarking will be conducted in detail throughout this thesis.

In 2007, Kowalchuk focusing on robust controller design, considered GPS-based closed-loop HIL formation flying simulations of two LEO spacecraft, in order to develop the Distributed Spacecraft Attitude Control System Simulator (DSACSS) testbed [2]. Kowalchuk's configuration of GPS-based HIL simulation at Virginia Tech used two Spirent GSS6560 simulators and Ashtech G12 GPS receivers [2]. In 2016, Harris at Virginia Tech developed a GPS-based HIL testbed to simulate scenarios of car, airplane and satellites [29]. By testing the formation and tracking control algorithms in the testbed, Harris made significant progress on the development of GNSS-based spacecraft formation flying simulation testbed.

This work is the first fully operational GNSS-based spacecraft formation flying simulation testbed at Virginia Tech with real time HIL capability with the implement of SDRE technique for dynamics control and EFK for relative states estimation.

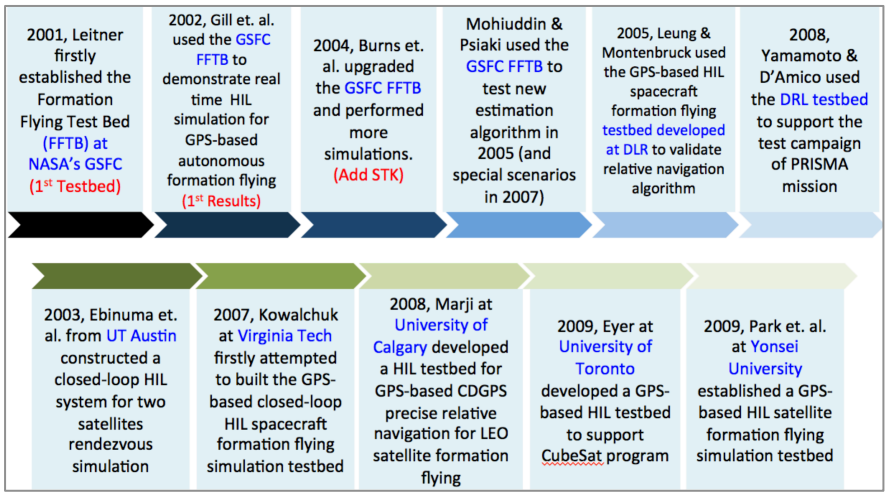

Figure 2.11. Important milestones of GPS-based HIL spacecraft formation flying testbed development

Chapter 3

Hardware Overview of Formation Flying Testbed

3.1. GNSS Simulators

As the core equipment of the closed-loop HIL testbed system for spacecraft formation flying simulation, GNSS simulators can create GNSS signals that are emulated to be as representative as possible of the signals that would actually be incident at the antenna of a GNSS receiver under specific scenarios. Developed by Spirent Communications, the GNSS simulators are compromised of RF signal generator(s) and operational computers with proprietary software. As shown in Fig. 3.1, GSS8000 GNSS RF signal generator and GSS7800 Galileo RF signal generator are synchronized to the Spirent simulator operational computer 2, while another GSS8000 RF signal generator is connected to the operational computer 1.

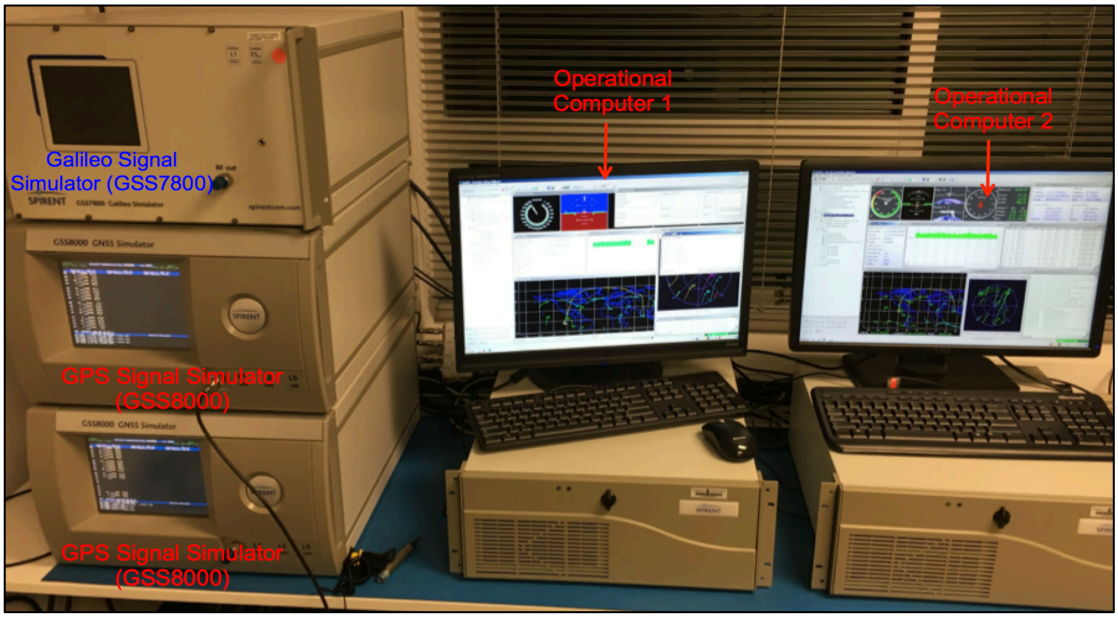

Figure 3.1. Spirent GNSS simulators and operational computers

GSS8000 GNSS simulator can emulate and output GPS-only RF signals, while GSS7800 Galileo simulator is capable of simulating RF signals of Galileo constellation. This work mainly focuses on GPS simulation. GSS8000 has two RF outputs (both output can generate L1, L2 and L5 frequency bands GPS signals) that can feed two receivers simultaneously with one antenna each. The normal power level output can generate RF signals from -49 dBm to +20 dBm, while the other higher power level output can export RF signals from -49 dBm to +25 dBm [30]. The simulator supports up to 48 channels in a chassis. Plus up to 192 additional programmable multipath channels, there are 240 channels per chassis in total. GSS8000's "high dynamic" capability allows user to run the simulation in 250 Hz (4 ms), 100Hz (10ms) or 10Hz (100ms) simulation iteration rate (SIR). SIR of 10 Hz (100ms) was selected to conduct the HIL simulation in this work.

The primary simulation software on the operational computer, known as “SimGEN” or “PosApp”, is synchronized with the hardware simulators via TCP/IP and used to control and customize the simulation under a graphical user interface (GUI) program.

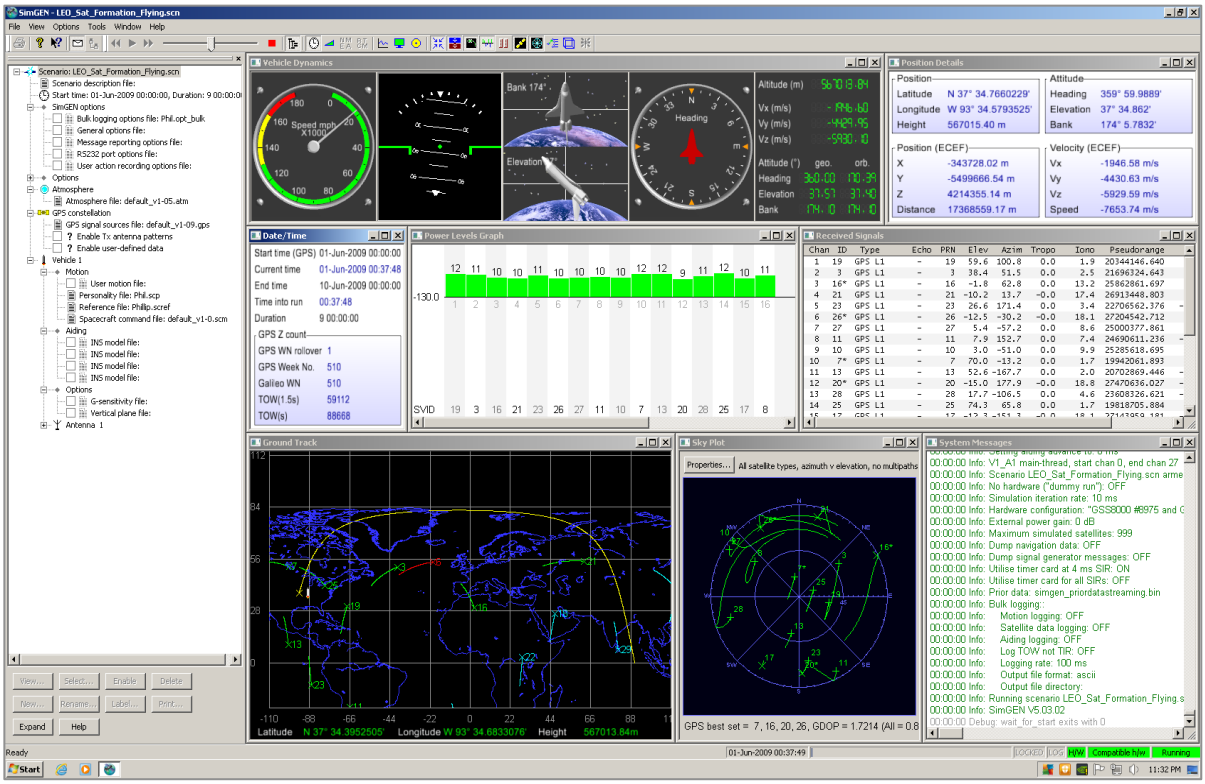

Figure 3.2. SimGEN interface with a spacecraft scenario

SimGEN provides the platform to create and design the scenario for the simulation. Available vehicle models include static location, simple motion, aircraft, land vehicle, ship, spacecraft or remote control. Depends on the application, you can customize the antenna pattern, RF output power level, or model the ranging errors including multipath, ionospheric impact (TEC, scintillation), tropospheric impact and so on. Also, users can update the GNSS constellation status by uploading the latest almanacs or even manipulate the GNSS constellation, say extending the total number of GPS satellites or modify their orbits.

An important feature of SimGEN is it allows external motion control for the remote vehicle in real time, which enables the closed-loop HIL development. This feature is called “SimGEN Remote” and it allows the users of SimGEN Remote have a large degree of freedom to design the motion or trajectory of any vehicle externally (e.g. using MATLAB). However, there are certain timing rules and dynamics restrictions in SimGEN, which require extra attention when users propagate the remote vehicle in the scenario. In the end of the simulation, the Data Logging function in SimGEN allows users to record the motion data for the spacecraft, which will be used to compare with the data measured by receivers or the estimation results output from the EFK in the control system. In this way, the navigation errors can be estimate and used to evaluate the simulation performance.

3.2. GNSS Receivers

Figure 3.3. Novatel GNSS receivers (Left: OEM628; Right: GPStation-6)

Two Novatel GNSS receivers are used in this work: OEM628 and GPStation-6. RF coaxial cables are used to connect the GNSS receivers with GNSS simulators for HIL simulation testbed development, or the outdoor GNSS antenna to receive real-world GNSS signals. By using supporting software Novatel Convert, Standard GNSS observation or navigation file can be outputted in the format of Rinex (version 2.10, 3.01 or 3.02), and the log data upon request can be converted into ASCII file.

Novatel OEM628 is an advanced multi-frequency multi-constellation GNSS receiver. As shown in the Fig. 3.3 (left), OEM628 receiver is compromised of a Triple-frequency plus L-Band GNSS receiver board on top of an OEM Development Kit. This 120-channel receiver is capable of tracking all current and upcoming GNSS constellations satellite signals including GPS, GLONASS, Galileo and BeiDou with maximum data logging rate of 100Hz [31]. Note that, the limit of high altitude and high velocity on this OEM628 receiver has been turned off. So it is able to provide navigation solutions for LEO spacecraft.

As shown in Fig. 3.3 (right), Novatel GPStation-6 is a multi-frequency multi-constellation GNSS receiver with advanced features of TEC and scintillation motioning. This model of GPStation-6 can track the satellite signals from GPS, GLONASS and Galileo constellations for up to 120 channels in total [32]. Maximum data logging rate is 50 HZ, including phase and amplitude sampling. It can generate 1 Hz raw pseudorange TEC and smoothed carrier phase TEC using Kalman Filter in 15 seconds interval. Auto calibration for differential receiver code bias can be applied on the TEC outputs. The receiver can also process the measurement data and directly output amplitude and phase scintillation indices for the users. Note that, this GPStation-6 receiver has limits on altitude and velocity so it's not able to provide navigation solution for LEO spacecraft. Therefore a primary application of the GPStation-6 receiver in this work is to study the localized ionospheric impacts on GNSS signals, and then provide the benchmarking for TEC and scintillation software development on OEM628 receiver.

3.3. Experiment Concepts of Hardware-in-the-Loop Simulation and Testbed Setup

3.3.1. Open loop vs. Closed-loop HIL Simulation

There are two types of system configuration of Hardware-in-the-loop Simulation: open-loop and closed-loop. The open-loop configuration doesn't execute any maneuvers or control on the target spacecraft during the simulation, so the data flow is single-direction as shown below in Fig. 3.4.

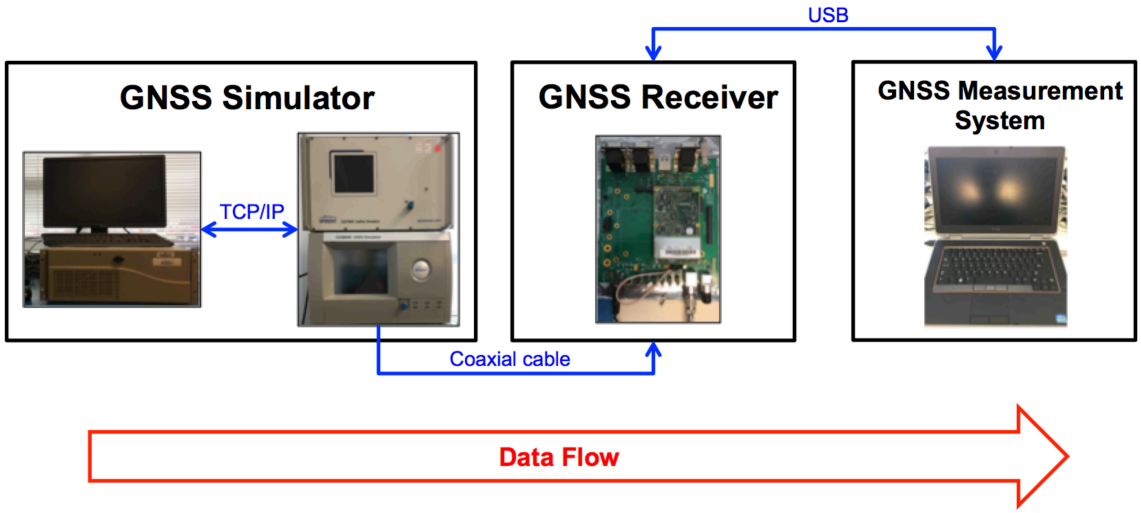

Figure 3.4. Open-loop configuration

While the closed-loop configuration will process the data from GNSS receiver and control the target spacecraft in the scenario during the simulation in real time. So the data flow is "round-trip" as shown below in Fig. 3.5.

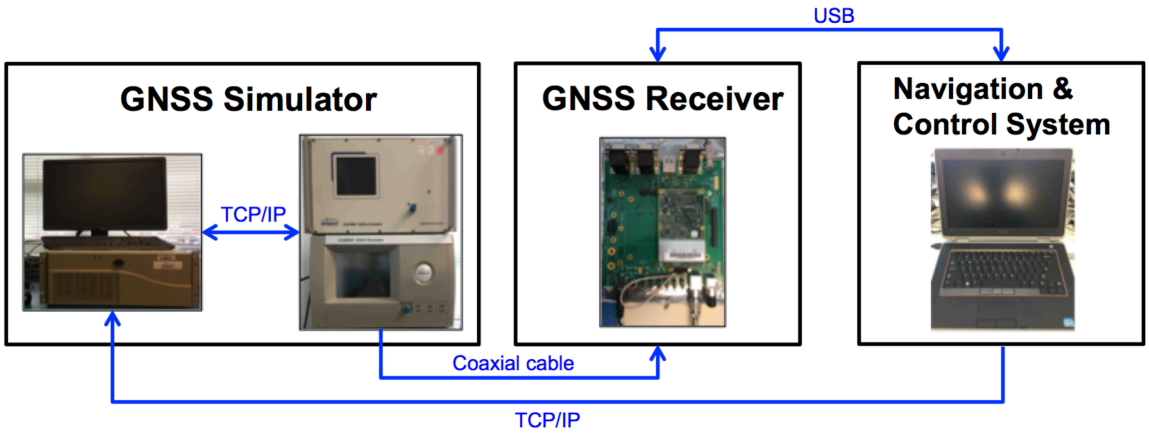

Figure 3.5. Closed-loop configuration

3.3.2. Reference Testbed Setup

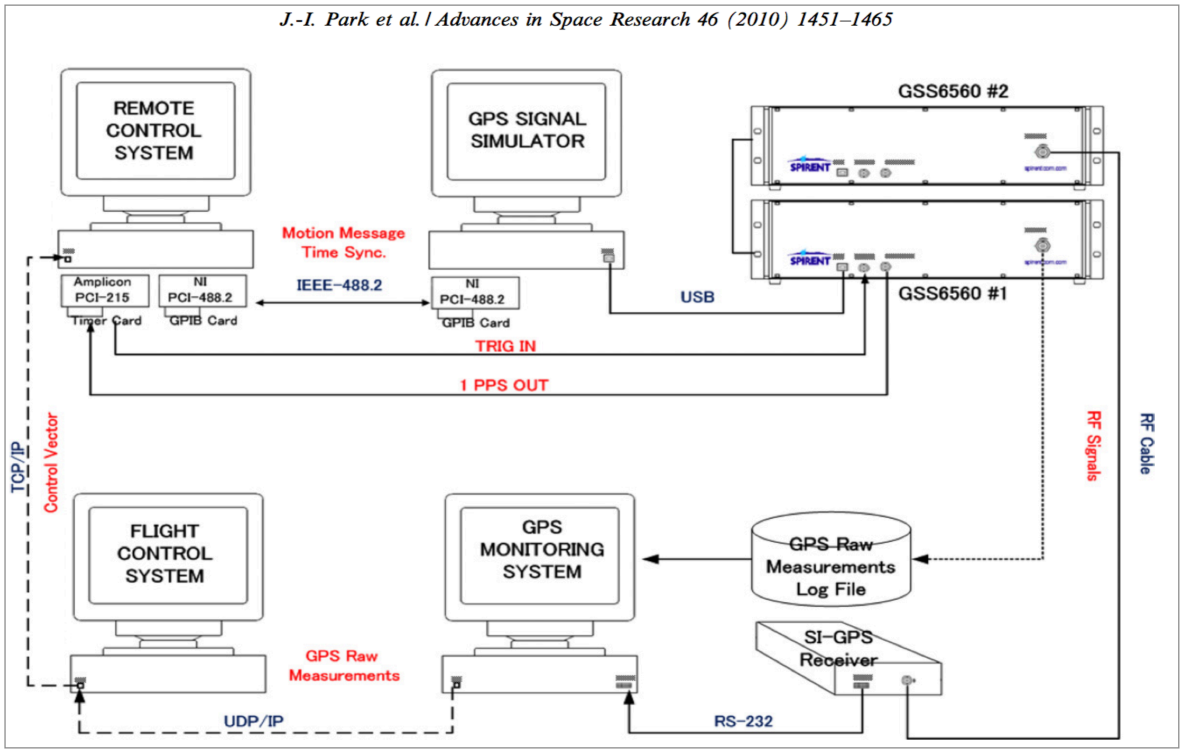

Figure 3.6. Closed-loop HIL simulation configuration of reference [5]

Fig 3.6 is the system configuration of reference [5]. "Spirent GPS simulators GSS6560", "SI-GPS receiver", "GPS monitoring system", "Flight control system", "Remote control system" and "Timer card" form their closed-loop simulation testbed. Note that, in their simulation the chief satellite is not under any maneuver but orbits the Earth without any thrust, while the deputy satellite is being controlled actively. Due to only one SI-GPS receiver available during their work, the observation file of the chief satellite was pre-recorded. During the closed-loop simulation, the GPS monitoring system continuously read the chief satellite's observation file along with the deputy satellite's real-time GPS data every 1 second. The Remote control system delivers motion commands to the GPS simulator every 100 ms. To make sure the deputy motion propagation arrives the GPS simulator a fraction of a second ahead of the time of execution consistently, a timer car was applied to synchronize the remote control system and the GPS simulator in millisecond accuracy.

3.3.3. Virginia Tech Formation Flying Testbed (VTFFTB)

Compared with the testbed in reference [5], the Virginia Tech Formation Flying Testbed (VTFFTB) consists of more advanced GPS simulators GSS8000 and Galileo simulator GSS7800, more sophisticated (Multi-frequency, Multi-constellation) GNSS receiver Novatel OEM628. The VTFFTB integrated "GNSS measurement system", "Flight control system" and "Remote control system" together into the software system on a Dell laptop as the "Navigation & Control system". Additionally, a STK Visualization System has been added into the VTFFTB for mission display.

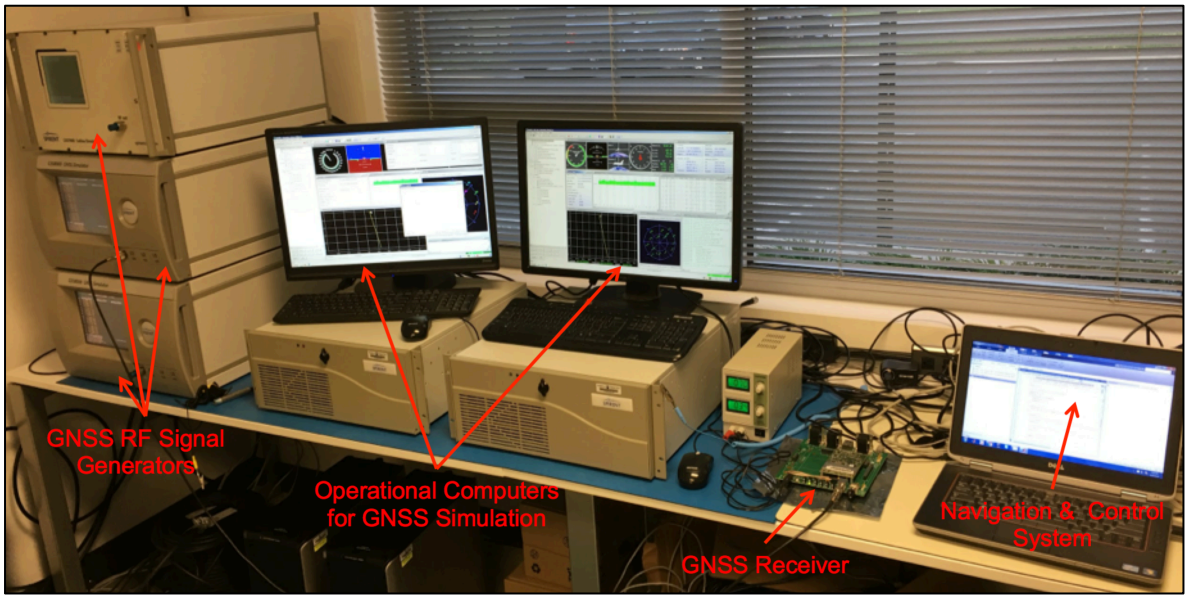

Figure 3.7. Virginia Tech Formation Flying Testbed

Because only one multi-constellation GNSS receiver is available for LEO spacecraft navigation in this study, the GNSS data for chief satellite of the scenario were recorded before the closed-loop real-time simulation, which is similar to the circumstance in reference [5]. The system configuration of the VTFFTB is shown below in Fig. 3.8:

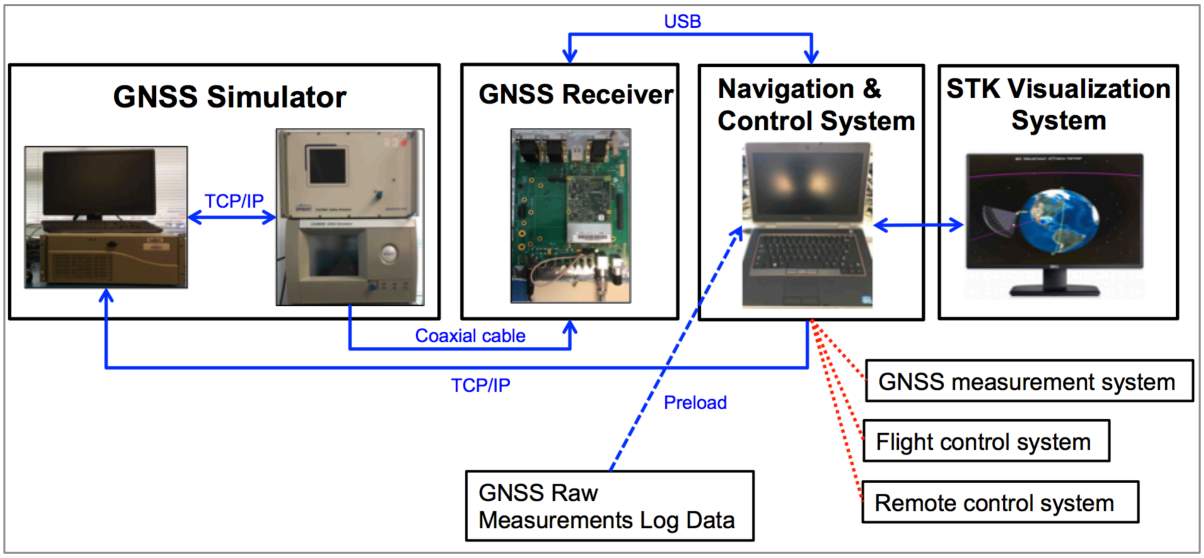

Figure 3.8. Closed-loop system configuration of the VTFFTB

The Spirent GNSS signal simulator can emulate all of the GPS signals received by the deputy spacecraft and output from the RF generator. The RF signals are received by the Novatel OEM628 receiver through the coaxial cable. The receiver produces raw GPS measurements for the deputy satellite including GPS time, pseudorange, carrier phase and ephemeris for all the tracked GPS satellites. The GNSS measurement system receives these data and processes them along with the dynamics propagator as well as the pre-recorded GPS raw measurement log data of the chief spacecraft, to estimate the absolute and relative states (positions and velocities) by running the EKF.

The estimation will be sent to the flight control system to calculate the required thrust to the maneuver the deputy spacecraft in real time. Next, the updated dynamics information will be transmitted to the remote control system and generate the motion command. Finally, the remote control system will deliver the deputy motion command through TCP/IP back to GNSS simulator and propagate the deputy spacecraft in SimGEN scenario for the upcoming time step, thereby closing the loop of the HIL spacecraft formation flying simulation.

It is worth mentioning that to avoid any potential receiver mistracking, the power level of the simulator RF output cannot be set too high. It was observed that when using an overly high simulated power, the Novatel OEM628 receiver was unable to track the simulated GNSS signals stably, and on occasion the receiver would restart on its own after the first navigation solution was computed. Also, properly resetting the receiver before every simulation was essential to avoiding potential GNSS timing issues.

3.3.3.1. STK Visualization Subsystem

Developed by Analytical Graphics, Inc. (AGI), Systems Tool Kit (STK) is an open source software package mainly used for aerospace mission simulation and modeling. STK offers a 4D (3D space + time) user-friendly environment to design, develop, and model space mission, including satellites, aircraft, radar, ground vehicle, ship and other facility or object. It's a convenient and valuable platform for spacecraft mission design and simulation.

One of the extensions beyond the reference [5] is adding the STK mission visualization system into the VTFFTB. MATLAB can be integrate with STK by using the STK's Object model and connect interfaces [33]. Motion information of both chief and deputy satellites from the dynamics propagator on MATLAB can be delivered to STK Integration module in real time. In this way, the orbits of chief and deputy spacecraft can be displayed on STK in real time, as shown in Fig. 3.9 and Fig. 3.10.

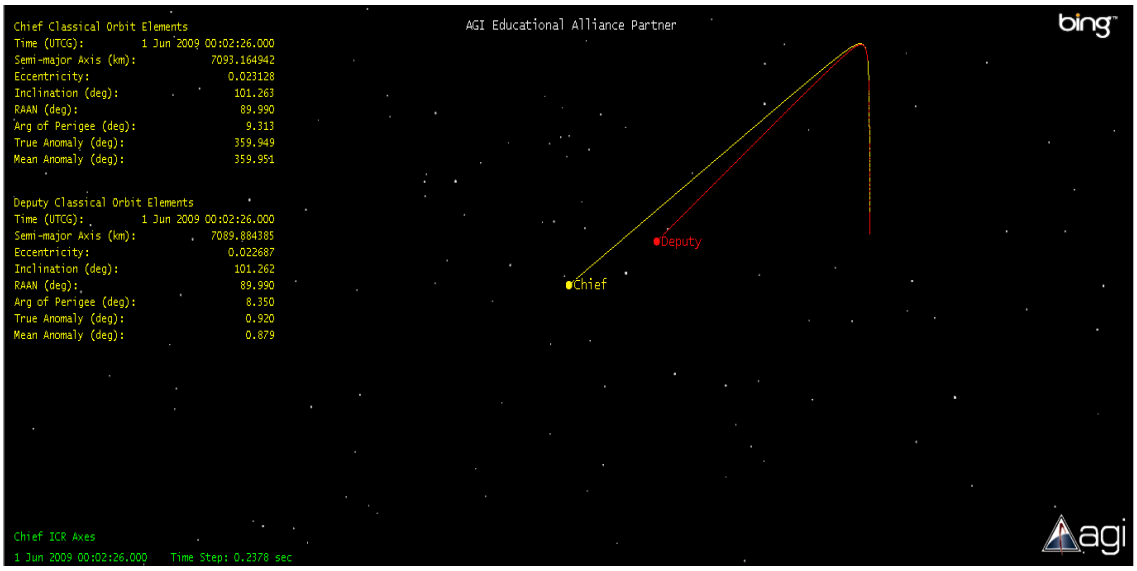

Figure 3.9. STK interface (example 1) for spacecraft formation flying

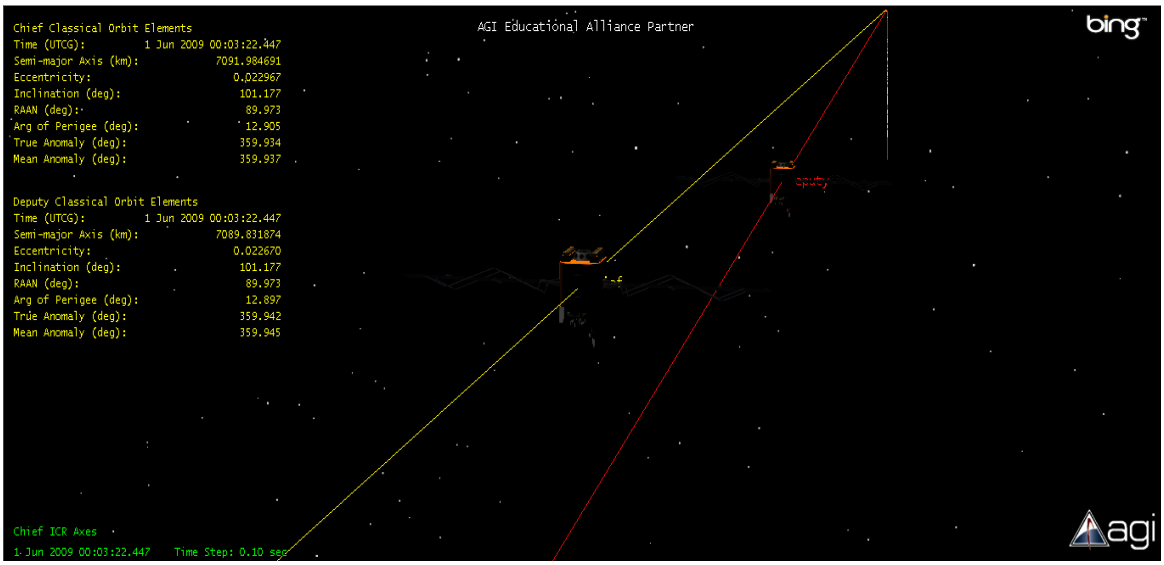

Figure 3.10. STK interface (example 2) for spacecraft formation flying

The connection between MATLAB and STK will slow down the run time of the Navigation & Control system and take up so much RAM. Particularly, without the implementation of timer card, it becomes more difficult to realize the time-synchronization between different hardware. Therefore, the real time STK visualization module was not applied into the final simulations in this work. But instead of real time display, STK was used as a mission replay system. After the simulations were completed, motion data of chief and deputy satellites were converted into ".e" file and insert into STK to reproduce the simulated spacecraft formation flying scenario.

Chapter 4

Software Algorithms and Design Methodology

4.1. Navigation & Control System Overview

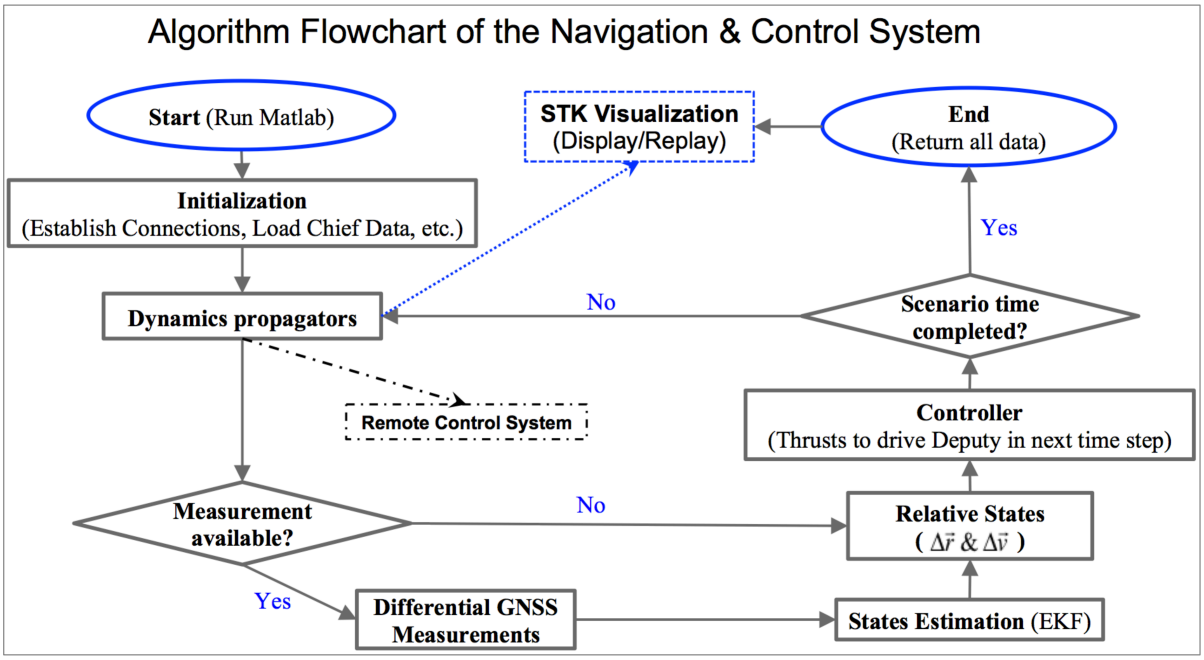

Figure 4.1. Algorithm flowchart of the navigation & control system

The algorithm flowchart for the navigation & control system of the VTFFTB is shown in Fig. 4.1. A step-by-step algorithms overview of the software system is given as follows:

1) **Start:** Run the main MATLAB program to start the scenario.

2) **Initialization:** Initialize all the variables or parameters, establish the connections with GNSS simulator and receiver, load the pseudorange and ephemeris data of the chief spacecraft and activate the deputy spacecraft scenario in SimGEN.

3) **Propagators for the first loop:** Start the motion propagations of chief and deputy spacecraft. (Details of the dynamics propagator will be discussed in section 4.3)

4) **Judge** if the GNSS measurement of deputy satellite are available at this moment. If yes, go to step (5); If not, the relative states (relative positions and relative velocities) are estimated directly by the result from dynamics propagators and jump to step (7).

5) **Differential GNSS measurements:** Perform single-differential pseudorange measurements (Details will be discussed in section 4.4)

6) **States Estimation:** Combine the dynamics predictions, measurement predictions and real-time measurements to execute Extend Kalman Filter, and output the estimations of relative states;

7) **Controller:** The estimated relative states will be passed to the controller along with the chief states (positions and velocities). The controller will calculate the thrusts needed to drive the deputy spacecraft at current time step.

8) Reach the end of the loop and **judge** if the scenario time (set to 1 hour as default) is ended. If yes, terminate the simulation and output and save all the data; If not, go back to step (3) and continue the looping.

9) **Propagators after the 1st loop:** Now, we can predict the deputy (position, velocity) states in next time step by using the updated acceleration (considering the thrust) and the newly estimated relative states. And we can generate and deliver the deputy motion command in next time step to SimGEN via TCP/IP. After that, pause the looping for the length of designed time interval and then go to step (4).

The run time of the navigation & control system has to be faster than the logging rate of 1 Hz due to timing and synchronization issues. There are time delays from receiving GNSS measurements, solving thrusts in the controller, sending commands back to the simulator and so on. Experiments showed that the solution of the controller in MATLAB has been on the order of 0.01 seconds, the run time of each loop of the navigation & control system with current configurations range from 0.06 to 0.07 seconds. So we are confident that the software system run time is fast enough to achieve the formation flying navigation and control. However, the run time of each loop is not constant. So without the implement of time synchronization system, some issues will arise and will be discussed in chapter 5. The algorithms and design methodology of each subsystem are presented from Section 4.2 through Section 4.6.

4.2. Communication with hardware

The duty of the remote control system is to generate the motion commands in the right syntax and send them to the GNSS simulator/SimGEN via TCP/IP socket. This process is called SimGEN Remote Control. There are two main formats of the motion commands for remote control: “MOT” and “MOTB”. “MOT” is the format with respect to ECEF coordinate frame while “MOTB” is the format with respect to WGS-84 coordinate frame. More details can refer to the SimREMOTE User Manual [34]. The “MOT” format is chosen to deliver the motion commands, which contains time, positions, velocities and accelerations (in ECEF frame). The remote control system will continuously drive the deputy spacecraft in the remote scenario.

GNSS measurement system can request and read the data from the OEM628 receiver by USB communication in real time. The connectivity is realized by establishing a serial port object in MATLAB. A logging rate of 1 Hz is adopted to query the time, pseudorange and the standard derivation of pseudorange for all visible GNSS satellites.

4.3. Dynamics Propagator

The dynamics model for satellite motion propagation adopted by reference [5] is expressed as follow:

$$\ddot{\vec{r}} = \frac{\mu}{r^3}\vec{r} + \vec{a}_{\text{geo}} + \vec{a}_{\text{darg}} + \vec{a}_{\text{asp}} + \vec{a}_{\text{thrust}} \tag{29}$$

where:

$\vec{a}_{\text{geo}}$ = graviational acceleration due to the Earth's non-spherical gravitational potential

$\vec{a}_{\text{darg}}$ = atmospheric drag acceleration

$\vec{a}_{\text{asp}}$ = acceleration by solar radiation pressure

$\vec{a}_{\text{thrust}}$ = thrust acceleration due to the maneuvers

Reference [5] also made the following assumptions: The drag coefficient C_D is 2.3, the cross-section area for drag computation is 1 m^2, and the solar radiation pressure coefficient C_R is 1.3. A 1 Hz pulsed plasma thruster (PPT) system with impulse-bit of 0.112mN is used for the 20 Kg deputy spacecraft maneuvers. For the chief spacecraft the thrust acceleration term can be ignored because no maneuver is applied on the chief satellite as we mentioned earlier in section 3.3.2. The selected force model for the Earth's gravitational field is a 20×20 subset of the joint gravity model 3 (JGM-3) [3], which is modeled by a 20th order spherical harmonics function.

The Earth's gravity potential ***U*** can be expressed in the form of Legendre polynomials:

$$U = \frac{\mu}{r}\sum_{n=0}^{\infty}\sum_{m=0}^{n}\frac{R_e^n}{r^n}P_{nm}(\sin\phi)\left[C_{nm}\cos(m\lambda) + S_{nm}\sin(m\lambda)\right] \tag{30}$$

where R_e is the equatorial radius of the Earth, ϕ and λ are the geocentric latitude and longitude respectively, C_{nm} and S_{nm} are JGM-3 gravitational coefficients and the associated Legendre polynomial of degree n and order m is defined as:

$$P_{nm}(u) = \left(1-u^2\right)^{m/2}\frac{d^m}{du^m}P_n(u) \tag{31}$$

$$P_n(u) = \frac{1}{2^n n!}\frac{d^n}{du^n}\left(u^2-1\right)^n \tag{32}$$

The numerical propagation method referred by reference [5] is Runge Kutta 4th order (RK4) method. An example of the RK4 position and velocity "one-step-forward" propagation is presented as follow:

$$k_1 = \begin{bmatrix} \vec{v}_0 \\ \vec{a}(\vec{r}_0) \end{bmatrix} \tag{33}$$

$$k_2 = \begin{bmatrix} \vec{v}_0 + \frac{1}{2}\vec{a}(\vec{r}_0) \\ \vec{a}(\vec{r}_a) \end{bmatrix} \quad \text{where} \quad \vec{r}_a = \vec{r}_0 + \vec{v}_0 dt + \frac{1}{2}\vec{a}(\vec{r}_0)(dt)^2 \tag{34}$$

$$k_3 = \begin{bmatrix} \vec{v}_0 + \frac{1}{2}\vec{a}(\vec{r}_a) \\ \vec{a}(\vec{r}_b) \end{bmatrix} \quad \text{where} \quad \vec{r}_b = \vec{r}_0 + \vec{v}_0 dt + \frac{1}{2}\vec{a}(\vec{r}_a)(dt)^2 \tag{35}$$

$$k_4 = \begin{bmatrix} \vec{v}_0 + \vec{a}(\vec{r}_b) \\ \vec{a}(\vec{r}_c) \end{bmatrix} \quad \text{where} \quad \vec{r}_c = \vec{r}_0 + \vec{v}_0 dt + \frac{1}{2}\vec{a}(\vec{r}_b)(dt)^2 \tag{36}$$

Finally the position and velocity vector in the next time step are given by:

$$\begin{bmatrix} \vec{r}_1 \\ \vec{v}_1 \end{bmatrix} = \begin{bmatrix} \vec{r}_0 \\ \vec{v}_0 \end{bmatrix} + \left(\frac{k_1 + 2k_2 + 2k_3 + k_4}{6} \right) dt \tag{37}$$

When the RK4 method was implemented to propagate the satellite orbit, the SimGEN would report kinetic errors of the propagation. It turned out that the motion propagation principle in Spirent simulator is non-linear interpolation [35], instead of Runge Kutta methods. An example of the interpolated non-linear position and velocity "one-step-forward" propagation is presented as follow:

$$\begin{bmatrix} \vec{r}_1 \\ \vec{v}_1 \end{bmatrix} = \begin{bmatrix} \vec{r}_0 + \vec{v}_0 \cdot dt + \frac{1}{2} \cdot \vec{a}(\vec{r}_0) \cdot (dt)^2 + \frac{1}{6} \cdot j_0 \cdot (dt)^3 \\ \vec{v}_0 + \vec{a}(\vec{r}_0) \cdot dt + \frac{1}{2} \cdot j_0 \cdot (dt)^2 \end{bmatrix} \tag{38}$$

Where the jerk (j) is always assumed as 0 $(j_1 = 0)$

Experiments verified this propagation method could work in the GNSS simulator and SimGEN without any issue. Therefore such propagation method is adopted in the final version of dynamics propagator. The time interval of propagation is 100ms, which is consistent with the simulation iteration rate of 100ms.

The dynamics model used in VTFFTB for satellite orbit propagation can be expressed as:

$$\ddot{\vec{r}} = \frac{\mu}{r^3}\vec{r} + \vec{a}_{\text{geo}} + \vec{a}_{\text{darg}} + \vec{a}_{\text{thrust}} \tag{39}$$

This is similar to the model adopted by reference [5], i.e. Eq. (29) except two differences:

① A 8×8 subset instead of the 20×20 subset of the JGM-3 gravitational field model is used;
② Solar radiation pressure was not included in the orbital perturbations.

Note that, 20×20 JGM-3 subset of JGM-3 model can be used. But the 8×8 JGM-3 gravitational model (lower accuracy but faster run time compared to 20×20 JGM-3) is implemented in the dynamics propagator at this point to improve computational efficiency and avoid further time-synchronization issue. The Kepler (two-body) gravitational model was firstly used to develop the initial dynamics propagator. Testing revealed that, the run time of 8×8 JGM-3 model propagator is about 0.02 second every time step. While the run time of Kepler model propagator is only about 0.002 second every time step, which is 10 times faster. The simulation results of Kepler model will also be presented in Section 5.2.1 for comparison. Furthermore, testing results show that the atmospheric drag perturbation is much less than the perturbation caused by the Earth's non-spherical gravitational field.

Coordinate transformations are iteratively performed during the dynamics propagation. The 3D trajectory of the 8×8 JGM-3 orbit 12-hour propagation in ECI frame are compared with the same orbit in ECEF frame as shown below in Fig. 4.2:

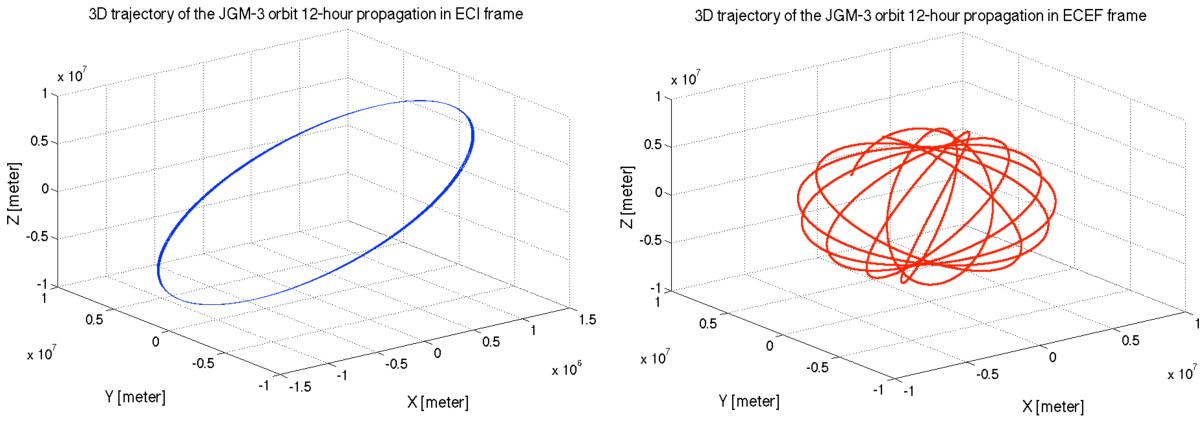

Figure 4.2. 12-hour JGM-3 orbit propagation (Left: ECI frame; Right: ECEI frame)

4.4. Differential GPS Measurement

Reference [5] used both the single-differential pseudorange measurement model and the double-differential carrier-phase measurement model to precisely determine the relative motion between the chief and deputy satellite [36]. For small baseline formation flying, some GNSS ranging errors such as ionospheric delays, troposphere delays, satellite clock bias, receiver clock bias, receiver noise etc., could be canceled out by taking the single and double differences. Therefore, when the separation between satellites in formation is relatively small, differential GNSS measurement technique is a powerful tool for precise relative navigation.

Single-differential pseudorange measurement is used in the GNSS measurement system. The model is outlined and explained as below:

Recall Eq. (1), the GNSS observable pseudorange of the GPS satellite *m* with respect to vehicle *i* can be expressed as:

$$P^m = R + c\left(\Delta T + \Delta t\right) + \Delta_{ionosphere} + \Delta_{troposphere} + \Delta_{multipath} + \Delta_{DOP} + \Delta_{receiver} + \Delta_{other} \tag{40}$$

Combine the delays of multipath, DOP, receiver and other noise together as one noise term, then:

$$P_i^m = \left\|\vec{r}^{\,m} - \vec{r}_i\right\| + c\left(\Delta T^m + \Delta t_i\right) + \Delta_{ionosphere}^m + \Delta_{troposphere}^m + \Delta_{noise,i}^m \tag{41}$$

$$P_j^m = \left\|\vec{r}^{\,m} - \vec{r}_j\right\| + c\left(\Delta T^m + \Delta t_j\right) + \Delta_{ionosphere}^m + \Delta_{troposphere}^m + \Delta_{noise,j}^m \tag{42}$$

(where *m* stands for GPS satellite m, *i* stands for chief spacecraft and *j* stands for deputy spacecraft)

Next, take the single difference with respect to GPS satellite m between chief *i* and deputy *j*, the single differential pseudorange for GPS satellite *m* is:

$$\Delta P_{ij}^m = P_i^m - P_j^m = \left\|\vec{r}^{\,m} - \vec{r}_i\right\| - \left\|\vec{r}^{\,m} - \vec{r}_j\right\| + c\left(\Delta t_i - \Delta t_j\right) + \left(\Delta_{noise,i}^m - \Delta_{noise,j}^m\right) \tag{43}$$

Replace the deputy satellite positions by the position of chief plus the relative position as $\vec{r}_i + \vec{\rho}_{ij}$,

write the differential receiver code bias as δt and the differential noise term as δ_{noise}^m, then:

$$\Delta P_{ij}^m = P_i^m - P_j^m = \left\|\vec{r}^{\,m} - \vec{r}_i\right\| - \left\|\vec{r}^{\,m} - \left(\vec{r}_i + \vec{\rho}_{ij}\right)\right\| + c\delta t + \delta_{noise}^m \tag{44}$$

If there are *n* visible satellites at the time of measurement, then the measurement model matrix can be written as:

$$\begin{bmatrix} \Delta P_{ij}^1 \\ \Delta P_{ij}^2 \\ \cdots \\ \Delta P_{ij}^n \end{bmatrix} = \begin{bmatrix} \left\|\vec{r}^{\,1} - \vec{r}_i\right\| - \left\|\vec{r}^{\,1} - \left(\vec{r}_i + \vec{\rho}_{ij}\right)\right\| + c\delta t + \delta_{noise}^1 \\ \left\|\vec{r}^{\,2} - \vec{r}_i\right\| - \left\|\vec{r}^{\,2} - \left(\vec{r}_i + \vec{\rho}_{ij}\right)\right\| + c\delta t + \delta_{noise}^2 \\ \cdots \\ \left\|\vec{r}^{\,n} - \vec{r}_i\right\| - \left\|\vec{r}^{\,n} - \left(\vec{r}_i + \vec{\rho}_{ij}\right)\right\| + c\delta t + \delta_{noise}^n \end{bmatrix} \tag{45}$$

On the right hand side of Eq. (45), positions of all the visible GPS satellites $\vec{r}^{\,m}$ are calculated by using the GPS ephemeris (in the navigation file). The chief position is determined from the absolute navigation using the preload GPS raw data of the chief spacecraft. The relative position $\vec{\rho}_{ij}$ and differential receiver code bias $c\delta t$ are included in the states matrix to be estimated, which will be

clearly defined in the next section. The differential noise term δ^{m}_{noise} is modeled as the Gaussian white noise.

4.5. Extended Kalman Filter

Extended Kalman Filter (EFK) is used for relative states estimation in the navigation & control system of the HIL testbed. The measurement results from section 4.4 will be inputted into the EFK together with the dynamics propagation results from section 4.3.

The 8×1 matrix of states to be estimated can be defined as:

$$X = \begin{bmatrix} \vec{\rho}_{ij} \\ \delta t \\ \dot{\vec{\rho}}_{ij} \\ \dot{\delta} t \end{bmatrix} = \begin{bmatrix} \text{relative position vector} \\ \text{differential receiver code bias (clock offset)} \\ \text{relative velocity vector} \\ \text{time-differential receiver code bias (clock drift)} \end{bmatrix} \tag{46}$$

The fundamental procedure of EFK is outlined step-by-step as follows. And these will be applied to the dynamics propagator and differential GPS measurement model discussed in the previous sections.

Step 1 – Initialization

Initialize the following parameters: states to be estimated $X(t_0)$, state covariance $P(t_0)$, process noise covariance Q and measurement noise covariance $R(t_0)$.

Step 2 – Relative states prediction

Propagate the relative states based on the dynamics propagator *f*:

$$X^{P}(t_1) = f\left[t_0, X(t_0), thrust(t_0)\right] \tag{47}$$

Step 3 – Evaluate State Prediction Jacobians

$$F(t_0) = \left.\frac{df(t_0)}{dX}\right|_{X=X(t_0)} \tag{48}$$

Step 4 – Determine the State Prediction Covariance

$$P^{P}(t_1) = F(t_0)P(t_0)F(t_0)^{T} + Q \tag{49}$$

Note that, the process noise covariance Q is assumed as constant.

Step 5 – Measurement of differential pseudoranges

$$Z(t_1)=\begin{bmatrix} \Delta P_{ij}^1 \\ \Delta P_{ij}^2 \\ \cdots \\ \Delta P_{ij}^n \end{bmatrix} \tag{50}$$

Meanwhile, the number of visible and available GPS satellites can be determined at this moment.

Step 6 – Measurement Prediction

Recall Eq. (45), the measurements of differential pseudorange can be predicted as:

$$\hat{Z}=h\left[t_1,X^P(t_1)\right]=\begin{bmatrix} \left\|\vec{r}^{\,1}-\vec{r}_i\right\|-\left\|\vec{r}^{\,1}-\left(\vec{r}_i+\vec{\rho}_{ij}\right)\right\|+c\delta t+\delta_{noise}^1 \\ \left\|\vec{r}^{\,2}-\vec{r}_i\right\|-\left\|\vec{r}^{\,2}-\left(\vec{r}_i+\vec{\rho}_{ij}\right)\right\|+c\delta t+\delta_{noise}^2 \\ \cdots \\ \left\|\vec{r}^{\,n}-\vec{r}_i\right\|-\left\|\vec{r}^{\,n}-\left(\vec{r}_i+\vec{\rho}_{ij}\right)\right\|+c\delta t+\delta_{noise}^n \end{bmatrix} \tag{51}$$

Step 7 – Evaluate Measurement Prediction Jacobians

$$H(t_1)=\left.\frac{dh(t_1)}{dX}\right|_{X=X^P(t_1)} \tag{52}$$

Step 8 – Determine the Residual Covariance

$$S(t_1)=R(t_1)+H(t_1)P^P(t_1)H(t_1)^T \tag{53}$$

Note that, the updated measurement noise covariance $R(t_1)$ is obtained from the GPS raw measurements. Standard derivations of pseudorange from the 1-Hz "ontime" log message were used to construct the diagonal matrix R.

Step 9 – Calculate the Residual of Measurement

$$\Delta Z(t_1)=Z(t_1)-\hat{Z}(t_1) \tag{54}$$

Step 10 – Determine the Kalman Filter Gain

$$K(t_1) = \frac{P^P(t_1)\left[H(t_1)\right]^T}{S(t_1)} \tag{55}$$

Step 11 – Update State Estimation

$$X(t_1) = X^P(t_1) + K(t_1)\Delta Z(t_1) \tag{56}$$

Step 12 – Update State Covariance

$$P(t_1) = P^P(t_1) - K(t_1)S(t_1)K(t_1)^T \tag{57}$$

After step (12), go back to step (2) to continue the looping, thereby closing the filtering process.

4.6. SDRE (State-Dependent Riccati Equation) Controller

In order to achieve the desired relative motion of the formation flying, a controller is designed to guide the deputy spacecraft to the intended relative states with respect to the chief spacecraft using only thrusts of three unit vector directions (radial, in-track or cross-track). In an attempt to solve the required thrusts for the maneuvers, a State Dependent Riccati Equation (SDRE) technique was used for the relative orbit control. The SDRE technique solved equations can be expressed in the state-space representation form：

$$\dot{\vec{x}} = A(\vec{x})\vec{x} + B(\vec{x})\vec{u} \tag{58}$$

Where **A** corresponds to the Hill's equations of relative motion, i.e. Eq. (25), Eq. (26) and Eq. (23), **B** corresponds to a control matrix (changes in velocity), **x** is the deputy state vectors relative to the chief satellite in the body frame, and **u** is the thrusts in the body frame to be solved.

Rewrite the Hill's equation in the form with all perturbation including thrust:

$$\begin{bmatrix} \ddot{x} - 2\dot{v}\dot{y} - \ddot{v}y - \dot{v}^2 x - \dfrac{\mu}{r_c^2} + \dfrac{\mu(r_c + x)}{\gamma} \\ \ddot{y} + 2\dot{v}\dot{x} + \ddot{v}x - \dot{v}^2 y + \dfrac{\mu y}{\gamma} \\ \ddot{z} + \dfrac{\mu z}{\gamma} \end{bmatrix} = \begin{bmatrix} a_x \\ a_y \\ a_z \end{bmatrix} \tag{59}$$

(Where a_x, a_y, and a_z are orbital perturbation terms, which include non-spherical geopotential perturbation, air drag, and thrust)

After rewriting the Hill's equation into the SDRE form, Eq. (58) can be expressed as follows [5]:

$$\begin{pmatrix} \dot{x}_1 \\ \dot{x}_2 \\ \dot{x}_3 \\ \dot{x}_4 \\ \dot{x}_5 \\ \dot{x}_6 \end{pmatrix} = \begin{bmatrix} 0 & 1 & 0 & 0 & 0 & 0 \\ \dot{v}^2 - \frac{\mu}{\gamma} + \frac{3\mu}{2r_c^3}\left(2 + \frac{x}{r_c}\right)\Psi & 0 & \ddot{v} + \frac{3\mu}{2r_c^4} y\Psi & 2\dot{v} & \frac{3\mu}{2r_c^4} z\Psi & 0 \\ 0 & 0 & 0 & 1 & 0 & 0 \\ -\ddot{v} & -2\dot{v} & \dot{v}^2 - \frac{\mu}{\gamma} & 0 & 0 & 0 \\ 0 & 0 & 0 & 0 & 0 & 1 \\ 0 & 0 & 0 & 0 & -\frac{\mu}{\gamma} & 0 \end{bmatrix} \times \begin{pmatrix} x_1 \\ x_2 \\ x_3 \\ x_4 \\ x_5 \\ x_6 \end{pmatrix} + \begin{bmatrix} 0 & 0 & 0 \\ 1 & 0 & 0 \\ 0 & 0 & 0 \\ 0 & 1 & 0 \\ 0 & 0 & 0 \\ 0 & 0 & 1 \end{bmatrix} \begin{pmatrix} u_1 \\ u_2 \\ u_3 \end{pmatrix} \quad \textbf{(60)}$$

Where:

x_1, x_2 and x_3 are relative position components of x, y and z

x_4, x_5 and x_6 are relative velocity components of $\dot{x}$, $\dot{y}$ and $\dot{z}$

$$\Psi = \sum_{i=1}^{\infty} \frac{1.5 + i}{i + 1} \zeta \Psi_{i-1}, \quad \Psi_0 = 1$$

$$\zeta = -\frac{2}{r_c} x - \frac{x^2 + y^2 + z^2}{r_c^2}$$

$\dot{v}$ and $\ddot{v}$ are the first and second time derivative of the true anomaly of the Chief, which can be derived from Eq. (28).

Here, solving Eq. (60) can be cast as an optimization problem with the performance index J as:

Weighted control matrices

$$J = \int_0^{\infty} ((\vec{x} - \vec{x}_d)^T Q_{ctr} (\vec{x} - \vec{x}_d) + \vec{u}^T R_{ctr} \vec{u}) dt \quad \textbf{(61)}$$

Current Deputy state vector — Desired Deputy state vector — Applied thrust to solve for

The weighted control matrices are written as the identity matrix multiplied by some constant. In this case, Q is multiplied by 1 and R is multiplied by 1000. This is where the tradeoff between the energy required to control the formation flying and the errors associated with the current formation flying configuration comes in.

Using SDRE control law, the solution for the optimization problem above can be solved by finding G in the following expression:

$$\vec{u} = -R_{ctr}^{-1} B^T G(\vec{x})(\vec{x} - \vec{x}_d) \tag{62}$$

Here, G is the positive-definite solution of the following Riccati equation:

$$G(\vec{x})A(\vec{x}) + A(\vec{x})^T G(\vec{x}) - G(\vec{x})BR_{ctr}(\vec{x})^{-1} B^T G(\vec{x}) + Q_{ctr} = 0 \tag{63}$$

This solution can be found by using the "care" function in MATLAB. And it is important to note that the construction of this solution does not account for perturbations, but instead assumes those have been applied to the Deputy state vector before being handed over to the controller. Also, the thrust limit of this controller in each unit vector direction can be customized. Note that, the default thrust cap is set as 1 m/s^2 (in each unit direction).

To summarize the principle of operation of the SDRE controller: The MATLAB function starts with coordinate transformation to convert the relative state vector from ECI frame to body frame, and then inputs those state variables into the Eq. (60). Next, Eq. (63) is solved for the linear quadratic regulators (LQR) to get the minimum cost (performance index J). Lastly, the thrusts that need to be applied for the maneuver can be determined.

Chapter 5

Testing and Validation

5.1. HIL Reference Scenario and Simulation Results

A similar scenario of formation flying with respect to reference [5] simulation has been established. The objective is to run both the software and hardware simulation with the same set of initial dynamics conditions as reference [5] for benchmarking as well as validation.

The reference scenario is comprised of two LEO satellites with an initial in-track separation of 1000 m and an altitude of around 550 km. It's designed to perform the formation acquisition to maneuver the deputy spacecraft to achieve 100 m in-track distance and maintain such formation flying till the end of the simulation. Total run time of the scenario is 1 hour. A cap on the total thrust that is allowed to be applied on the deputy spacecraft in every second is limited to 1 m/s for each unit vector direction. This is done in an attempt to replicate an actual satellite, which would have limitations based on its own capabilities. Besides the thrusts, detail of the other orbital perturbations has been introduced in Section 4.3. The initial classical orbital elements and ECEF states are listed in Table 2:

Orbital Elements	**Chief spacecraft**	**Deputy spacecraft**
Semi-major axis (a) (m)	6937466	6937466
Eccentricity (e)	0.00120	0.00120
Inclination (i) (°)	97.615	97.615
Argument of perigee (ω) (°)	359.951	359.951
Longitude of ascending node (Ω) (°)	339.484	339.484
Mean anomaly (M) (°)	0.0000450	0.0084424
ECEF Values		
x (m)	-77.9763	54.5423
y (m)	6929124.9712	6929124.8729
z (m)	193.6730	1184.8535
v_x (m/s)	1510.9785	1510.9785
v_y (m/s)	-0.1932	-1.2968
v_z (m/s)	7522.1738	7522.1737
a_x (m/s^2)	-0.0001	-0.0004
a_y (m/s^2)	-8.4966	-8.4966
a_z (m/s^2)	-0.0002	-0.0014

Table 2. Initial orbital elements and ECEF state vectors of the reference scenario [5]

The corresponding initial relative position and velocity are calculated by coordinate transformation and list them in Table 3. And the desired relative states are listed in Table 4.

Radial separation (m)	-0.0708	Radial relative velocity (m/s)	0.0013
In-track separation (m)	997.8673	In-track relative velocity (m/s)	2.2493×10^{-5}
Cross-track separation (m)	-65.2758	Cross-track relative velocity (m/s)	8.2274×10^{-5}

Table 3. Initial relative states in body frame of the reference scenario

Radial separation (m)	0	Radial relative velocity (m/s)	0
In-track separation (m)	100	In-track relative velocity (m/s)	0
Cross-track separation (m)	0	Cross-track relative velocity (m/s)	0

Table 4. Desired relative states in body frame of the reference scenario

The closed-loop HIL simulation results of reference [5] are shown and explained below, which will be use to benchmark the simulation results of VTFFTB presented in Section 5.2 and 5.3.

1) The absolute navigation errors of positioning for deputy satellite are shown in Fig. 5.1, where the mean and standard deviation values for each direction are summarized in the table on the right.

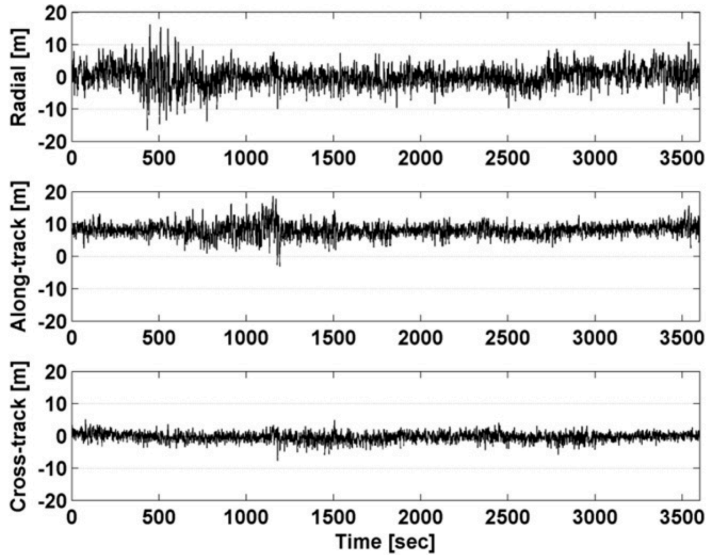

Direction	Position (m)	
	Mean	Std
Radial	−0.066	3.282
Along-track	7.978	2.018
Cross-track	−0.374	1.347

Figure 5.1. Closed-loop absolute navigation position error for deputy satellite [5]

2) The relative navigation errors for deputy satellite are shown in Fig. 5.2. The mean and standard deviation values for each direction are summarized in the Table 5.

Direction	Position (m)		Velocity (m/s)	
	Mean	Std	Mean	Std
Radial	0.003	0.026	0.0000	0.0021
Along-track	0.000	0.053	0.0001	0.0041
Cross-track	0.000	0.028	0.0000	0.0019

Table 5. Characteristics of relative navigation errors [5]

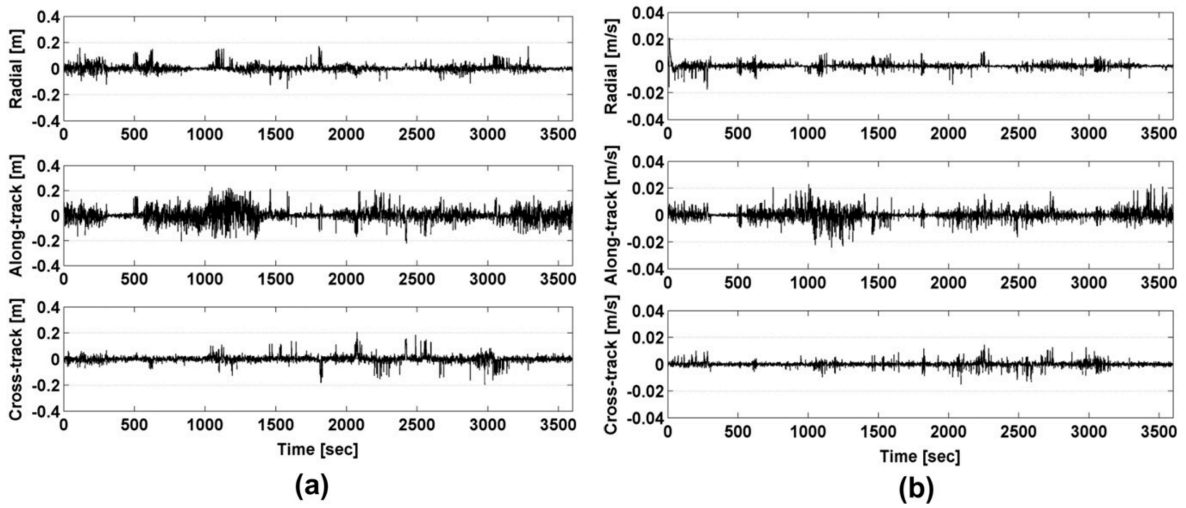

Figure 5.2. Closed-loop relative navigation errors: (a) position errors; (b) velocity errors [5]

3) The relative position in each direction for formation acquisition and keeping phase are shown in the left side of Fig. 5.3. Through the formation acquisition process from the beginning to about 141 s, the targeted 100-m in-track separation of the formation flying is successfully achieved, and the formation keeping process starts from approximately 142 s. Take another look of the relative motion trajectory of the deputy satellite in the chief-centered rotating frame as shown in the right side of Fig. 5.3. The initial in-track separation is decreased to the desired 100-m separation.

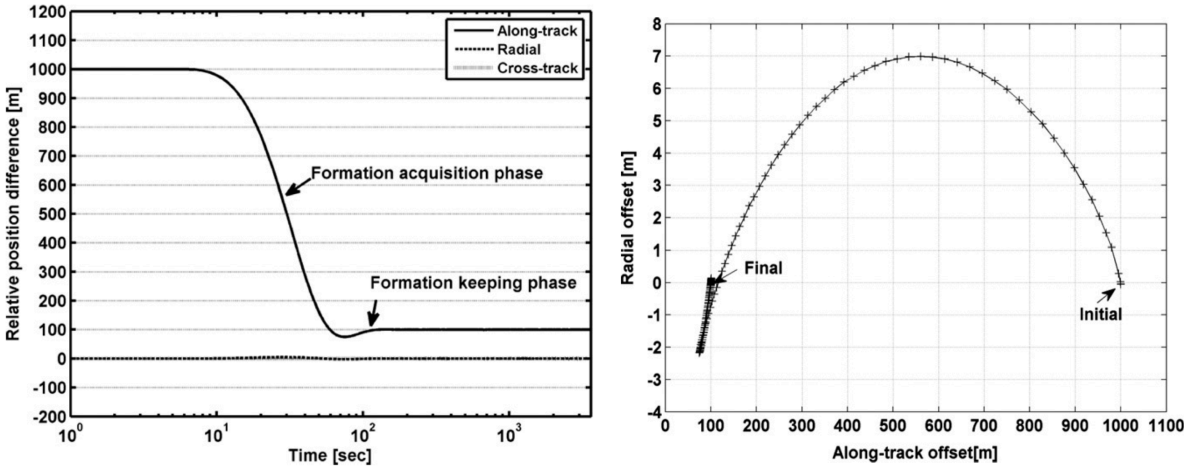

Figure 5.3. Result of relative motion during the closed-loop HIL simulation (Left: positions v.s. time; Right: relative motion trajectory in the chief-centered rotating frame) [5]

4) The performance of the navigation & control system for formation keeping can be characterized by the maximum, mean, and standard deviations of the relative state, as summarized in table in the right side of Fig. 5.4. And the distance between the deputy and chief satellites during the formation keeping is plotted in the left side of Fig. 5.4. The results indicate the desired 100-m in-track formation flying separation of reference [5] can be maintained with a mean position error of approximately 0.2 m and a standard deviation of 0.9 m.

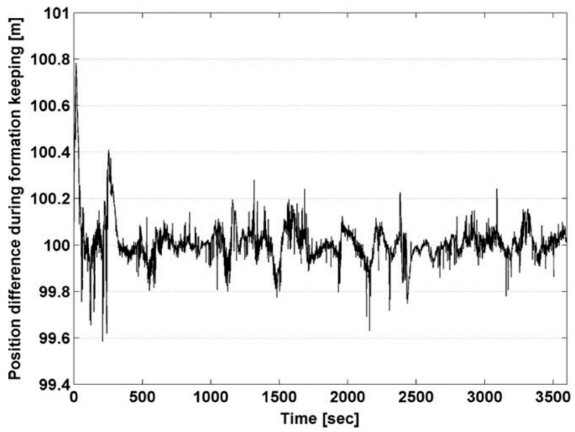

	Radial (m)	Along-track (m)	Cross-track (m)
Minimum	−1.617	99.58	−0.496
Maximum	1.132	100.81	0.394
Mean	0	100.19	0
RMS	0.172	0.091	0.070

Figure 5.4. Left: Position difference between the Chief and Deputy during the formation keeping; Right: Characteristics of autonomous formation-keeping control [5]

5) The control accelerations (applied thrusts) in each axis during the HIL simulation are shown in Fig. 5.6. A total ΔV of 69.56 m/s has been applied to the in-track direction for the entire simulation. Specifically, a ΔV of 64.75 m/s is used for the formation acquisition while a ΔV of 4.8 m/s is used for the formation keeping. Since the control is primarily commanded in the along-track direction, the in-track ΔV is larger than in the fuel cost in other directions. The thrusts used in the one-hour simulation here are likely to be overly high for CubeSats with the current propulsion system. However, it should be noted again, the objective here is to reproduce the reference simulation results rather than design a realistic scenario.

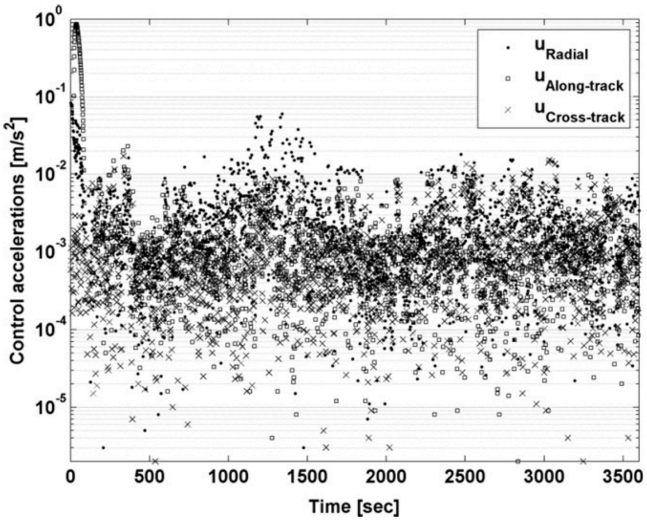

Figure 5.5. Control accelerations in each axis during the formation acquisition and keeping [5]

5.2. Software Simulation

To test the flight control system, pure software simulations were firstly performed on MATLAB. The motions of the chief and deputy spacecraft are purely driven by the dynamics propagator and the flight controller. In this case, the GNSS measurement system was deactivated so no EKF was applied. Both the Kepler and 8×8 JGM-3 gravity models were tested and compared.

5.2.1. Simulation Results and Comparisons

The simulation results using Kepler gravity model are presented on the left, while the simulation results using JGM-3 gravity model are presented on the right.

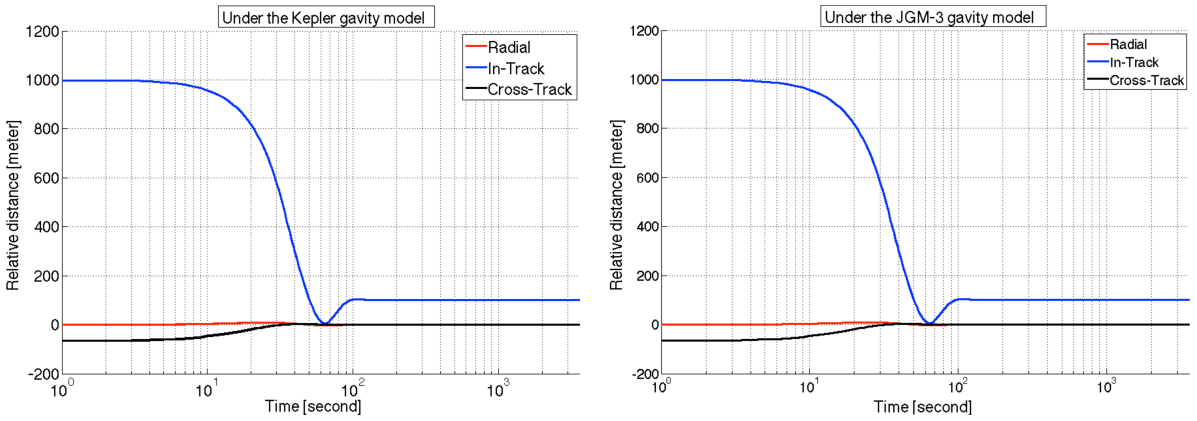

Figure 5.6. Software simulation of relative positions v.s. time (Left: Kepler ; Right: JGM-3)

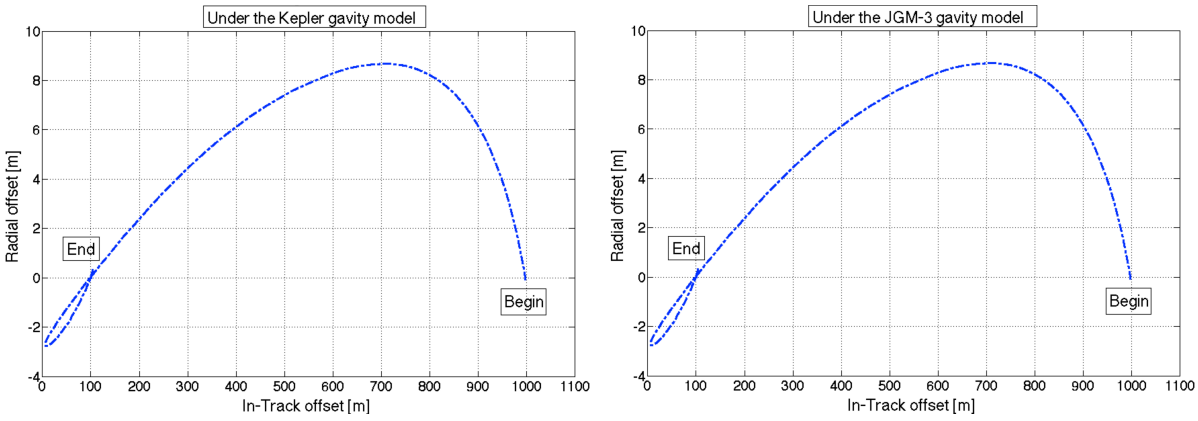

Figure 5.7. Software simulation of relative motion trajectory in the chief-centered rotating frame (Left: Kepler ; Right: JGM-3)

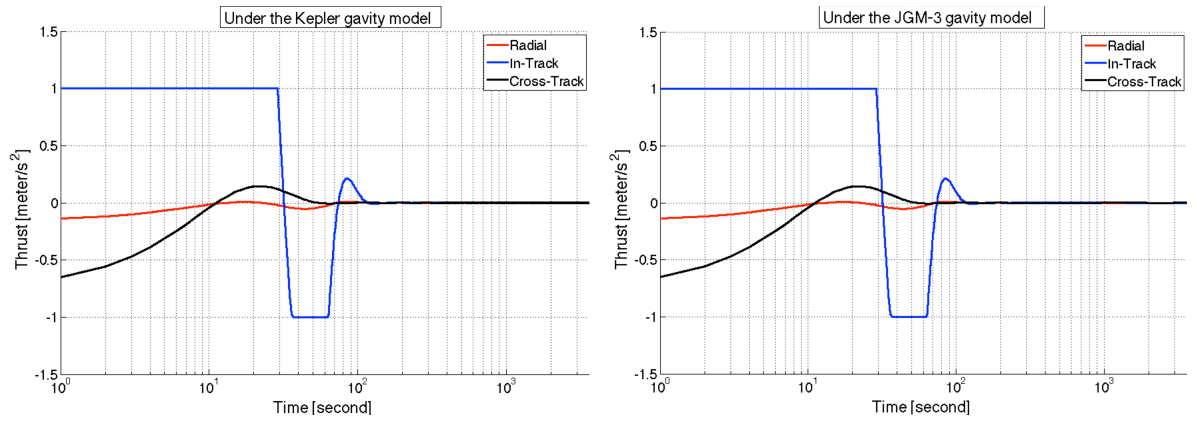

Figure 5.8. Thrust v.s. Time (Left: Kepler ; Right: JGM-3)

Thrust applied for the 1-hour MATLAB simulation with Kepler gravity model in radial, in-track and cross-track direction are 2.6280 m/s^2, 69.2121 m/s^2 and 6.4431 m/s^2, respectively; While the total thrust applied for the 1-hour MATLAB simulation with JGM-3 gravity model in radial, in-track and cross-track direction are 2.6260 m/s^2, 69.2118 m/s^2 and 6.4433 m/s^2, respectively. Because of the gravitational potential difference, the required thrusts to control the deputy are different between the Kepler case and the JGM-3 case. The JGM-3 case actually required slightly less fuel given the same set of initial kinetic conditions.

In conclusion, as shown from Fig. 5.6 to Fig. 5.8, software simulation results with Kepler gravity model are highly similar to the results with JGM-3 gravity model except a slightly different amount of thrust applied for the maneuver.

Overall, the software simulation results match the results of reference [5] fairly close. By comparing Fig. 5.6 with Fig. 5.3, the overshot of formation acquisition process in the Kepler or JGM-3 simulation is stronger than that of reference [5], which is caused by a different thrust limit. However, MATLAB simulations had shown the thrust limit applied by reference [5] is too low for the formation acquisition in this scenario. More details of the thrust limit are discussed in the next section. Because of the strong overshot, the closest in-track separation for these MATLAB simulations is about 5.2 meters, which seems too close from the perspective of potential collision hazard. Current simulations assume that the deputy spacecraft can apply thrust in any direction ideally. For safety concern, adding some restrictions to the control law in future formation-flying simulations, such as setting a safety zone can be considered. Besides, there is a disagreement of initial cross-track separation: The initial cross-track separation in reference [5] seems close to 0 according to Fig. 5.3, which is inconsistent with the calculated value of -65.2758 meters as shown in Table 3.

5.2.2. Thrust Limit Analysis

In a real scenario, the amount of thrust that the satellite can apply is limited. Understanding how this affects the control and total amount of thrust applied by the spacecraft is important. In this section, an analysis of the thrust cap is made with changes of the thrust limit being applied during the maneuver for the sample formation-flying scenario.

Variable thrust caps have been applied to the controller and the analysis results are shown in Fig. 5.9. The total thrust over the entire maneuver including formation keeping versus the thrust limit are plotted. Note that, each run was done with a given thrust limitation in meters per second, assuming that each thrust command was applied once every second. Therefore, a total ΔV is the integration of thrust in every second over the whole period of maneuver.

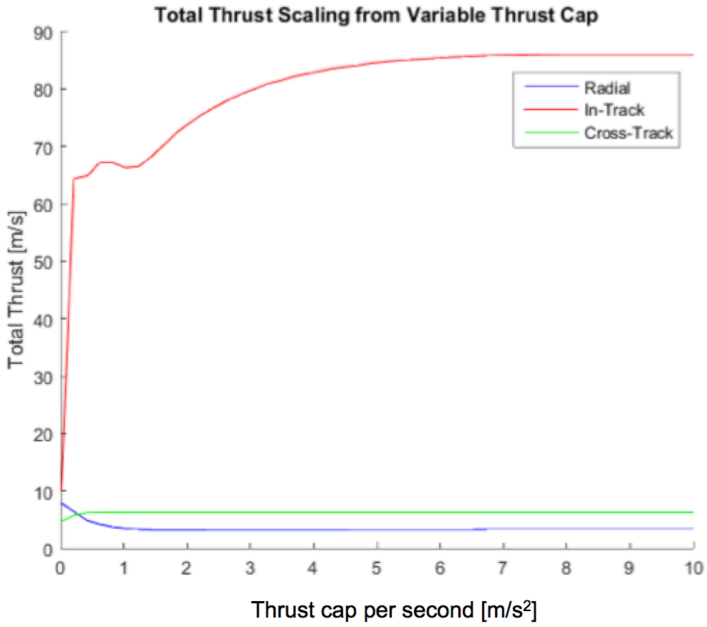

Figure 5.9. Total thrust v.s. Thrust cap

As shown in Fig. 5.10, the left portion of the plot in red background is a very low thrust cap region, which is unrealistic and would not be used for formation keeping and control. The thrust in such inoperable region is too low that the desired formation is never reached.

When the formation acquisition can be reached, the in-track total thrust required to get to the desired location has three distinct regions:

Region 1: As shown in blue background region in Fig. 5.10, this region is where the thruster is weak, but strong enough get the deputy spacecraft to the targeted state. The default thrust cap being set in the reference scenario is located in this region.

Region 2: This is the region where we can find the local minimum of fuel plan, where the thrust applied does not overshoot the desired location, and there is no need for correction, as shown in the green background in Fig. 5.10.

Region 3: The wide region is where there is overshoot during acquisition, and the controller must keep working to correct the overshoot, as shown in the yellow background region in Fig. 5.10. When the total thrust limitation is very high, the total thrust needed approaches a constant value. As the deputy spacecraft begins to approach the desired location, the controller begins commanding the Deputy to apply thrust in the opposite direction of motion. It would seem that this would be able to quickly stop the deputy spacecraft, but during the early portions of the acquisition the controller commands the deputy spacecraft to apply a large amount of thrust to get to the desired location. This large amount of thrust applied early on in the maneuver makes the approach to the desired location a bit “overzealous”, so the same large thrust capability that would allow it to stop quickly causes the deputy spacecraft to move too quickly when approaching. A pattern of oscillating relative distance will appear in such large thrust cap situation.

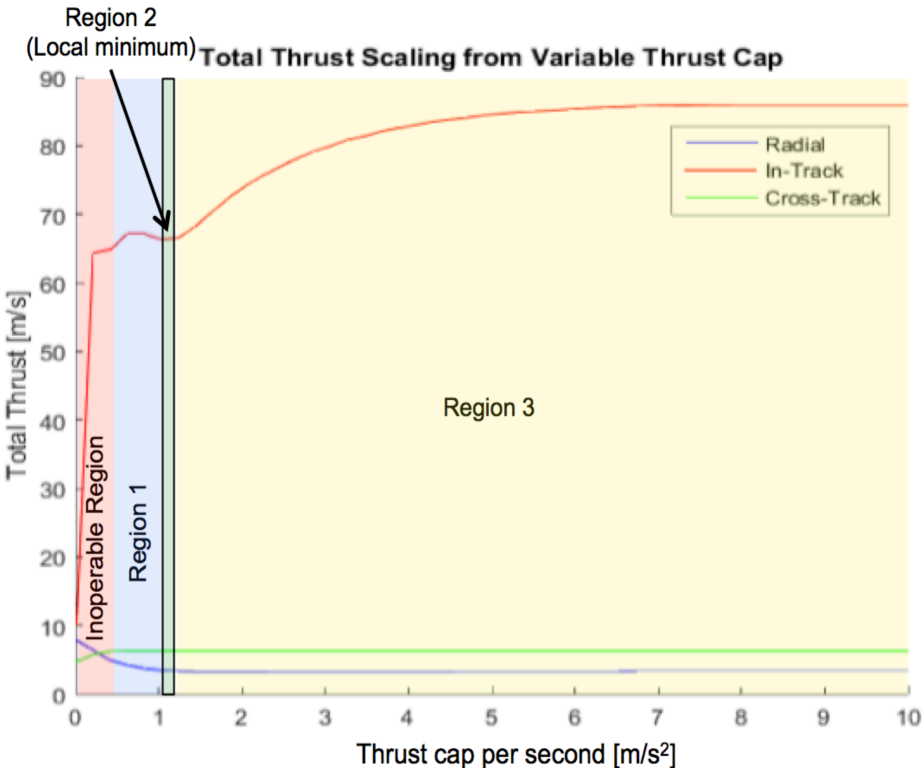

Figure 5.10. Demonstration of different characteristic regions of thrust cap

As shown in Fig. 5.11, the first 100 seconds of the simulation is the time frame where most of the formation acquisition occurs. After this time period the thrust needed to keep in formation is quite low, and stable.

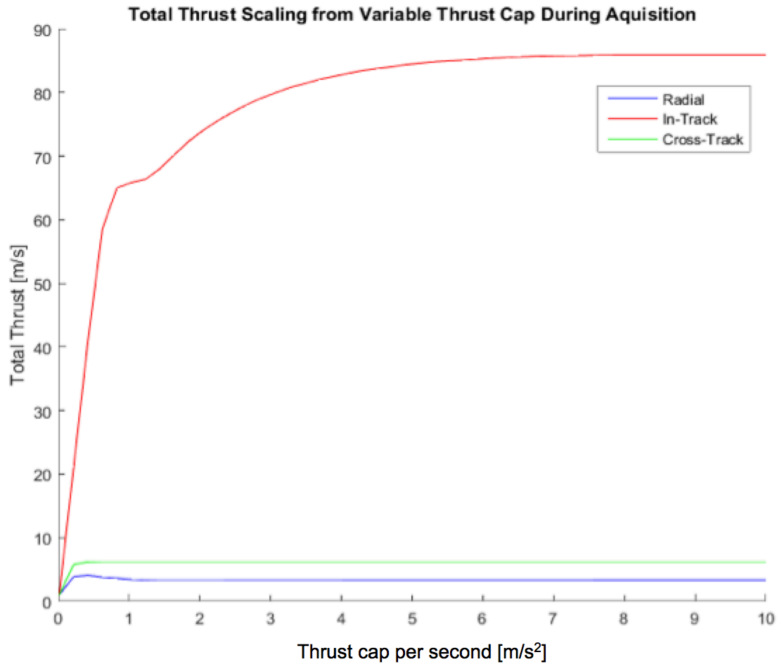

Figure 5.11. Total thrust during the first 100-s v.s. Thrust cap

5.3. Closed-loop HIL Simulation Results

Closed-loop HIL simulation of the entire VTFFTB has been completed and the results are presented and discussed in the following subsections.

5.3.1. Absolute and Relative Navigation Errors

The positioning performance of OEM628 receiver is evaluated by analyzing the absolute positioning errors in ECEF frame. 30 minutes data of the chief satellite are used for the analysis. The absolute navigation error is defined as the difference between the receiver navigation solutions and the positions logs in SimGEN. Note that, GPS L1, L2 & L5 signals with TEC correction are used to generate the absolute navigation solutions.

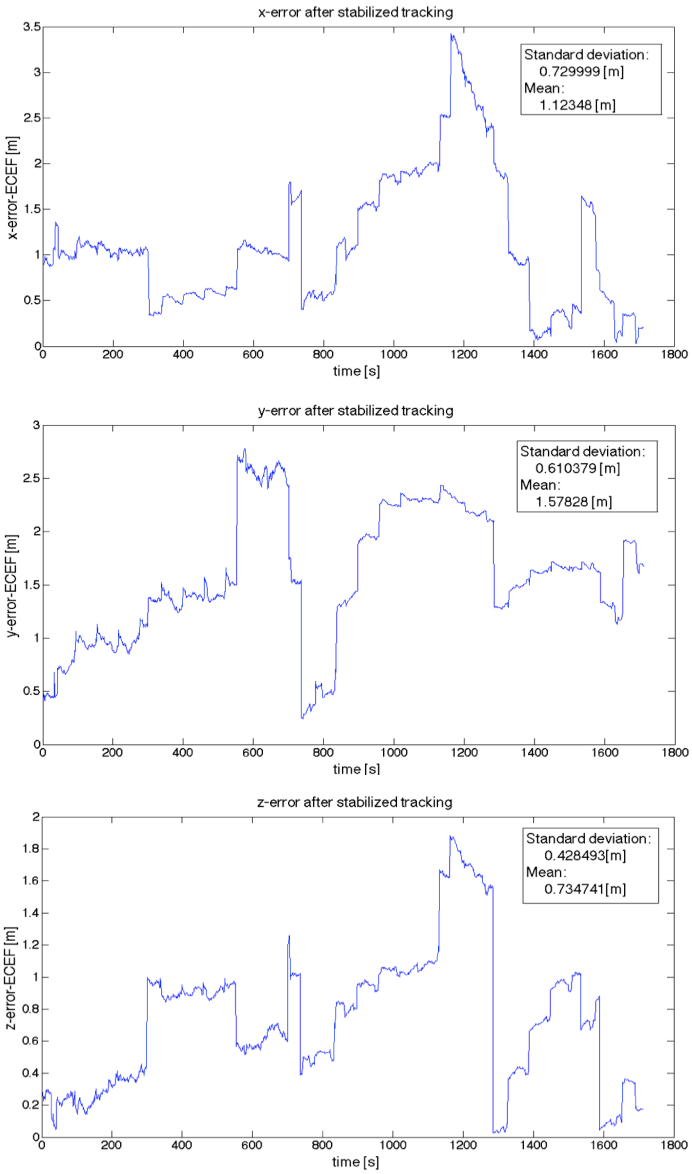

Figure 5.12. Absolute navigation errors in each ECEF direction (Up: x direction; Middle: y direction; Down: z direction)

As shown in Fig. 5.12, for most of the time, the absolute navigation error is smaller than 3 meters in x or y direction and smaller than 1 meter in z direction.

Relative navigation errors are computed and plotted in Fig. 5.13 and Fig. 5.14. Relative navigation error is defined as the difference between the relative states calculated from the logged chief & deputy data in SimGEN and the relative states estimated by the EKF. The average relative positioning errors are smaller than 1mm in each direction.

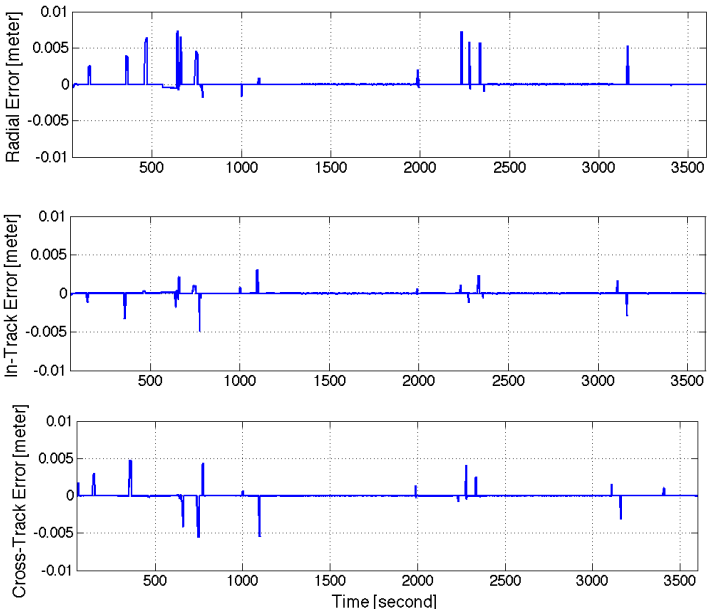

Figure 5.13. Relative position navigation errors in body frame

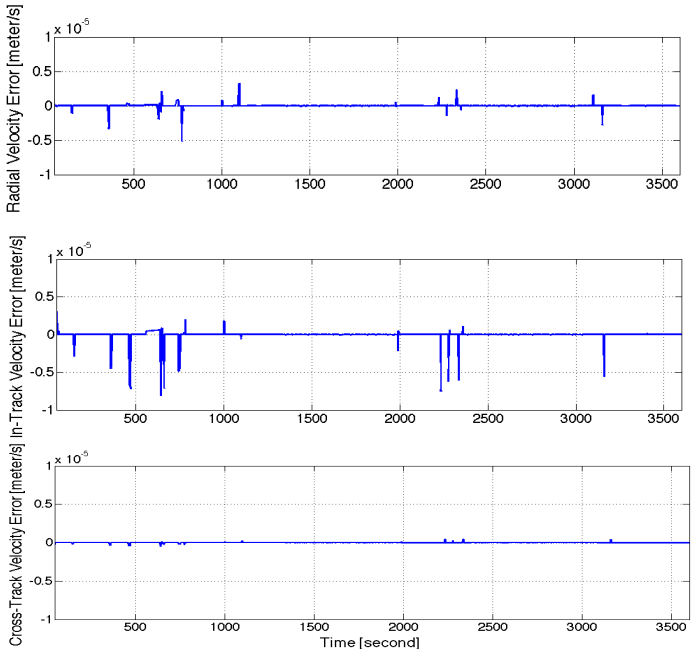

Figure 5.14. Relative velocity navigation errors in body frame

Direction	Position (m)		Velocity (m/s)	
	Mean	Std	Mean	Std
Radial	-0.001264	0.08018	$4.035*10^{-7}$	$2.452*10^{-5}$
In-track	0.0003057	0.0186	$1.397*10^{-6}$	$8.739*10^{-5}$
Cross-track	-0.0009881	-0.5866	$-9.865*10^{-8}$	$5.797*10^{-6}$

Table 6. Characteristics of relative navigation errors

5.3.2. Relative Positions During the Formation Acquisition and Keeping

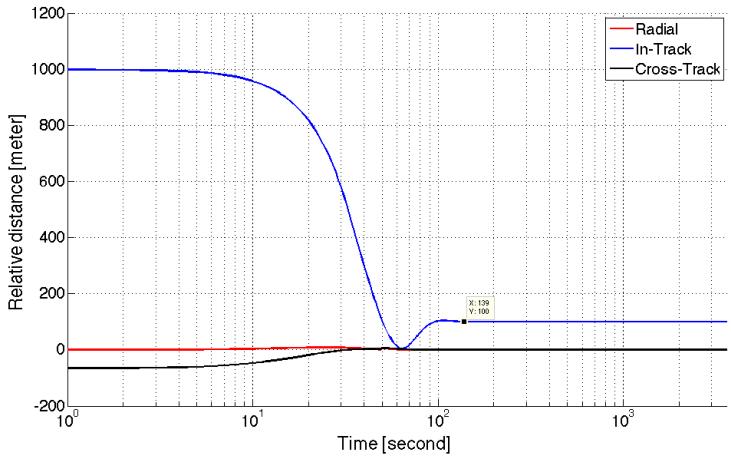

Figure 5.15. Relative position vector v.s. time during HIL simulation

The results in Fig. 5.15 are very consistent with the results in Fig. 5.3, except for a stronger overshoot and small slip occurred at 50 seconds and the cross-track direction disagreement as mentioned early. At 64 seconds, the in-track separation reached its minimum of 4.05 meters due to the strong overshoot. This overshoot can be understood as an under damped feedback system in terms of classic Feedback Control Theory. This implies adjusting parameters in the controller may allow reduction of this overshoot. Further work is planned to apply these concepts. The slip can be obviously seen from the result in chief-centered rotating frame coming next. The formation keep process starts at approximately 139 seconds, which is similar to reference [5]'s result of 141s.

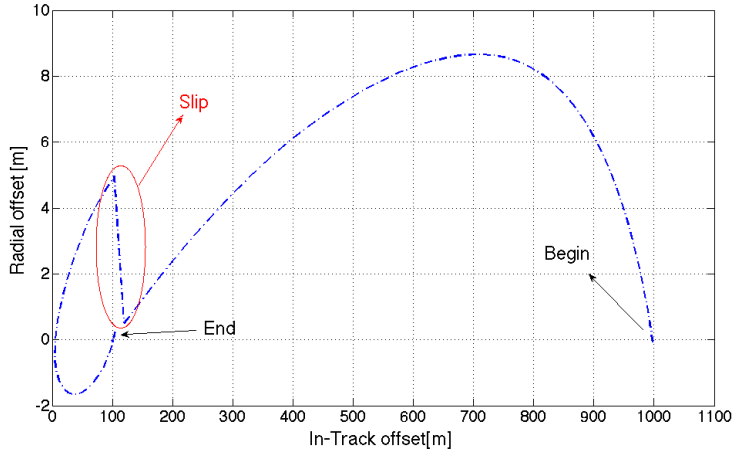

Figure 5.16. Relative motion trajectory in the chief-centered rotating frame during HIL simulation

Overall this result is basically consistent with the result of reference [5] except for the overshoot and sudden jump of the relative states, which is called the slip here, as seen in Fig 5.16. There are two potential reasons to cause the sudden slip: Firstly, the first run of EFK cannot give an accurate estimation for the relative states because of poor prior information (initial state covariance and initial measurement noise covariance). Secondly, the time between the navigation & control system is not consistent with the scenario time in SimGEN/simulator, which causing a large residual of measurement and degraded the state estimation from EFK. The characteristics of the time delay will be analyzed in section 5.3.4.

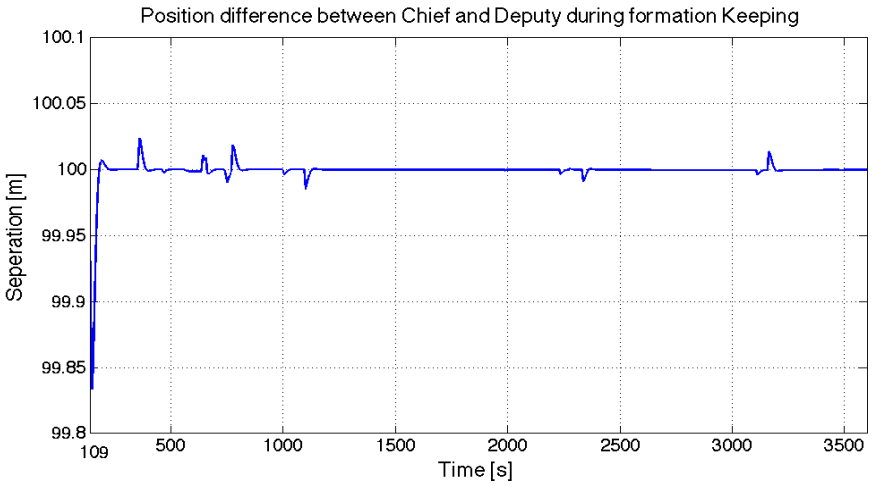

Figure 5.17. Position difference between the chief and deputy satellites during formation keeping

Fig. 5.17 shows the positions difference during the formation flying phase. In the along-track direction, the maximum error is 2.4 cm and the mean error is down to 1 mm. Characteristics of formation keeping process of the VTFFTB are summarized in Table 7, which outperform the results of reference [5] as shown in the table of Fig. 5.4 from the standpoint of stabilization.

	Radial (m)	In-track (m)	Cross-track (m)
Maximum	0.007660	100.0240	0.05873
Minimum	-0.05917	99.8335	-0.03592
Mean	-0.001448	99.9990	-0.00007901
RMS	0.006387	0.01165	0.004909

Table 7. Characteristics of formation keeping during the HIL simulation

5.3.3. Thrust Analysis

Total thrust applied during the 1-hour HIL simulation in radial, in-track and cross-track direction are 2.4550 m/s^2, 69.3347 m/s^2 and 6.7858 m/s^2, respectively. Total thrust of 69.2674 m/s^2 is required for the radial formation acquisition, whereas only 0.0673 m/s^2 is applied for the radial formation keeping. As shown in the Fig. 5.18, starting from 119 s, the thrust in all directions became low and stably. This indicates the desired state of formation flying is fairly fuel-efficient during the formation keeping

process. Compared to the corresponding results in in reference [5], much less thrust for formation keeping is required since the dynamics propagator of VTFFTB has not incorporated as many orbital perturbations.

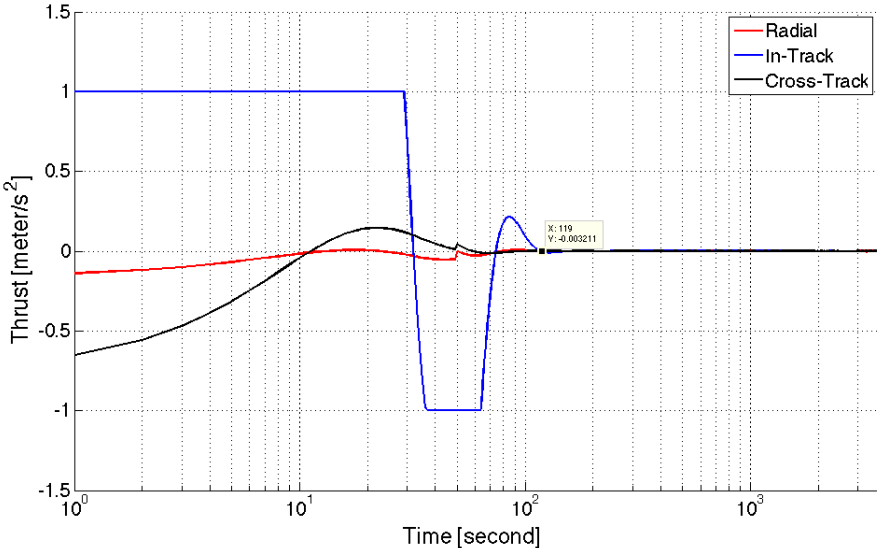

Figure 5.18. Applied thrust in each axis during the HIL simulation

Compared the HIL simulation result of thrusts with the software simulation, the total thrust in three directions in total is approximately 78.58 m/s^2, which is more than the 3-direction total thrust calculated from MATLAB simulation result of 78.28 m/s^2. Such 0.3 m/s^2 difference is spent on accounting all the "real world effects", including the measurement noise, processing noise, estimation errors, etc. from the hardware environment.

5.3.4. Timing Evaluation

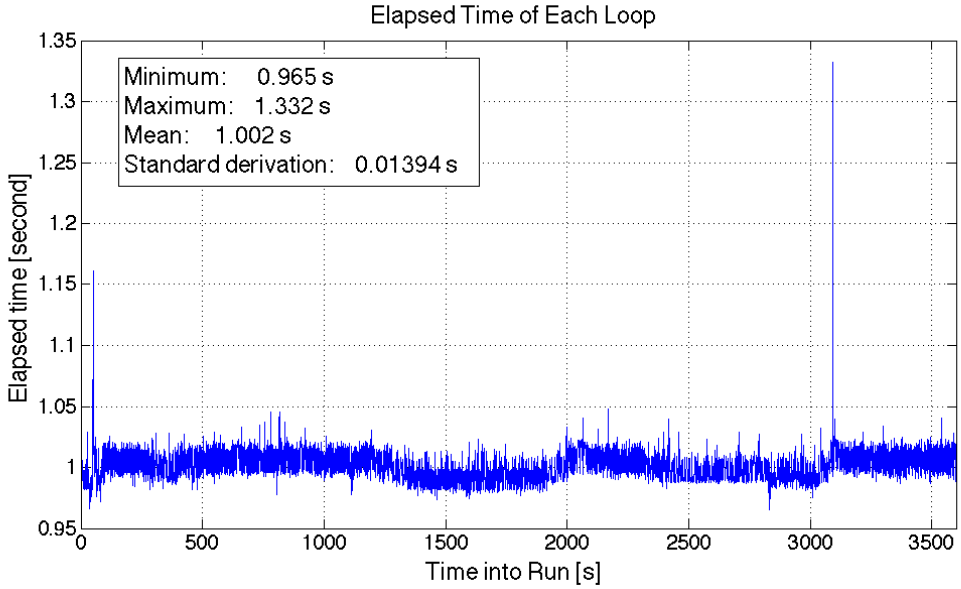

Figure 5.19. Recorded elapsed run time of each loop during the HIL simulation

The run time of each loop of the navigation & control system was recorded during the simulation and is plotted in Fig. 5.19. Obviously, without a time-synchronization system (e.g. timer card), the run time of each loop is not constant but variable and drifted up and down with a mean of 1.002 s. The maximum spike appear in the figure indicates the longest run time of a loop is 1.332 s, which is 33.2 % off the designed 1 s interval time. Fortunately, the overall run time of each loop is around 1 s and in most of the cases fluctuated within ± 0.02 seconds. The simulation began with a faster run but later on the run time of each loop increased. A timer card or clock will be added to the VTFFTB to improve the capability of time-synchronization.

Overall, the closed-loop HIL simulation of the GNSS-based spacecraft formation flying under the VTFFTB can reproduce all the results in reference [5] with a high level of consistency. Some minor differences are discussed and explained above. These results have validated the feasibility and evaluated the performance of the VTFFTB for spacecraft formation flying simulation via benchmarking with reference [5].

Chapter 6

Application to Ionospheric Remote Sensing

6.1. Multi-constellation GNSS TEC Measurement and Model Evaluation System

Historically, dual-frequency GPS (or Glonass) receivers are widely used for TEC measurements. Currently, there are 12 Galileo satellites and 21 Beidou satellites in orbit operationally with more planned to be launched. Compared with previous single/dual-constellation TEC measurements, tracking more constellations greatly increases the number of ionospheric piercing points to be measured, which potentially improves the measurement accuracy and quality. As a comparison, STK simulation of GPS-only constellation and all current GNSS satellites are shown in Fig. 6.1.

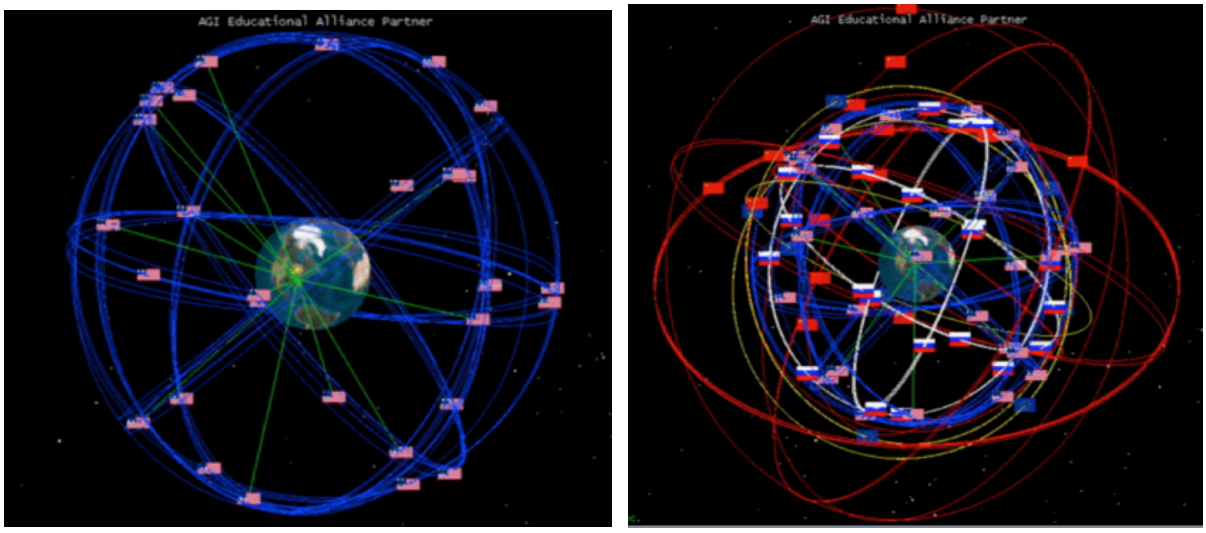

Figure 6.1. Left: GPS only (Past) v.s. Right: GPS + GLONASS + Galileo + Beidou (Today)

A multi-frequency multi-constellation GNSS TEC measurement and model evaluation system are developed to take advantages of the growing GNSS for TEC monitoring and ionospheric effects analysis. The system can determine ground-based vertical TEC combining GPS, GlONASS, Galileo, and Beidou constellations, as well as evaluate the Klobuchar, NeQuick and CIM (Beidou) TEC models with measurement data.

The software algorithm of the system is outlined in Fig. 6.2. GPStation-6 receiver is used to generate slant TECs for GPS, Glonass and Galileo constellations respectively. Next, the slant TECs are converted to vertical TECs after addressing the satellite and receiver bias. Meanwhile, MATLAB software has been developed to process the raw GNSS measurement data from OEM628 and generate the vertical TECs for GPS, Glonass, Galileo and Beidou constellations from measurements, as well as the vertical TECs of Klobuchar, NeQuick and CIM models based on the corresponding propagating coefficients. The GPStation-6 receiver has internal software to process the data and produce

ground-based TEC, and it has been used as a benchmarking tool to develop space-based TEC software to process the GNSS measurement data from OEM628 receiver.

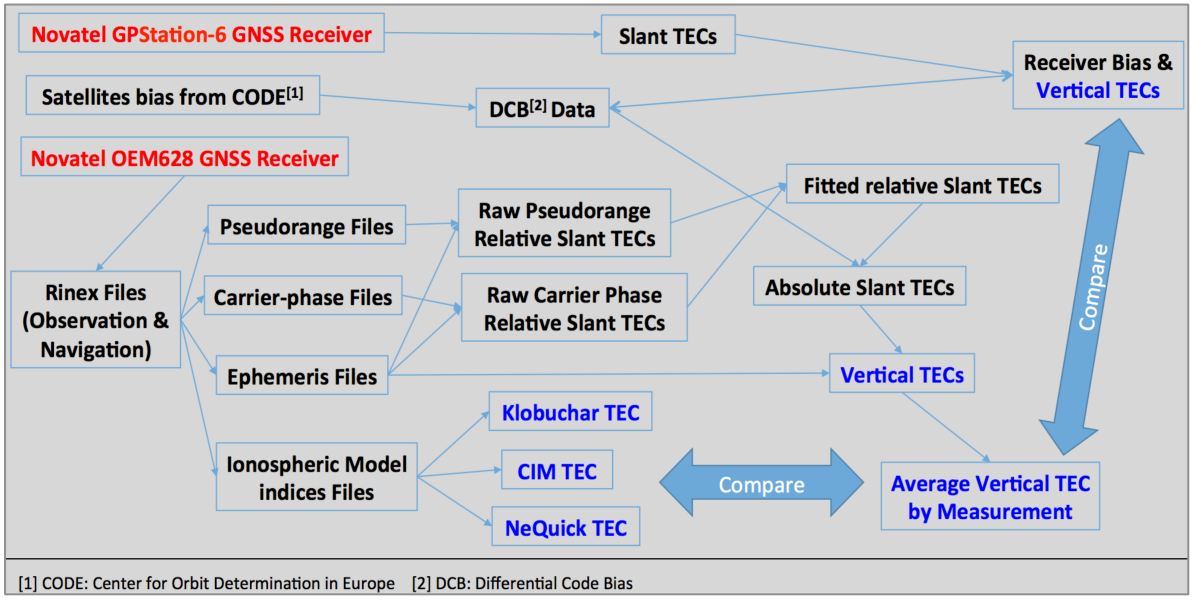

Figure 6.2. Flow Diagram of TEC Data Processing

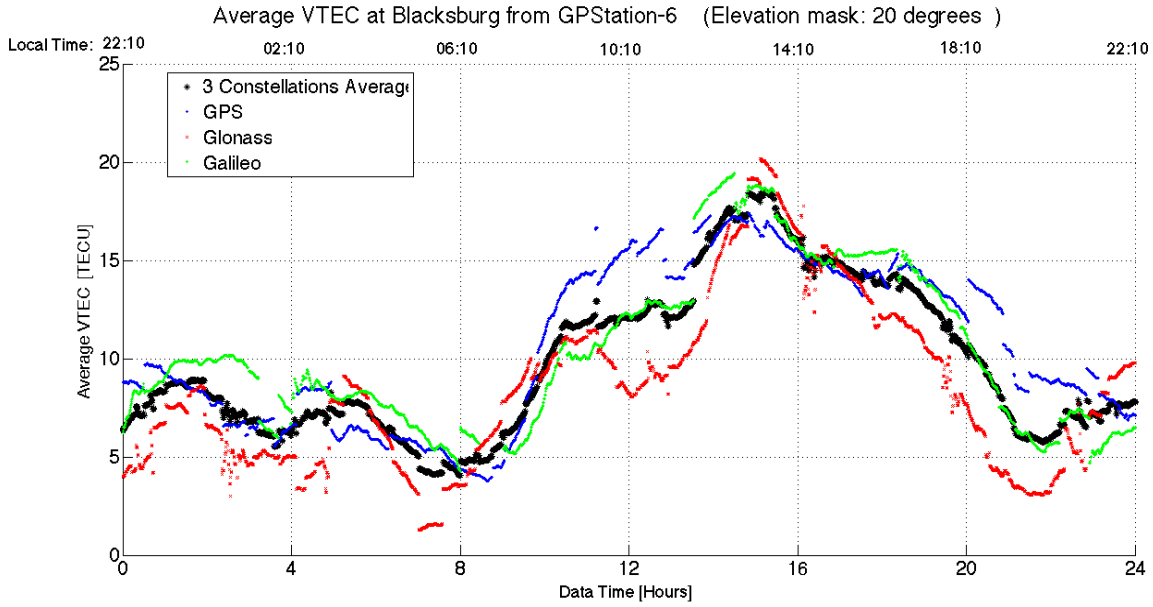

Figure 6.3. Vertical average TEC measured at Blacksburg

Vertical average TECs at Blacksburg measured by GPStation-6 are shown in Fig. 6.3. The blue one is GPS TEC, red one is GLONASS TEC and the green one is Galileo TEC. The average of three-constellation gives the black curve. Starting from 10:10pm (EDT) on October 28, 2016, the sample data were taken 24 hours continuously at Blacksburg, VA (37.205° N, 80.417° W). An elevation mask is set as 20 degrees to eliminate the noisy data.

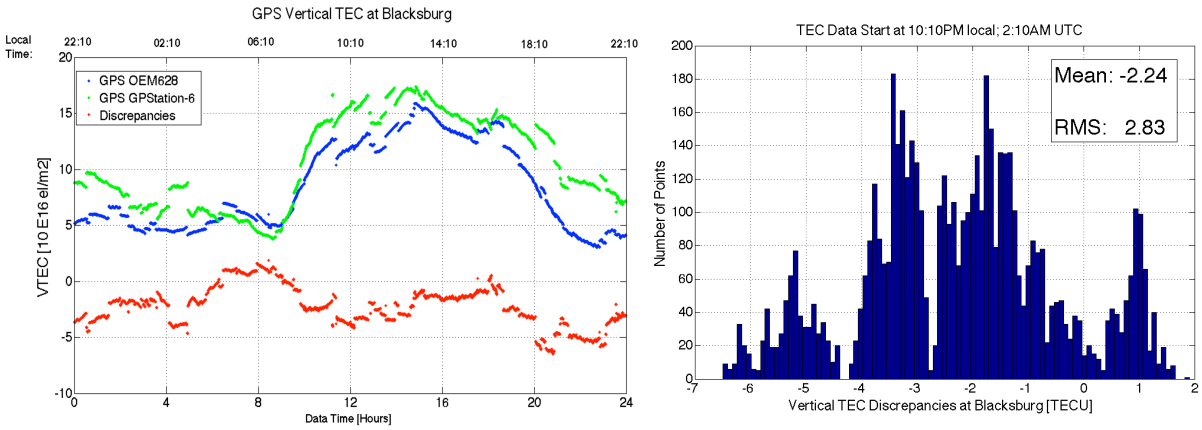

Figure 6.4. Left: Comparison of GPS vertical TEC generated between two different receivers; Right: Corresponding Histogram of TEC discrepancies

To validate the TEC processing of the software, the GPS vertical TEC generated between two receivers are compared as shown in Fig. 6.4. On the left plot, GPS TEC generated by the software from OEM628 data is in blue, the TEC measured by GPStation-6 are processed and plotted in green and the discrepancies are computed in red. As shown in the right of Fig. 6.4, a mean discrepancies of -2.24 TECU and RMS of 2.83 TECU prove a reasonable good consistency between two TEC and validates the software is capable to produce the right TEC.

Next, the TEC model evaluation function is introduced and presented. Three constellations are implementing the TEC model for single frequency user to correct ionospheric delay:

① **Klobuchar** is the 2D TEC model being used in GPS constellation. 8 coefficients are modulated with the broadcast GPS RF signals to drive the TEC value at a specific location and time. As a simple model, the Klobuchar model assumes the night time TEC is minimum and constant. The ionospheric delay δt of the Klobuchar model can be expressed as [37]:

$$\delta t = F_s\left[5\times10^{-9} + A_I\cos\left(\frac{2\pi(t-50400)}{P_I}\right)\right] \quad \text{(in seconds)} \qquad \textbf{(64)}$$

where:

F_s = slant factor

A_I = amplitude of ionospheric delay

t = local time at Ionospheric Pierce Point (IPP)

P_I = period of ionospheric delay

② **NeQuick** is a 3D electron density model used in Galileo constellation. The model is driven by the effective ionization level, which is controlled by 3 broadcast coefficients. Plus the time and location,

the TEC can be derived by integrating the electron density along the line of sight between GNSS satellite and receiver.

③ **Compass Ionospheric Model (CIM)** is the TEC model used by Beidou constellation. CIM is similar to Klobuchar model except threes differences: First, CIM uses a geographical reference frame while Klobuchar uses a geomagnetic frame. Second, the slant factor or mapping function of CIM is a sine function while Klobuchar is an approximation of sine function. Third, the 8 model coefficients are updated every 2 hours in Beidou for CIM while every few days to 10 days in GPS for Klobuchar. It is worth mentioning that, in order to guarantee a symmetric daily TEC structure between dawn side and dusk side, an upper limit for the period P_I in the model should be set. Say:

$$P_I \le P_I^{\max} = 4 \times (86400 - 50400) = 4 \times 3600 = 14400 \quad \textbf{(65)}$$

A comparison is made in Fig. 6.5 to illustrated the impact of setting: $P_I^{\max} = 14400$

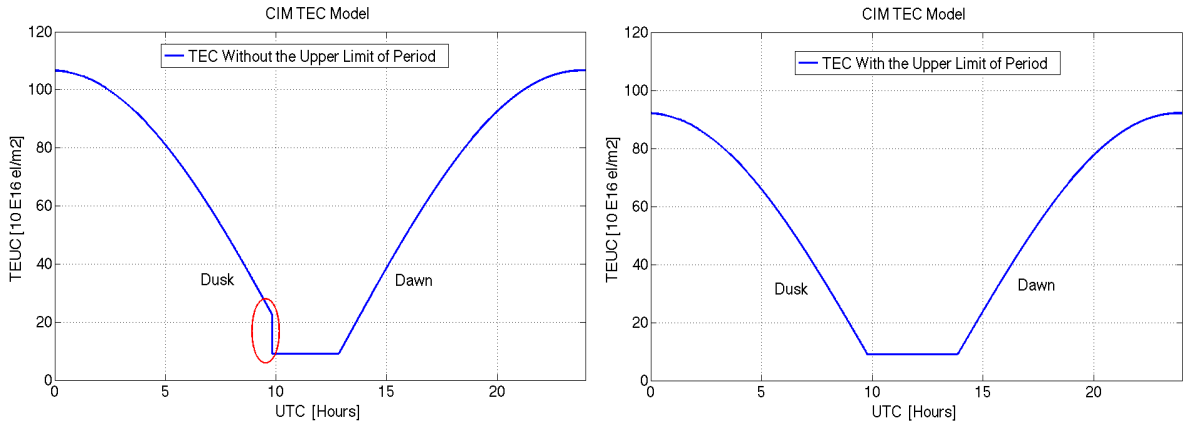

Figure 6.5. Illustration of the impact of setting a upper limit on the period in CIM

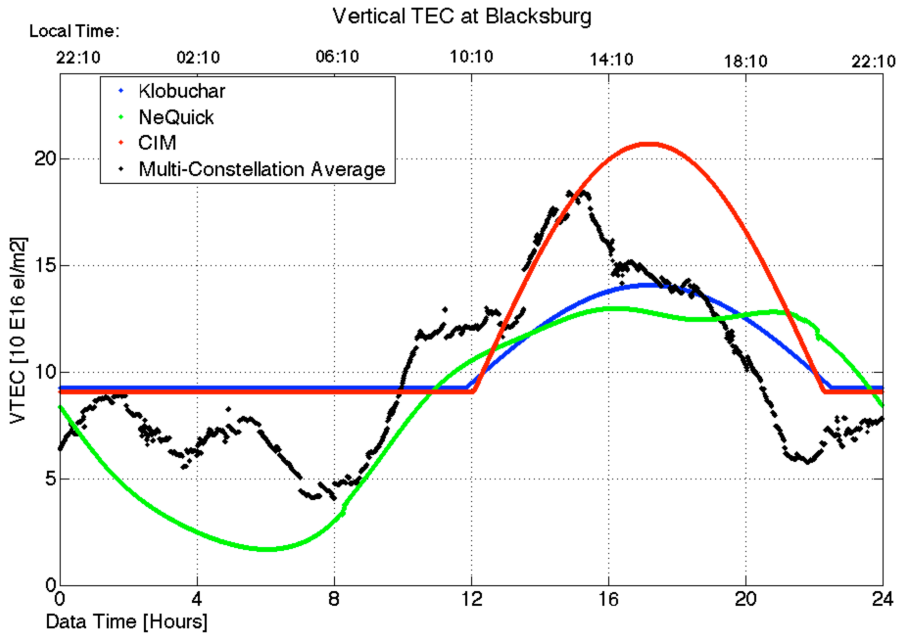

Figure 6.6. Compare three TEC models with multi-constellation average TEC measurements

The TEC models of GPS, Galileo and Beidou constellations are plotted together with the GPStation-6 multi-constellation average TEC measurement in Fig. 6.6. The blue one is Klobuchar, the red one is CIM, the green one is NeQuick, and the black one is the multi-constellation measurement average. Both the Klobuchar and CIM TEC peak at 3pm local time, while the measurement TEC peaks at around 1 pm local time. The Klobuchar peak value is about 4 TECU lower than the measurement peak, while the CIM peak value is about 2 TECU higher than the measurement peak. The night-time TEC of NeQuick model is not constant but has a trough, which is more realistic from the standpoint of measurement.

Furthermore, the TEC software and the measured data have been validated by benchmarking with another TEC software of Rinex GPS-TEC developed by Dr. Gopi Krishna Seemala as well as the raw data from the World-wide GPS Receiver Network in MIT Madrigal Database. Hence, this multi-constellation GNSS TEC measurement system can be used for multi-constellation TEC monitoring/measurement and model evaluation. Thus, diurnal variation or long term TEC trend can be studied. A 7-day TEC monitoring at Blacksburg by GPStation-6 are shown in Fig. 6.7.

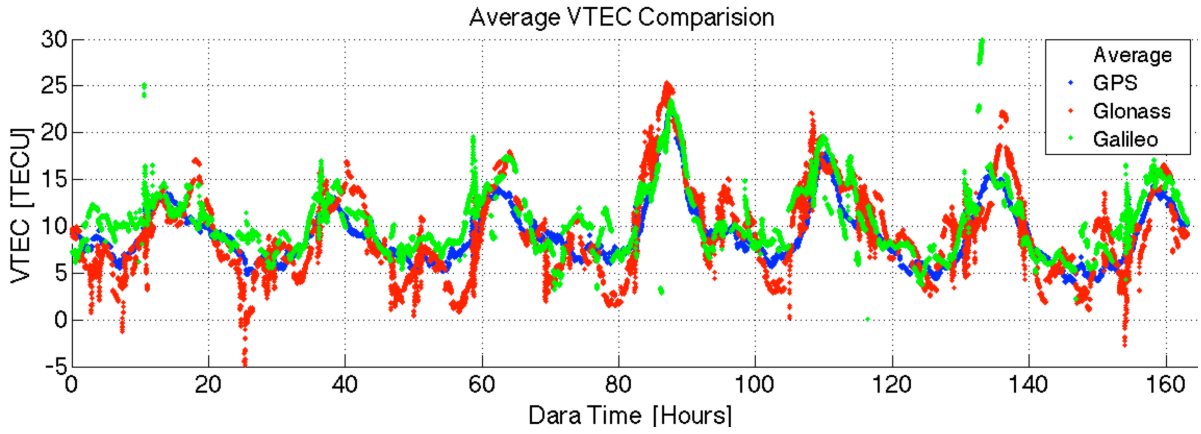

Figure 6.7. 7-day ground-based TEC monitoring by GPStation-6 at Blacksburg

Last but not the least, this system can also be integrated with the HIL spacecraft formation flying simulation testbed to design future satellite-beacon ionospheric remote sensing missions, which will be covered in section 6.2.

6.2. Ionospheric Irregularity Remote Sensing Mission Demonstration

Ground based instrument or space based satellites have frequently observed various types and scales of irregularities in the ionosphere. However the production mechanism of ionospheric irregularities has not been fully understood due to the lack of accurate observations or robust modeling. To further understand the physics of ionospheric irregularities, precise measurements with high resolution are demanded. Satellites formation flying can be applied in ionospheric remote sensing. For instance, by taking advantage of the onboard GNSS receivers, the electron density or scintillation can be probed in a higher level of resolution.

Sporadic E (Es), thin layers with irregular electron density, is one type of ionospheric irregularity that exists in the E region of the ionosphere. Ground-based remote sensing techniques are mostly used to observe Es in the past, while satellite-beacon remote sensing missions were involved in the probing recently. In 2005, Wu at JPL studied Sporadic E morphology from satellite radio occultation data of the CHAMP mission and the COSMIC missions [38]. In this section, a scenario of Sporadic E is designed and used to demonstrate how to apply spacecraft formation flying and differential-TEC technique to detect and measure the Sporadic E.

According to ionosonde and incoherent scatter radar measurements, Es layers often appear at the altitude of 90 - 110 km, with the vertical thickness of 0.5 - 5 km and a horizontal scale of 10 - 1000 km [38]. Therefore the altitude of the satellites orbit should be about 100km. The polar orbit (89 degree inclination) is selected in order to probe the Es in low-latitude, mid-latitude and high-latitude regions.

Let's assume there exists a homogeneous Es layer at an altitude of 101 km. As illustrated in Fig. 6.8 below, vertically the Es region ranges from 100.5 km to 101.5 km with the thickness of 1000 m, and horizontally the width of the Es region is about 500 km. Given a pair of spacecraft are travelling together below the Es region in the velocity of v_0.

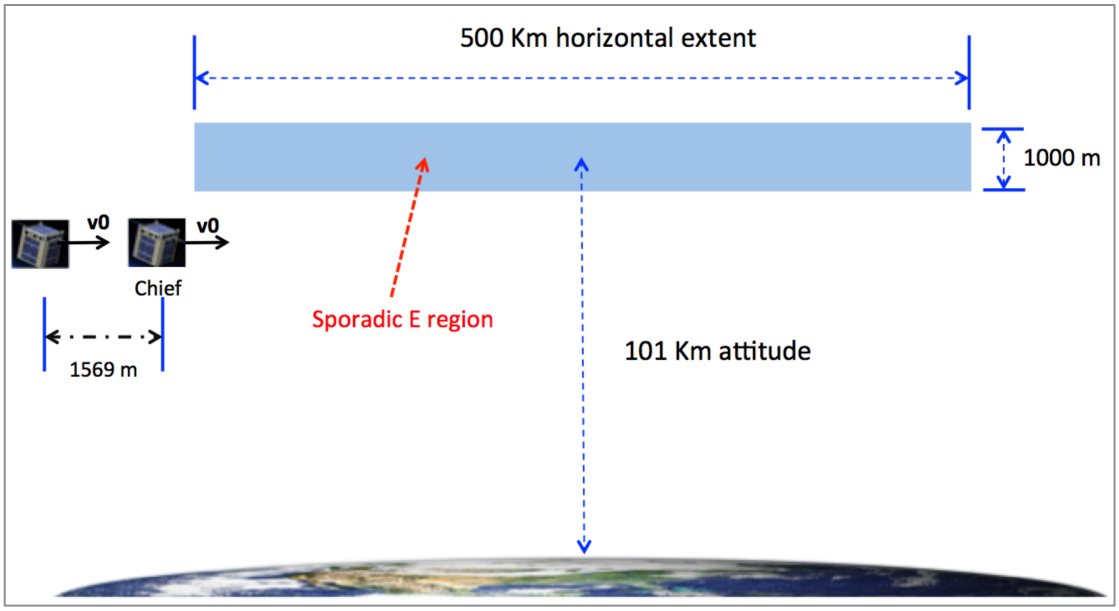

Figure 6.8. Initial setup of the remote sensing scenario

The initial relative orbit is a leader–follower formation flying in an in-track separation of 1569 m before the maneuver. The objective is to achieve and maintain a relative orbit with 2000 m radial offset and zero offset in the other two direction. Through the formation acquisition process, the two spacecraft can probe the top-side and bottom-side of an Es region through the radial direction maneuver of the deputy spacecraft. By taking the difference of vertical TEC measured by two spacecraft (at different altitude but same longitude and latitude) with onboard GNSS receivers, the electron density between the spacecraft can be estimated. When the deputy spacecraft crosses the

vertical edge of Es region, a gradient of electron density might occur in the observation data, depending on the physics and morphology of the irregularity. The scenario of deputy satellite passing the Es region during the formation acquisition is as shown in Fig. 6.9.

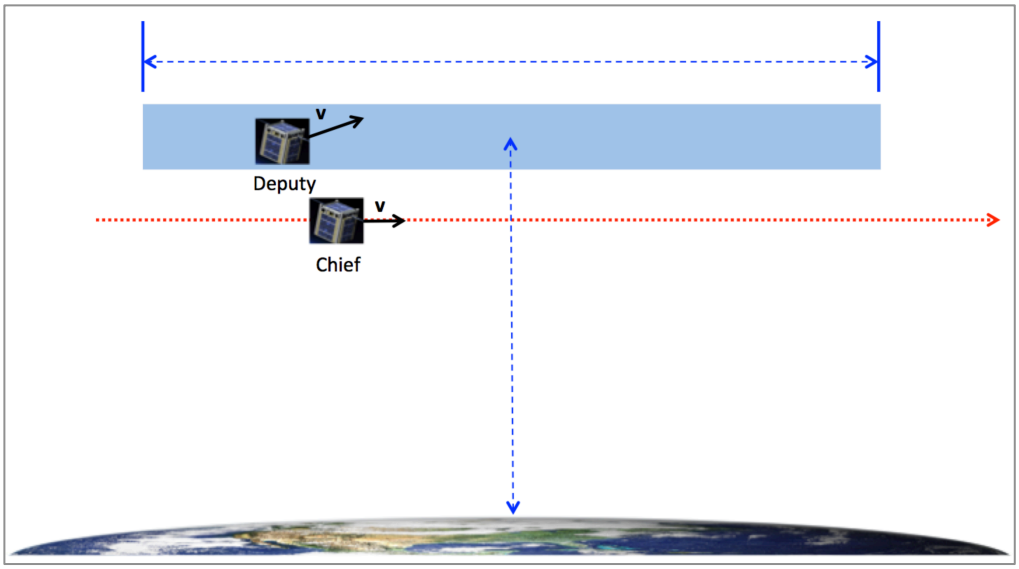

Figure 6.9. Formation acquisition stage of the remote sensing scenario

Meanwhile as the two spacecraft travel horizontally, the horizontal boundary of Es region might induce a gradient of TEC, which allows us to identify the horizontal range of the irregularity region. The final stage of the formation keeping will be a 2000-m radial offset formation flying configuration as shown in Fig. 6.10.

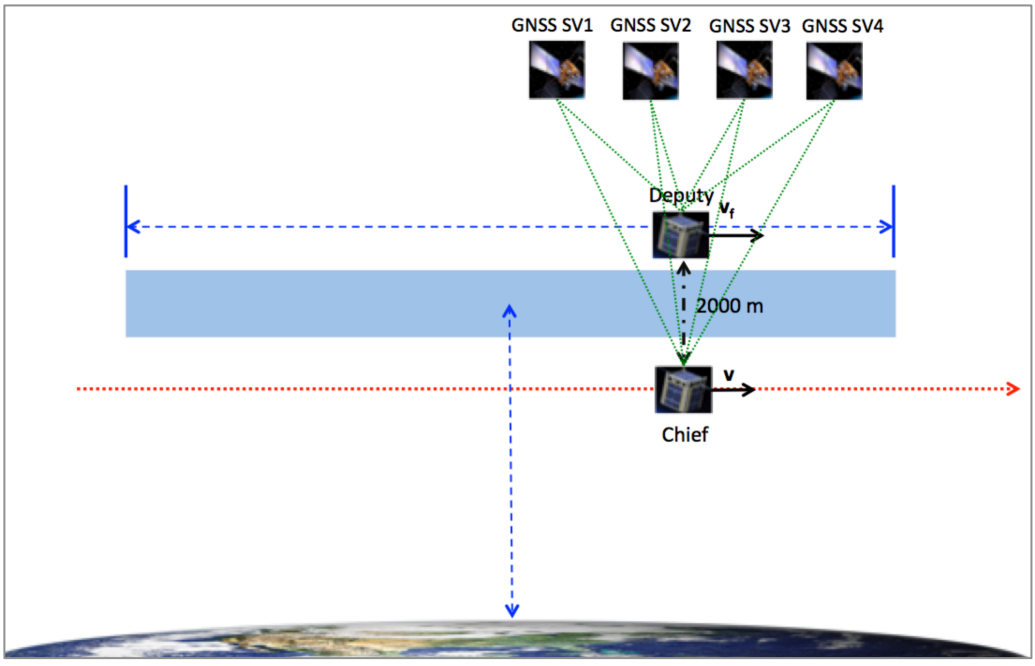

Figure 6.10. Formation keeping stage of the remote sensing scenario

MATLAB, STK and SimGEN were used to design the mission orbit for this scenario. A set of initial conditions for this remote sensing scenario is summarized in Table 8.

Orbital Elements	**Chief spacecraft**	**Deputy spacecraft**
Semi-major axis (a) (m)	6478140	6478150
Eccentricity (e)	2.57212×10^{-15}	9.41351×10^{-7}
Inclination (i) (°)	89	89
Argument of perigee (ω) (°)	0	0
Longitude of ascending node (Ω) (°)	286.842 (RAAN: 0 °)	287.062 (RAAN: 0 °)
True anomaly (V)(°)	0	0.0140257
ECEF Values		
x (m)	6478140	6478139.8100
y (m)	0	27.3798
z (m)	0	1568.5840
v_x (m/s)	0	-1.8996
v_y (m/s)	136.8990	136.8990
v_z (m/s)	7842.92	7842.9196
a_x (m/s^2)	-9.4831	-9.4831
a_y (m/s^2)	0.0001	0
a_z (m/s^2)	-0.0001	-0.0024

Table 8. Initial orbital elements and ECEF state vectors of the remote sensing scenario

The corresponding initial relative position and velocity are calculated and list them in Table 9. While the desired relative states are listed in Table 10.

Radial separation (m)	-0.1900	Radial relative velocity (m/s)	0
In-track separation (m)	1568.8229	In-track relative velocity (m/s)	-0.0001
Cross-track separation (m)	0	Cross-track relative velocity (m/s)	0

Table 9. Initial relative states in body frame of the remote sensing scenario

Radial separation (m)	2000	Radial relative velocity (m/s)	0
In-track separation (m)	0	In-track relative velocity (m/s)	0
Cross-track separation (m)	0	Cross-track relative velocity (m/s)	0

Table 10. Desired relative states in body frame of the remote sensing scenario

Close-loop HIL simulation of this remote sensing scenario has been conducted in the VTFFTB and the key results are presented as follows. Note that, the thrust limit was reset as 10 m/s^2 for this remote sensing scenario in order to provide a stronger controllability and complete the formation acquisition faster. Generally, a larger thrust cap would enable faster maneuver to complete the formation acquisition.

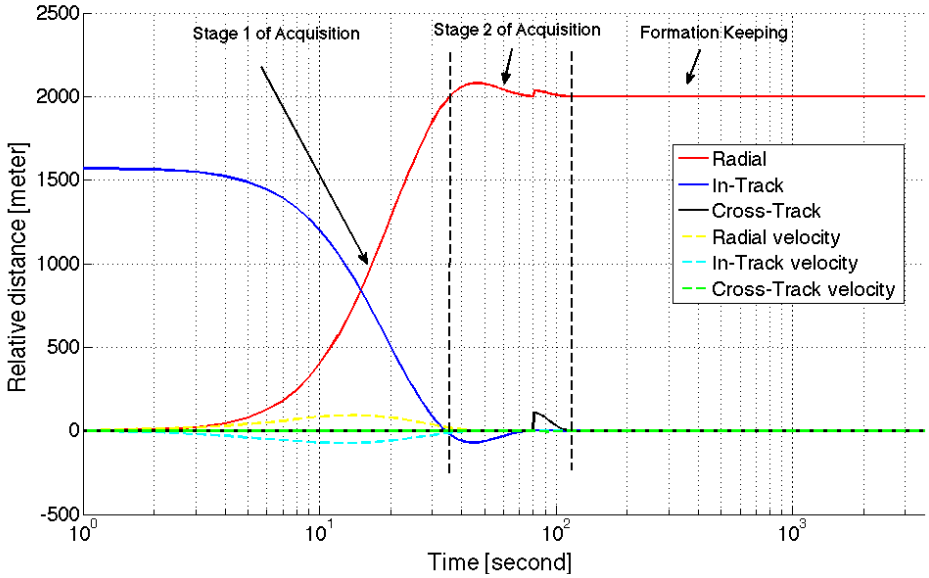

Figure 6.11. Relative States v.s. time during HIL simulation of the remote sensing scenario

It took 36 seconds to drive the deputy spacecraft to the desired 2000-m radial separation firstly, as shown as the stage 1 of formation acquisition in Fig. 6.11. At 113 s, the desired formation-flying configuration is successfully achieved and enters the formation keeping status. In the stage 2 of formation acquisition, a sudden slip occurs for radial and cross-track relative position, which is caused by the lack of time-synchronization or the poor first estimation of the EFK as discussed earlier.

In the speed of approximately 7850 m/s, the spacecraft travelled ~ 282.6 km during the stage 1 and ~ 887.1 km during the formation acquisition. Therefore, the results of horizontal travelling distance can satisfy the goal of detecting the boundary of the Es region with 500 km extent using differential-TEC technique.

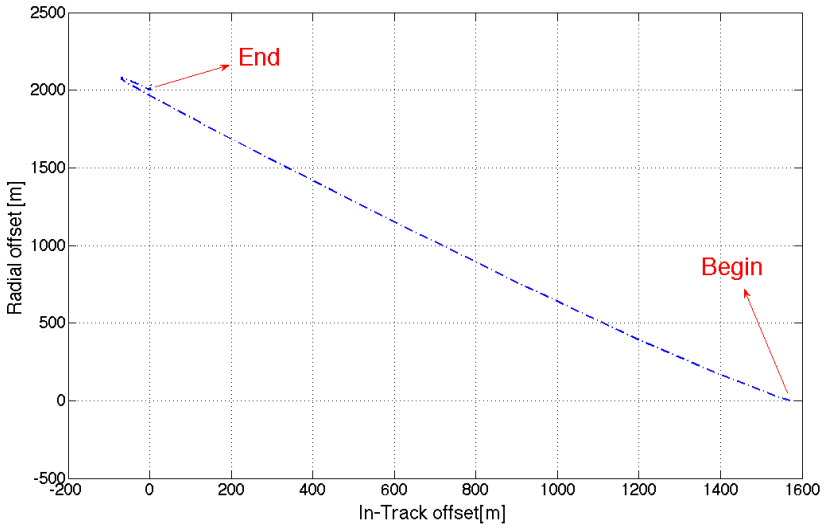

Figure 6.12. Relative motion trajectory in the chief-centered rotating frame during HIL simulation

As shown in Fig. 6.12, the initial along-track separation is decreased to the zero while the radial offset is increased to 2000 m during the formation flying.

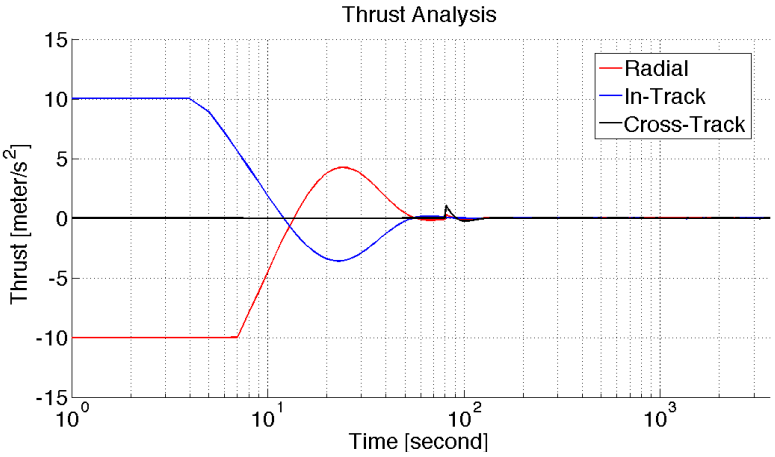

Figure 6.13. Applied thrust in each axis during the HIL simulation of remote sensing scenario

Total thrust applied during the 1-hour HIL simulation for this remote sensing scenario in radial, in-track and cross-track direction are 223.8653 m/s^2, 155.1403 m/s^2 and 10.5918 m/s^2, respectively. Total thrust of 192.9028 m/s^2 and 154.9667 m/s^2 are required for the radial and in-track formation acquisition respectively, whereas 30.6732 m/s^2 and 0.1320 m/s^2 are applied for the radial and in-track formation keeping respectively. Maintaining zero radial offset for two-satellite formation flying are relatively fuel consuming, and flying satellites on a 100-km altitude will be very fuel consuming to main the altitude too. Therefore, this remote sensing scenario is very unrealistic in terms of the energy efficient perspective. There is a lot of room to improve the reconfiguration of new orbit scenarios for spacecraft formation flying. For instances, once the desired 2000-m radial separation is achieved and the horizontal boundary is detected, there is no need to maintain the same configuration any more, which can save a certain amount of fuel. Also, it might be better to let the deputy spacecraft fly ahead of the chief spacecraft initially. Once the maneuver begins, the deputy spacecraft just need to slow down and increase the orbital radius (altitude), which may consume much less fuel for the formation acquisition phase.

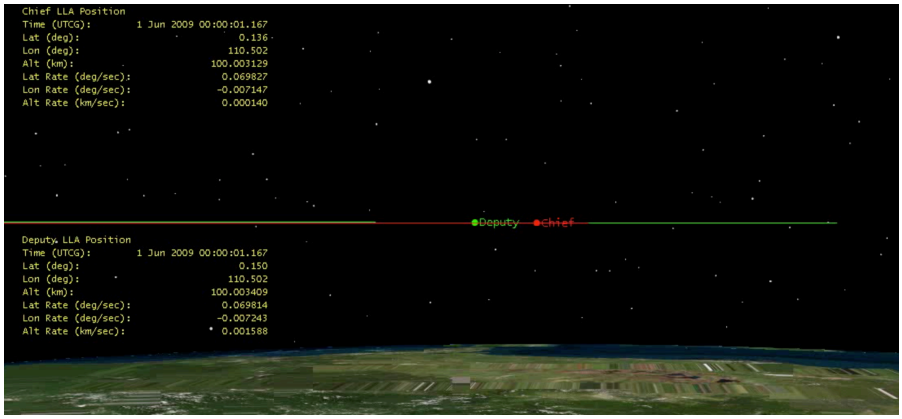

Figure 6.14. Initial orbits of two spacecraft in STK

The formation acquisition of this scenario's HIL simulation has been replayed in STK visualization system (As shown in Fig. 6.14, Fig. 6.15 and Fig. 6.16).

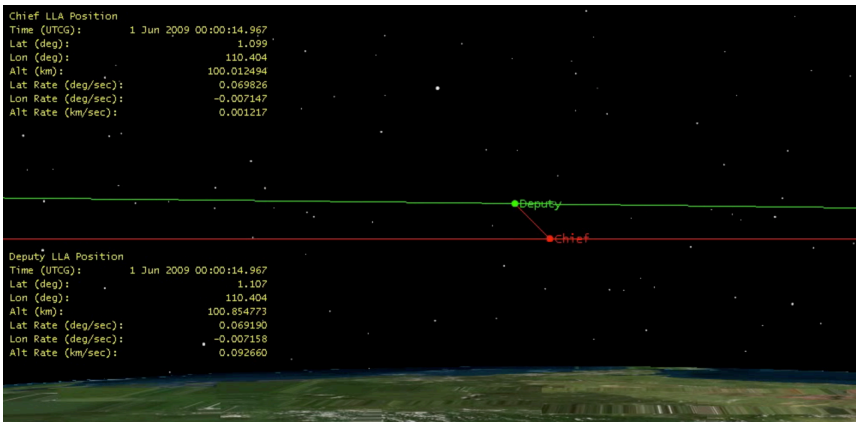

Figure 6.15. Relative orbit at 15 seconds during the formation acquisition in STK

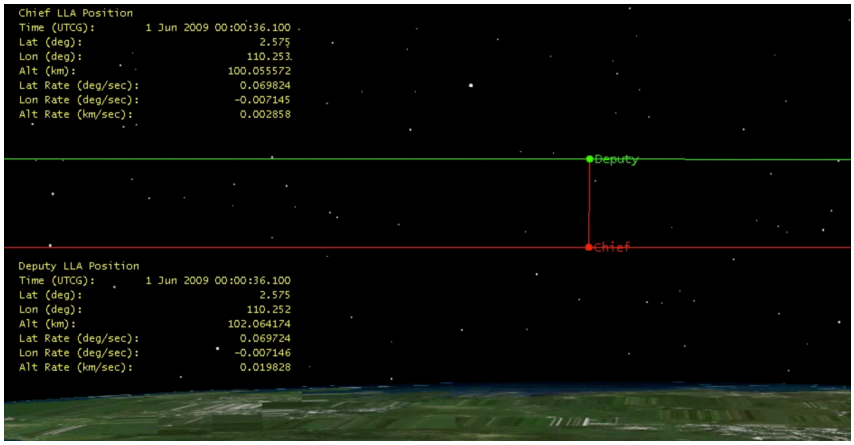

Figure 6.16. Relative orbit at 36 seconds during the formation acquisition in STK

As an initial attempt, this experiment has demonstrated the VTFFTB can be applied on a new scenario for remote sensing mission purpose and the VTFFTB will be a very useful platform to test future GNNS-based spacecraft formation flying mission given a specific application or observation target.

6.3. Subsystem of Multi-constellation Multi-frequency GNSS Scintillation Monitoring

A multi-constellation multi-frequency GNSS scintillation-monitoring platform has been developed using the GPStation-6 receiver as a subsystem of the GNSS ionospheric weather monitoring system at Virginia Tech. Currently the platform can generate ground-based GNSS scintillation data at Blacksburg, VA including L1, L2 & L5 bands of GPS, L1 & L2 bands of GLONASS and E1, E5a & E5b bands of Galileo. The subsystem can produce GNSS scintillation indices of CN_0 (carrier noise

ratio), S4 (amplitude scintillation index) and Sigma Phi (phase scintillation index), which can be exploited to characterize both the amplitude and phase scintillation of mid-latitude regions based on long-term observation. An example of 7-day S4 index measurement at Blacksburg is shown below.

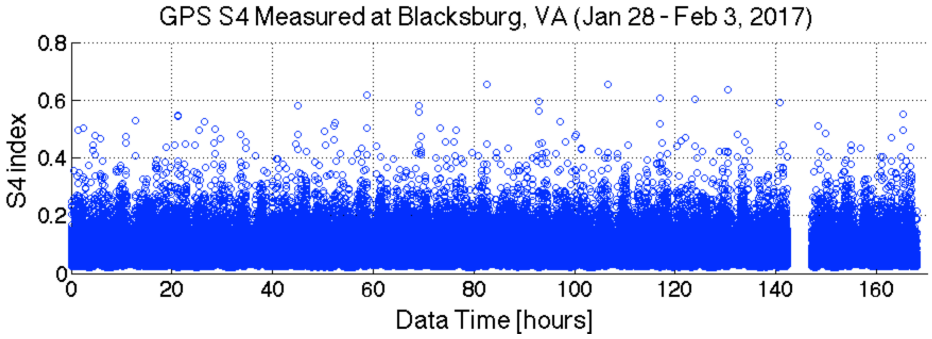

Figure 6.17. GPS S4 index 7-day Measurement at Blacksburg

Our observations have found relatively high scintillation level and large spatial gradient of TEC, when the ionospheric piercing points (IPPs) of GNSS satellites passed through ionospheric irregularity areas detected by the Super Dual Auroral Radar Network (SuperDARN) Blackstone radar. Such joint observation between SuperDarn and GNNS scintillation on mid-latitude ionospheric irregularity had been conducted in the past to investigate impact of plasma wave cascading processes on the formation of mid-latitude irregularities [39]. An illustration of such in-conjunction measurement is shown in Fig. 6.18.

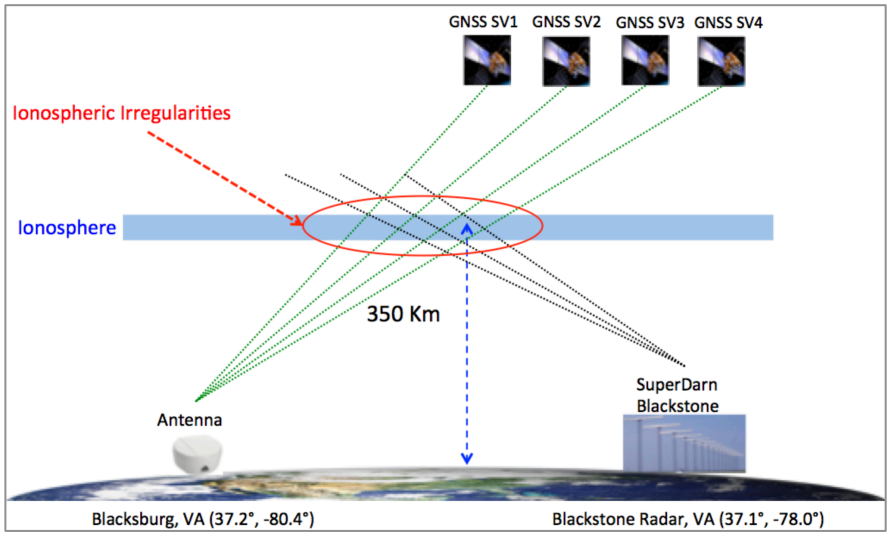

Figure 6.18. Demonstration of ionospheric irregularities in-conjunction measurement

It's important to note, this subsystem can be utilized as a benchmark to develop future space-based GNSS scintillation measurement technique using the OEM628 receiver. Ultimately, the multi-constellation TEC measurement system can be integrated with this subsystem on the VTFFTB for space-based ionospheric irregularities observation mission development.

Chapter 7

Summary and Conclusion

7.1. Summary

The GNSS-based Virginia Tech Formation Flying Testbed (VTFFTB) for closed-loop LEO spacecraft formation flying simulation has been developed. The preformation of the VTFFTB has been tested and evaluated. The simulation results have been validated by benchmarking with reference [5]. The VTFFTB is comprised of Spirent GNSS simulators, Novatel multi-constellation GNSS receiver(s), the Navigation & Control system and the STK visualization system. The Navigation & Control system mainly consist of a dynamics propagator based on a 8×8 JGM-3 gravity model and the non-linear interpolation principle, a GNSS measurement system using single-differential pseudorange model for relative navigation, an EKF system for relative states estimation and a flight control system using SDRE control technique.

The same scenario established in reference [5] is used for setting up the initial conditions of the closed-loop HIL simulation for testing and validation. The reference scenario of two LEO spacecraft begins with an initial in-track separation of 1 km and aims to eventually accomplish a formation keeping with 100 m along-track offset only. Both the software (MATLAB) and the closed-loop HIL simulations were performed for the 1-hour reference scenario, and the results are consistent with that of reference [5]. Particularly, the thrust cap analysis is carefully made based on MATLAB simulations, and the elapsed run time of each loop was recorded to assess the time consistency of HIL simulations. Besides the slip issue caused by the lack of proper time-synchronization and the fuel consumption difference caused by slightly different orbital perturbations, the overall functionalities of the VTFFTB are evaluated. In conclusion, the reproduced results demonstrate that the newly established closed-loop HIL simulation testbed at Virginia Tech is capable of supporting the developments of GNSS-based spacecraft formation flying missions.

To take advantage of the rapidly growing GNSS, the multi-constellation (GPS, GLONASS, Galileo and Beidou) GNSS TEC measurement and model evaluation system has been developed for higher-accuracy TEC monitoring and ionospheric irregularity study. Meanwhile, the subsystem of multi-constellation multi-frequency GNSS scintillation platform has been established with the objective to characterize mid-latitude scintillation, investigate ionospheric irregularities and potentially be integrated with the VTFFTB for satellite mission development. The integration of multi-constellation GNSS TEC measurement technique and the VTFFTB was applied to develop a LEO satellite formation flying mission for ionospheric remote sensing. A scenario of sporadic E observation is designed and illustrated to demonstrate how to implement differential-TEC method and GNSS-based spacecraft formation-flying mission to probe the irregularity region. More novel satellite formation flying missions for ionospheric remote sensing can be developed on the VTFFTB with the implementation of multi-constellation GNSS remote sensing systems at Virginia Tech.

7.2. Issues and Future Work

According to the assessment of time consistency, the timing between the simulator and navigation & control is not synchronized. This would cause the inconsistency between the real-time GNSS measurements and the measurement model predictions and induce a large measurement residual, which could be detrimental to the performance of EFK estimations. All these negative effects together would result in the occurrence of slip in the HIL simulation results, as seen early in Fig. 5.17 and Fig. 6.11. In short, currently the primary issue is time-asynchronization and the first future work is to make the time synchronized among different systems of the VTFFTB.

Additional control laws may need to be added into the controller for safety concern. The simulation results of the reference scenario indicated that the minimum separation between spacecraft might be too close because of the overshoot. Therefore, the SDRE controller in the current navigation & control system should be upgraded by setting a safety zone to avoid a potential collision hazard.

Potential future work can be enumerated below in priority order:

1) Install timer card/clock to synchronize different components in the testbed;
2) Upgrade the measurement model from single-difference pseudorange to CDGPS;
3) Upgrade the dynamics propagator by incorporating a higher order JGM-3 gravity model and more orbital perturbations, which would make the simulation more realistic;
4) Update the corresponding EFK based on the new measurement technique and new dynamics propagator;
5) Upgrade the SDRE controller by adding additional control law to avoid potential collision;
6) Upon the completion of step 1 - 5, try to conduct full GNSS-based satellite formation flying remote sensing simulations and produce convincing results including the ionospheric remote sensing data. Meanwhile, attempt to design new formation flying configurations of the mission scenario, such as adding a third spacecraft or design new orbits with better fuel plan;
7) Add Galileo into the system by activating the Spirent GSS7800 Galileo simulator, which might increase both the navigation accuracy and remote sensing resolution.

Reference

[1] Parker, J., Valdez, J., Bauer F., Moreau M., Use and Protection of GPS Sidelobe Signals for Enhanced Navigation Performance in High Earth Orbit, American Astronautical Society, AAS 16-72, 2016.

[2] Kowalchuk, S.A., Investigation of nonlinear control strategies using GPS simulator and spacecraft attitude control simulator, PhD dissertation, Virginia Polytechnic Institute and State University, Virginia, 2007.

[3] Montenbruck, O., Gill, E., Satellite Orbits, Springer-Verlag, Heidelberg, Germany, 2001.

[4] Westerhoff, J., Earle, G., et. al., LAICE CubeSat mission for gravity wave studies, Advances in Space Research, Volume 56, Issue 7, Pages 1413–1427, 2015.

[5] Park, J.-I., Park, H.-E., Park, S.-Y., Choi, K.-H., Hardware-in-the-loop simulations of GPS-based navigation and control for satellite formation flying, Advances in Space Research, Vol. 46, No. 11, pp. 1451–1465, 2010.

[6] Galileo Frequency bands. Available at: http://galileognss.eu/galileo-frequency-bands/

[7] BeiDou Signal Plan. Available at: http://www.navipedia.net/index.php/BeiDou_Signal_Plan

[8] Fejer, B., Kelley, M. C. , Ionospheric irregularities, Rev. Geophys., 18(2), 401–454, 1980.

[9] Chen, F.F., Introduction to Plasma Physics and Controlled Fusion Plasma Physics, New York, 1984.

[10] Alfriend, K. T., Vadali, S. R., Gurfil, P., How, J. P. and Berger, L. S., Spacecraft Formation Flying: Dynamics, control and navigation, Elsevier, Great Britain, 2010.

[11] Cluster_II_operations. Available at:
http://www.esa.int/Our_Activities/Operations/Cluster_II_operations

[12] The GRACE mission website. Available at: http://www.csr.utexas.edu/grace/

[13] The SWARM mission website. Available at:
http://www.esa.int/Our_Activities/Observing_the_Earth/Swarm

[14] The MMS mission website. Available at: https://mms.gsfc.nasa.gov/

[15] Precision Formation Flying at NASA JPL. Available at:
https://scienceandtechnology.jpl.nasa.gov/precision-formation-flying

[16] Gong, S., Li, J., BaoYin, H., Formation flying solar-sail gravity tractors in displaced orbit for towing near-Earth asteroids, Celestial Mechanics and Dynamical Astronomy, 105: 159, 2009.

[17] Guinn, J. R., Boain, R. J., Spacecraft Autonomous Navigation for Formation Flying Earth orbiters Using GPS, Astrodynamics Conference, San Diego, CA, U.S.A., 1996.

[18] Leitner, J. A Hardware-in-the-Loop Testbed for Spacecraft Formation Flying Applications, IEEE Aerospace Conference, Big Sky, MT, 2001.

[19] Gill, E., Naasz, B., Ebinuma, T., First Results from a Hardware-in-the-Loop Demonstration of Closed-Loop Autonomous Formation Flying, 26th Annual AAS Guidance and Control Conference, Breckenridge, USA, AAS 03-040, 2003.

[20] Burns, R., Naasz, B., Gaylor, D., Higinbotham, J., An Environment for Hardware-in-the-Loop Formation Navigation and Control, AIAA/AAS Astrodynamics Specialist Conference and Exhibit, Providence, USA, AIAA, 2004-4735, 2004.

[21] Mohiuddin, S., Psiaki, M. L., Satellite Relative Navigation Using Carrier-Phase Differential GPS with Integer Ambiguities, AIAA Guidance, Navigation, and Control Conference and Exhibit, San Francisco, California, 2005.
[22] Mohiuddin, S., Humphreys, T. E., Psiaki, M. L., A Technique for Determining the Carrier Phase Differences between Independent GPS Receivers during Scintillation, Proc. ION GNSS 20th, Fort Worth, TX, 2007.
[23] Mohiuddin, S., Psiaki, M. L., High-Altitude Satellite Relative Navigation Using Carrier-Phase Differential Global Positioning System Techniques, Journal of Guidance, Control, and Dynamics, Vol. 30, No. 5, 2007.
[24] Leung, S., Montenbruck, O., Real-time navigation of formation-flying spacecraft using global positioning system measurements, Journal of Guidance, Control, and Dynamics. 28 (2), 226–235, 2005.
[25] Yamamoto, T., D'Amico, S., Hardware-in-the-loop demonstration of GPS-based autonomous formation flying, Presented at the NAVITEC, Noordwijk, Netherlands, 2008.
[26] Ebinuma, T., Bishop, R. H., Lightsey, E. G., Integrated Hardware Investigations of Precision Spacecraft Rendezvous Using the Global Positioning System, Journal of Guidance, Control, and Dynamics, Vol. 26, No. 3, 2003.
[27] Marji, Q., Precise Relative Navigation for Satellite Formation Flying Using GPS, Master thesis, University of Calgary, 2008.
[28] Eyer, J. K., A Dynamics and control algorithm for low Earth orbit precision formation flying satellites, Ph.D. thesis, University of Toronto, 2009.
[29] Harris, F. B., Jr., GNSS Hardware-In-The-Loop Formation and Tracking Control, Master thesis, Virginia Polytechnic Institute and State University, Virginia, 2016.
[30] Spirent Communication plc., SIMGEN SOFTWARE USER MANUAL, DGP00686AAA, 2012.
[31] OEM628 Product Sheet. Available at:
http://www.novatel.com/assets/Documents/Papers/OEM628.pdf
[32] GPStation-6 Product Sheet. Available at:
http://www.novatel.com/assets/Documents/Papers/GPStation-6.pdf
[33] Integrating STK with Matlab. Available at:
http://help.agi.com/stk/index.htm#training/StartMatlab.htm
[34] Spirent Communication plc., SimREMOTE User Manual, DGP00792AAA, 2008.
[35] Spirent Communication plc., VEHICLE REFERENCE FRAMES AND VEHICLE MOTION HANDLING IN SimGEN (PC) SOFTWARE, DGP01062AAA, 2011.
[36] Mohiuddin, S., Psiaki, M. L., Satellite relative navigation using carrierphase differential GPS with integer ambiguities, in: Presented at the AAIA Guidance, Navigation, and Control Conference and Exhibit, 2005.
[37] Kintner, P. M., Jr., Global Positioning System Theory and Design, Ithaca, New York, 1999.
[38] Wu, Dong L., et al., Sporadic E morphology from GPS-CHAMP radio occultation, Journal of Geophysical Research, Vol. 110, A01306, 2005.
[39] Eltrass, A., Scales, W. A., Erickson, P. J., Ruohoniemi, J. M., Baker, J. B. H., Investigation of the role of plasma wave cascading processes in the formation of midlatitude irregularities utilizing GPS and radar observations, Radio Sci., 51, 836–851, 2016.

Appendix

Table of 8×8 JGM-3 Earth Gravity Field (Conventional Coefficients)

n	m	C	S
2	0	-0.10826360229840D-02	0.0
3	0	0.25324353457544D-05	0.0
4	0	0.16193312050719D-05	0.0
5	0	0.22771610163688D-06	0.0
6	0	-0.53964849049834D-06	0.0
7	0	0.35136844210318D-06	0.0
8	0	0.20251871520885D-06	0.0
2	1	-0.24140000522221D-09	0.15430999737844D-08
3	1	0.21927988018965D-05	0.26801189379726D-06
4	1	-0.50872530365024D-06	-0.44945993508117D-06
5	1	-0.53716510187662D-07	-0.80663463828530D-07
6	1	-0.59877976856303D-07	0.21164664354382D-07
7	1	0.20514872797672D-06	0.69369893525908D-07
8	1	0.16034587141379D-07	0.40199781599510D-07
2	2	0.15745360427672D-05	-0.90386807301869D-06
3	2	0.30901604455583D-06	-0.21140239785975D-06
4	2	0.78412230752366D-07	0.14815545694714D-06
5	2	0.10559053538674D-06	-0.52326723987632D-07
6	2	0.60120988437373D-08	-0.46503948132217D-07
7	2	0.32844904836492D-07	0.92823143885084D-08
8	2	0.65765423316743D-08	0.53813164055056D-08
3	3	0.10055885741455D-06	0.19720132389889D-06
4	3	0.59215743214072D-07	-0.12011291831397D-07
5	3	-0.14926153867389D-07	-0.71008771406986D-08
6	3	0.11822664115915D-08	0.18431336880625D-09
7	3	0.35285405191512D-08	-0.30611502382788D-08
8	3	-0.19463581555399D-09	-0.87235195047605D-09
4	4	-0.39823957404129D-08	0.65256058113396D-08
5	4	-0.22979123502681D-08	0.38730050770804D-09
6	4	-0.32641389117891D-09	-0.17844913348882D-08
7	4	-0.58511949148624D-09	-0.26361822157867D-09
8	4	-0.31893580211856D-09	0.91177355887255D-10
5	5	0.43047675045029D-09	-0.16482039468636D-08
6	5	-0.21557711513900D-09	-0.43291816989540D-09
7	5	0.58184856030873D-12	0.63972526639235D-11
8	5	-0.46151734306628D-11	0.16125208346784D-10
6	6	0.22136925556741D-11	-0.55277122205966D-10

7	6	-0.24907176820596D-10	0.10534878629266D-10
8	6	-0.18393642697634D-11	0.86277431674150D-11
7	7	0.25590780149873D-13	0.44759834144751D-12
8	7	0.34297618184624D-12	0.38147656686685D-12
8	8	-0.15803322891725D-12	0.15353381397148D-12